3D chemical imaging of brain tumors

Abiodun Ogunleke

université de BORDEAUX

THÈSE

PRÉSENTÉE À

L'UNIVERSITÉ DE BORDEAUX

ÉCOLE DOCTORALE DES SCIENCES CHIMIQUE

Par **ABIODUN OGUNLEKE**

POUR OBTENIR LE GRADE DE

DOCTEUR

SPÉCIALITÉ: CHIMIE PHYSIQUE

IMAGERIE CHIMIQUE 3D DE TUMEURS DU CERVEAU

Soutenue le: 18 Mars 2019

Devant la commission d'examen formée de:

Professeur Sophie Javerzat	Examinateur
Professeur Ganesh Sockalingum	Rapporteur
Professeur Wojciech M. Kwiatek	Rapporteur
Professeur Cyril Petibois	Directeur de thése

université de BORDEAUX

PhD THESIS

PRESENTED AT THE

UNIVERSITY OF BORDEAUX

DEPARTMENT OF CHEMISTRY

by **ABIODUN OGUNLEKE**

TO OBTAIN THE DEGREE OF

Doctor of Philosophy

SPECIALITY: CHEMICAL PHYSICS

3D CHEMICAL IMAGING OF BRAIN TUMORS

Defended on: March 18, 2019

Defended in front of the exam committee:

Professor Sophie Javerzat	Examiner
Professor Ganesh Sockalingum	Reviewer
Professor Wojciech M. Kwiatek	Reviewer
Professor Cyril Petibois	Director of thesis

Acknowledgements

This work has been carried out under the supervision of **Prof. Cyril Petibois** in the group of biophysics of vascular plasticity, Institut national de la santé et de la recherche médicale unité 1029 de l'angiogenèse et du micro-environnement tumoral (INSERM U1029, LAMC), University of Bordeaux, France. It would have been impossible to complete this work without the support and kind gestures of many people

Firstly, I would like to thank God, the giver of life and wisdom for the gift of life and wisdom.

I would love to thank profoundly **Prof. Cyril Petibois**, for giving me this valuable opportunity to learn under his direction. I am deeply grateful for his generosity, kindness, tenderness, constructive criticism, considerations and continuous involvement in the project. Without his immense encouragement, inspiring guidance, and support this work would not have been completed. It was an honour and privilege working under his supervision.

I would also love to express my gratitude to every member of the team who showed me love and guidance throughout the period of this work. I am grateful for the contributions of **Maylis Delugin, Prof. Sophie Javerzat, Dr. Benoit Recur** and **Dr. Hugo Balacey**. I will forever be grateful for your encouragement, kind words, constructive criticism and support throughout the period of this work. It was such an honour working with and learning from you all.

I would also love to express my appreciation to every member of the Harvesting Faith Ministries church who became my family away for home. I am deeply grateful for your support and prayers.

Last but in no way the least, I want to thank my family, for their encouragement, prayers and support from birth till this moment.

DEDICATED TO MY PARENTS AND FAMILY

Résumé

L'histologie tridimensionnelle (3D) est un nouvel outil avancé de cancérologie. L'ensemble du profil chimique et des caractéristiques physiologiques d'un tissu est essentiel pour comprendre la logique du développement d'une pathologie. Cependant, il n'existe aucune technique analytique, in vivo ou histologique, capable de découvrir de telles caractéristiques anormales et de fournir une distribution 3D à une résolution microscopique. Nous présentons ici une méthode unique de microscopie infrarouge (IR) à haut débit combinant une correction d'image automatisée et une analyse ultérieure des données spectrales pour la reconstruction d'image 3D-IR. Nous avons effectué l'analyse spectrale d'un organe complet pour un petit modèle animal, un cerveau de souris avec une tumeur de gliome implantée. L'image 3D-IR est reconstruite à partir de 370 coupes de tissus consécutives et corrigée à l'aide du tomogramme à rayons X de l'organe pour une analyse quantitative précise du contenu chimique. Une matrice 3D de spectres IR 89 x 10^6 est générée, ce qui nous permet de séparer la masse tumorale des tissus cérébraux sains en fonction de divers paramètres anatomiques, chimiques et métaboliques. Nous démontrons pour la première fois que des paramètres métaboliques quantitatifs (glucose, glycogène et lactate) peuvent être extraits et reconstruits en 3D à partir des spectres IR pour la caractérisation du métabolisme cérébral / tumoral (évaluation de l'effet de Warburg dans les tumeurs). Notre méthode peut être davantage exploitée en recherchant l'ensemble du profil spectral, en distinguant différents points de repère anatomiques dans le cerveau. Nous le démontrons par la reconstruction du corps calleux et de la région des noyaux gris centraux du cerveau.

Mot-clés: Imagerie IRTF, imagerie IR-QCL, imagerie chimique 3D, pathologie numérique, test Clinique

Abstract

Three-dimensional (3D) histology is a new advanced tool for cancerology. The whole chemical profile and physiological characteristics of a tissue is essential to understand the rationale of pathology development. However, there is no analytical technique, in vivo or histological, that is able to discover such abnormal features and provide a 3D distribution at microscopic resolution. Here, we introduce a unique high- throughput infrared (IR) microscopy method that combines automated image correction and subsequent spectral data analysis for 3D-IR image reconstruction. I performed spectral analysis of a complete organ for a small animal model, a mouse brain with an implanted glioma tumor. The 3D-IR image is reconstructed from 370 consecutive tissue sections and corrected using the X-ray tomogram of the organ for an accurate quantitative analysis of the chemical content. A 3D matrix of 89 x 10^6 IR spectra is generated, allowing us to separate the tumor mass from healthy brain tissues based on various anatomical, chemical, and metabolic parameters. I demonstrate for the first time that quantitative metabolic parameters (glucose, glycogen and lactate) can be extracted and reconstructed in 3D from the IR spectra for the characterization of the brain vs. tumor metabolism (assessing the Warburg effect in tumors). Our method can be further exploited by searching for the whole spectral profile, discriminating different anatomical landmarks in the brain. I demonstrate this by the reconstruction of the corpus callosum and basal ganglia region of the brain.

Keywords: FTIR microscopy, QCL-IR imaging, 3D chemical imaging, Digital pathology, Clinical test

Glossary

2D – Two-dimensional

3D – Three-dimenisional

BBB – Blood brain barrier

CT – Computed tomography

DA – Discriminant analysis

FOV – Field of view

FPA – Focal plane array

FTIR – Fourier transform infrared

GFAP – Glial fibrillary acidic protein

H&E – Hematoxylin and eosin

IHC – Immunohistochemical

IR – Infrared

LDA – Linear discriminant analysis

LPPC – Log-polar phase correlation

MCT - Mercury-Cadmium-Telluride

MRI – Magnetic resonance imaging

MSI – Mass spectrometry imaging

PCA – Principal component analysis

QCL – Quantum cascade laser

m/z – Mass to charge ratio

SIFT – Scale invariant feature transform

SNR – Signal to noise ratio

SURF – Speeded up robust features

XRF – X-ray fluorescence

WHO – World Health Organisation

List of Figures

List of Tables.

Table of Contents

INTRODUCTION

This work was conducted within the 'biophysics' of vascular plasticity group in the research unit of the angiogenesis and the micro-environment of tumors, INSERM U1029 situated at the University of Bordeaux. The main theme of this research is to develop a 3D imaging methodology for chemical characterization of brain tumors. This is an area of cancer research that is currently not yet developed and has a potential of becoming very valuable in improving the existing diagnostic tool for brain tumors.

Brain tumors due to their ability to exist even at a small size, thus making them extremely to diagnose and cure, are often considered as one of the highly destructive and lethal group of brain diseases. Surgery is usually difficult due to the delicate nature and function of the organ. Characterized with high morbidity and mortality, brain tumors often lead to progressive decline in physical, cognitive and emotional functions and are in many instances fatal.

Brain tumors result from an uncontrolled proliferation of cells derived from neural tissue or structural, supportive tissue within the brain [1]. It is simply the formation of abnormal cells within the brain. Typically, the human brain completes its growth and development soon after birth and the vast majority of cells enter a resting state; they normally never divide again. However, one exception to this rule is when a brain tumor develops. The abnormal brain cells re-enter the "cell-cycle" because of alterations in any of a huge number of genes that control cell division and growth processes [2].

Depending on their behavior, tumors are generally classified into benign and malignant or cancerous tumors. Benign tumors are group of similar cells characterized with slow growth and do not invade surrounding tissues or spread to other organs. On the other hand, malignant or cancerous tumors are heterogeneous cells characterized with rapid growth and invasion into surrounding tissues and organs. Brain tumors can be further classified based on their origin and location in the brain. Brain tumors can be classified into primary and secondary tumors depending on their origin.

Primary brain tumors originate from the brain, cranial nerves, pituitary gland or meninges. The largest and most aggressive group of primary brain tumors based on the location of their origin is the glioma. Gliomas make up 80% of all malignant primary brain tumors [3] and mainly affect the astrocytes (also oligodendrocyte).

The secondary brain tumors (metastases) originates from organs outside the brain or from primary tumors in the brain. Secondary brain tumors are always malignant and make up the majority of cancerous brain tumors. Typically, secondary brain tumors arise from primary tumor cells that migrate hematogenously or via direct invasion of adjacent tissue They usually start in one part of the body such as the lungs or breast and spread, or metastasize, to the brain through the blood brain barrier (BBB) [4].

Several therapeutic strategies have been proposed and are clinically available for brain tumor treatment. Resection is a common practice in brain tumor treatment. It aims at reducing the intracranial pressure by removing as much tumor as is safely possible to preserve neurological function [5]. Other strategies includes chemotherapy [6] [7], radiation therapy [8] [9], active surveillance [10] [11], supportive therapy [5].

However, the treatment of brain tumors remains a challenge as the mortality rate remains high in spite of the advances in the therapeutics of brain tumors. A study conducted in 2012 [12] shows that worldwide, approximately 256,213 new cases of brain and other CNS tumors were diagnosed, with an estimated 189,382 deaths. This represents approximately 74% mortality from the incidences reported.

Therapeutics of brain tumors is highly dependent on the accurate characterization and consequently diagnosis of brain tumors. The choice of therapeutic strategy applied depends on the reliability of diagnosis which dictates the prognosis and consequently the therapy. Therapeutic strategy such as resection depends on accurate delineation of the tumor mass. Hence, accurate brain tumor diagnosis is a vital step in the treatment of brain tumors.

Generally, brain tumor imaging is the first step in brain tumor diagnosis. Brain tumor imaging encapsulates a variety of methods and technologies used to either directly or indirectly obtain the image of the anatomy and physiology of the brain. Brain tumor imaging plays an important role in the diagnosis, treatment planning, and post-therapy assessment of brain tumors. It provides a visual representation of the brain which helps doctors to preoperatively visualize the morphology, location, size, grade and consequently the prognosis and treatment of brain tumors.

Magnetic resonance imaging (MRI) method is clinically the gold standard for brain tumor imaging. MRI is based on the principle of nuclear magnetic resonance and uses radiofrequency waves to probe

soft tissue anatomy and physiology *in vivo*. It is a non-invasive technique, which provides good soft tissue contrast and is widely available in clinics. MRI makes it possible to produce markedly different types of tissue contrast by varying excitation and repetition times, which makes it a very versatile tool for imaging different structures of interest [13].

MRI was first reported as a viable tool for detecting brain tumor in 1984 [14] and has evolved to become the standard clinical routine in brain tumor examination. It provides neuro-oncologists with 2D or 3D contrast images used to identify lesion, determine the lesion location, extent of tissue involvement, and resultant mass effect upon the brain, ventricular system, and vasculature [15].

However, it is unable to reveal pathological objects, such as metastases or tumors with diameter less than 5–10 mm. This is due to the spatial resolution which cannot go below 1-mm at the best for human applications, 100-μm in small animals [16] [17] [18] and low sensitivity to some tumor types [19]. In spite of the advances in MRI [15] [20], however, due to the limited spatial resolution which makes it impossible to characterize brain tumors at cellular resolution. MRI is mainly used clinically for preoperative analysis and to aid targeting of tumors for tumor excision [21].

Histopathological examination is the standard for brain tumor diagnosis [22]. Histopathological analysis is the standard procedure routinely used to reveal the amount of necrosis, proliferative regions, collagen and vascularity within the tumor area [23]. Histopathological techniques enable the analysis of the cellularity, nuclear atypia, metabolic pathways, mitotic activity, pleomorphism, vascular hyperplasia, and necrosis [21].

Historically, histopathological evaluation had been used by the World Health Organization (WHO) for the classification of brain tumors in the light of tumorigenesis; based on their microscopic similarities with different putative cells of origin and their presumed levels of differentiation. Recent updates in the WHO classification has incorporated both histological and molecular genetic features [22] in tumor classification. Analyses of the metabolic pathways involved in tumorigenesis may also provide useful information for brain tumor diagnosis and treatment.

Hypoxia and metabolite deprivation are commonly observed in solid tumors and modulate the transcription of genes involved in several cellular processes, including malignant growth, angiogenesis, and metastasis [24]. Brain tumors also exhibit difference in their energy requirement, depending on the cell types considered, tumor grade and lesion locations. Thus, an accurate

determination of the spatial metabolic profile of tumors is required for a better diagnosis in order to adopt relevant therapeutic strategy.

Traditionally, histopathological examination prepares sample tissues for microscopic study by histological staining. This is done in order to reveal cellular composition of tissues. Typically, a molecular target is determined and probed under a microscope with the aid of histological stains. Staining is a commonly used medical process in the diagnosis of tumors in which a dye color is applied on the posterior and anterior border of the sample tissues to locate the diseased or tumorous cells or other pathological cells [25]. More recently, immunostaining which binds antibodies to antigens in tissues have been used to stain particular protein, lipid and carbohydrate.

Unfortunately, traditional histopathology imaging techniques are limited in brain tumor applications due to the limited known molecular information about brain tumors. Furthermore, multiple immunostaining cannot identify more than four different antigens on a same sample [26]. Alternatively, metabolic parameter can be used as complementary information for tumor diagnosis through techniques that allow access to the 3D organization of tissue contents along with their quantitative measurement, notably for chemical and cellular parameters can be utilized in histological examination.

Spectroscopic technique such as mass spectroscopy can offer quantitative measurement of tissue contents. Combining a spectrometer and a microscope is called spectro-microscopy. These setups offer a global view of the sample chemical contents, which can be further analyzed for extracting relevant molecular parameters for diagnosis [27]. 3D chemical imaging is achieved by several spectro-microscopic methods. These provide a quantitative analysis of tissue content and substructures with a depth of information that no other histological technique can determine from the same sample. However, they are currently underexploited despite their potential.

An emerging spectro-microscopic technique for histopathological examination is IR spectro-microscopy. As a result of the advent of powerful IR sources with quantum-cascade lasers (QCLs) in 2014, IR spectro-microscopy can now produce millions of IR spectra per hour with high S/N. This innovation has led to new developments in IR image analyses for biosamples, such as 3D-IR image reconstructions for the quantitative analysis of metabolic or biochemical parameters [27].

3D spectroscopy analysis rapidly faces the problem of big data management as spectra are characterized by large series of x, y data whose exploitation requires intense calculation means. Therefore, most of spectro-microscopy techniques are currently not appropriate on large samples, i.e. typically from the 1 mm^3 to the 1 cm^3 tissue volumes, such as a tumor biopsy or a small animal organ in which a pathology can be modeled.

The term 'big data' in 3D chemical imaging holds a double meaning, since a 3D spectrum matrix is at the same time massive and contains complex chemical information. The massive nature of the information is due to the huge number of spectra. However, the complex nature of this information stems from the fourth dimension of the voxels, the spectral data, which require advanced data treatments to extract the 'embedded' chemical information (e.g., individual absorption bands in IR and Raman spectra by curve-fitting methods).

Furthermore, analytics (i.e., the algorithms performing spectral data treatments to produce biological metadata) require major computing resources, combining CPU means for high-performance calculation with GPU cards for both parallelized calculations on spectra and visualization of 3D reconstructed results [28].

3D reconstruction is emerging in IR spectro-microscopy. Previously, acquisition of a 3D histological dataset was not feasible due to bottlenecks such as inability to maintain consistent S/N and relatively slow acquisition time for large samples. As the new frontier of 3D chemical imaging by IR is just opening up, there is currently no standard processing sequence or specialized algorithms for 3D reconstruction of IR slices. Thus, there is need to develop a standard processing sequence for 3D reconstruction of IR slices.

In this thesis, advanced spectra data treatment methods were developed for the characterization of brain tumors. Also developed is an advanced processing sequence for 3D quantitative reconstruction of IR slices. An application of our developed methods is shown in a quantitative 3D reconstruction of tumor in a mouse brain based on the chemical characterization of tumor and normal tissue metabolism. Also presented in this thesis is the 3D reconstruction of the anatomy of mouse brain by using our advanced processing sequence for 3D quantitative reconstruction of IR slices.

This manuscript is organized as follows:

The first part of this manuscript Part A, is dedicated to the understanding the state of the art within the domain of this work. In the first chapter, we introduce the concept of chemical characterization of brain tumor by infrared imaging. I define the biological and anatomical elements needed to understand our work as well as review on the biomarkers for chemical characterization of brain tumors.

In the second chapter, we introduce the different techniques for 3D reconstruction of histological images. I present a comparative study of these methods and their application to 3D reconstruction of infrared images.

In the second part of this manuscript Part B, we present the contributions made during the course of this work. In the third chapter, we introduce an advanced processing sequencing for the development of 3D IR imaging. This includes computational methods for extracting biological metadata from IR spectra and a hierarchical method for 3D reconstruction of IR metadata images.

In the fourth chapter, we present the application of our proposed methods to 3D chemical imaging of tumors in a sample mouse brain. I discuss our experimental setup, sample preparation and data acquisition and a step by step detailed experiment of our proposed methods for chemical characterization of brain tumor.

In the fifth chapter, we present an elaborate experiment to resolve the anatomy of the mouse brain vis-à-vis it's chemical information in what is called 3D anatomo-chemistry of the mouse brain. I present the reconstruction of some anatomical landmark in the mouse brain in this chapter.
In the last chapter, we make a general conclusion and a reflection on the perspectives that have been refined by this work.

CHAPTER 1: Brain tumor characterization and diagnosis

1.1. General Description of brain tumors

Brain tumors result from an uncontrolled proliferation of cells derived from neural tissue or structural, supportive tissue within the brain [1]. It is typically the formation of abnormal cells within the brain. The human brain completes its growth and development soon after birth and the vast majority of cells enter a resting state; they normally never divide again. However, a major exception to this rule is when a brain tumor develops.

The abnormal brain cells re-enter the "cell-cycle" because of alterations in one or several genes that control cell division and growth processes [2]. Depending on their behavior, tumors are generally classified into benign and malignant or cancerous tumors. Benign tumors are group of similar cells characterized with slow growth and do not invade surrounding tissues or spread to other organs.

On the other hand, malignant or cancerous tumors are heterogeneous cell phenotypes characterized with rapid growth and invasion into surrounding tissues and possibly metastasing to distant organs. Brain tumors can be further classified based on their origin and location in the brain.

Brain tumors can be classified into primary and secondary tumors depending on their origin.

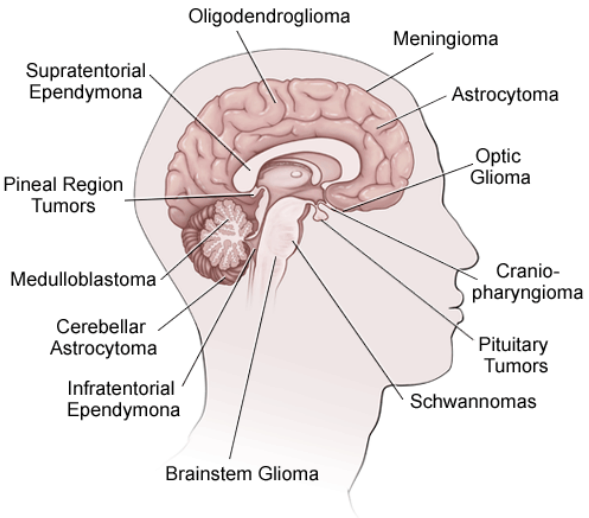

Figure 1Brain tumor classification based on tumor location [29]

Primary brain tumors originate from the brain, cranial nerves, pituitary gland or meninges. The largest and most aggressive group of primary brain tumors based on the location of their origin is the glioma. Gliomas make up 80% of all malignant primary brain tumors [3].

The secondary brain tumors (metastases) originates from organs outside the brain or from primary brain tumors. Secondary brain tumors are always malignant and make up the majority of cancerous brain tumors. Typically, secondary brain tumors arise from primary tumor cells that migrate via the blood system or through direct invasion of adjacent tissue They usually start in one part of the body such as the lungs or breast and spread, or metastasize, to the brain through the blood brain barrier (BBB) [4].

In most cases, a brain tumor is named for the cell type of origin. Some brain tumors are named according to their location. Today, most medical institutions use the World Health Organization (WHO) classification system to identify brain tumors [22].

The WHO classifies brain tumors by cell origin and how the cells behave, from the least aggressive (benign) to the most aggressive (malignant). Some tumor types are assigned a grade, which signifies the rate of growth. There are variations in grading systems, depending on the tumor type.

The classification and grading of an individual tumor characterizes the features of the tumor at a specific stage of growth. Although they may fall into a specific classification or category, brain tumors are specific to each individual. Brain tumors have vastly different characteristics and patterns of growth due to the molecular profile of the individual tumor.

A series of criteria are used to make a diagnosis and grading. One important criterion is anaplasia, the manner in which tumor cells grow with the loss of normal form or structure. The degree of anaplasia helps to forecast a tumor's growth potential. The most rapidly growing tumors have the highest degree of anaplasia. In addition to other criteria, some tumors are examined for their genetic traits to evaluate the nature of the tumor.

Gliomas are the most common aggressive and the worst kind of primary brain tumors, which represent about 42% of all adult brain tumors [30] and approximately 50% in children. Gliomas are usually located in the deep white matter of the cerebral hemispheres [31], most frequently in the frontal lobe and mainly affect the astrocytes (also oligodendrocyte).

Depending on their shape and size, gliomas are classified from grade I (considered as benign) to grade IV (the most malignant). The grade I glioma are poorly aggressive tumors most common in children and youngsters. Grade II are diffuse or low-grade astrocytomas, grade III are high-grade anaplastic astrocytomas and grade IV are also called glioblastoma multiform (GBM) or malignant astrocytomas.

Several therapeutic strategies have been proposed and are clinically available for glioma treatment. Resection is a common practice in brain tumor treatment. It aims at reducing the intracranial pressure by removing as much tumor as is safely possible to preserve neurological function [5].

Other strategies includes chemotherapy [6] [7], radiation therapy [8] [9], active surveillance [10] [11], supportive therapy [5]. These strategies can also be combined in some cases to reduce the probability of a relapse.

However, the treatment of glioma remains a challenge as the mortality rate remains high in spite of the advances in the therapeutics of brain tumors. A study conducted in 2012 [12] shows that worldwide, approximately 256,213 new cases of glioma and other CNS tumors were diagnosed, with an estimated 189,382 deaths. This represents approximately 74% mortality from the incidences reported.

Therapeutics of brain tumors is highly dependent on the accurate characterization and consequently diagnosis of brain tumors. The choice of therapeutic strategy applied depends on the reliability of diagnosis which dictates the prognosis and consequently the therapy.

Therapeutic strategy such as resection depends on accurate delineation of the tumor mass. Hence, accurate brain tumor diagnosis is a vital step in the treatment of brain tumors.

1.2. Current Diagnostic Methods

Clinical symptoms are usually indicators of the presence of glioma tumors in the brain. The observed symptoms depend on the anatomical site of the tumor. Brain glioma can cause headaches, nausea, seizures, vomiting and epilepsy, diminished consciousness, weakness or numbness, loss of vision, personality changes and loss of mental sharpness or difficulty in concentrating. Glioma of the optic nerve may cause visual loss.
However, the standard procedure for diagnosing glioma is through brain imaging and histopathological examination of brain tissues.

1.2.1. Brain Imaging

Generally, brain tumor imaging is the first step in brain tumor diagnosis. Brain tumor imaging encapsulates a variety of methods and technologies used to either directly or indirectly obtain the image of the anatomy and physiology of the brain.

Brain tumor imaging plays an important role in the diagnosis, treatment planning, and post-therapy assessment of brain tumors. It provides a visual representation of the brain which helps doctors to preoperatively visualize the morphology, location, size, grade and consequently the prognosis and treatment of brain tumors.

1.2.1.1. Computed Tomography

Computed Tomography (CT) Computed Tomography combines sophisticated x-ray scanner and computer technology. Unlike other medical imaging techniques, CT has the ability to show a combination of soft tissue, bone, and blood vessels in the final 2D or 3D images.

CT is effective at examining bone and tissue calcification and haemorrhage. It can determine some types of tumours, as well as help detect swelling and bleeding. Usually, iodine is the contrast agent used during a CT scan.

However, CT scans involve exposure to ionizing radiation. This is a concern for people who have multiple CT scans and for children, because they are more sensitive to radiation than adults.

While high resolution CT allows the clear imaging of blood vessel of about 30–50 μm diameter, however, the x-ray dose used for acquisition increases as the quality and resolution of the final

image increases. Thus a compromise must be sought between the overall image quality and the size of tumours. This makes CT not suitable for imaging glioma metastases.

1.2.1.2. Positron-emission Tomography

Positron-emission tomography (PET) imaging uses positron-emitting radionuclides to label molecules such as glucose, water or ammonia which can be imaged inside the body. Although it has limited spatial resolution (3–4 mm), it can be preferred due to its higher specificity and sensitivity for in vivo imaging. It requires also probes such as fluoro-deoxy glucose (FDG) labeled with the positron emitted F having a half-life of 110 min.

Due to the technique resolution and temporal limits, such label can be used only to locate the primary tumor site. PET is highly specific due to labeling molecules, but it limited when possible applications to small tumor specimens where long accumulation of contrast agent is required to obtain a signal.

1.2.1.3. Magnetic Resonance Imaging

Magnetic Resonance Imaging (MRI) An MRI is the standard imaging technique for suspected brain tumors. An MRI is a scanning device that uses magnetic fields and computers to capture images of the brain. It does not use x-rays and it provides pictures from various planes, which permits doctors to create a three dimensional image of the tumor. The MRI detects signals emitted from normal and abnormal tissue, providing clear images of most tumors.

Magnetic resonance imaging (MRI) method is clinically the gold standard for brain tumor imaging. However, it is unable to reveal pathological objects, such as metastases or tumors with diameter less than 5–10 mm. This is due to the spatial resolution which cannot go below 1-mm at the best for human applications, 100-μm in small animals [16] [17] [18] and low sensitivity to some tumor types [19].

In spite of the advances in MRI [15] [20], however, due to the limited spatial resolution which makes it impossible to characterize brain tumors at cellular resolution. MRI is typically used clinically for preoperative analysis and to aid targeting of tumors in biopsies [21].
The above mentioned imaging techniques are only effective for the localization of the bulk disease in vivo but does not allow the imaging of detailed anatomy and physiology of tumors as well as

metastases imaging. This is due to their limited spatial resolution which cannot go below 1-mm at their best for human and 100-μm in small animal applications.

Consequently, it is necessary to use alternative ex-vivo histopathological examination of tissues for diagnosis of tumors. Histopathological examination is the standard for brain tumor diagnosis [22]. Histopathological procedures are routinely used to reveal the amount of necrosis, proliferative regions, collagen and vascularity within the tumor area [23].

Thus, biopsies are performed to enable the analysis of the cellularity, nuclear atypia, metabolic pathways, mitotic activity, pleomorphism, vascular hyperplasia, and necrosis [21] of tumors in order to obtain pathological diagnosis and are also helpful to identify the tumor margins.

1.2.2. Biopsy & surgical excision

A biopsy is a surgical procedure in which a small sample of tissue is taken from the tumor site and examined under a microscope. The results help the doctor diagnose the type of tumor. The biopsy will provide information on types of abnormal cells present in the tumor. There are two kinds of biopsy procedures: an open and a closed biopsy.

An open biopsy is done during a craniotomy. A craniotomy is a surgical procedure that involves removing a piece of the skull in order to get access to the brain (excision). A closed biopsy (also called stereotactic or needle biopsy) is performed when the surgeon wants to avoid removing healthy tissue from the area surrounding the tumor, or when the tumor is in an area of the brain that is difficult to reach.

Guided by a CT or MRI that is performed prior to the procedure, the surgeon drills a small hole into the skull and passes a narrow, hollow needle through the hole into the tumor to remove a sample of tissue. Once a sample is obtained, a pathologist will examine the tissue under a microscope. Further examination or analysis may be performed on the tumor tissue in order to accurately diagnose the tumor.

The pathologist diagnoses tumors by examining the histology and physiology of the tissue. This domain is referred to as histopathology. It involves the identification of tumors by light microscopy of pathognomonic histological and immunohistochemical (IHC) staining patterns. Hematoxylin and

eosin (H&E) is the standard stain used by histologists to highlight certain areas or molecules in tissues. Histological examination includes gradation of tumor cell density, vascularization, small-cell, density and matrix loosening, and the presence of necrosis, atypia, mitoses, and endothelial proliferation.

The pathologist typically uses some salient characteristics called biomarkers which characterize different types of tumors in order to determine the type and grade of the tumor. The biomarkers typically include; the morphology, molecular and chemical composition of the tumor tissue. For example, the degree of anaplasia, mitotic activity as well as endothelial proliferation and/or necrosis can be used to identify GBM.

1.2.2.1. Histological/Anatomo-pathological characterization

Anatomo-pathology is one of the standard histopathological and clinical diagnostic criteria. The first published classification of brain tumors by the WHO was based purely on their morphological and histological features. Some brain tumors are well-differentiated and can be diagnosed solely based on their histopathological appearance [32].
Histologically, brain tumors were categorized as astrocytoma, oligodendroglioma, glioblastoma and oligoastrocytoma [33] [34] [35].

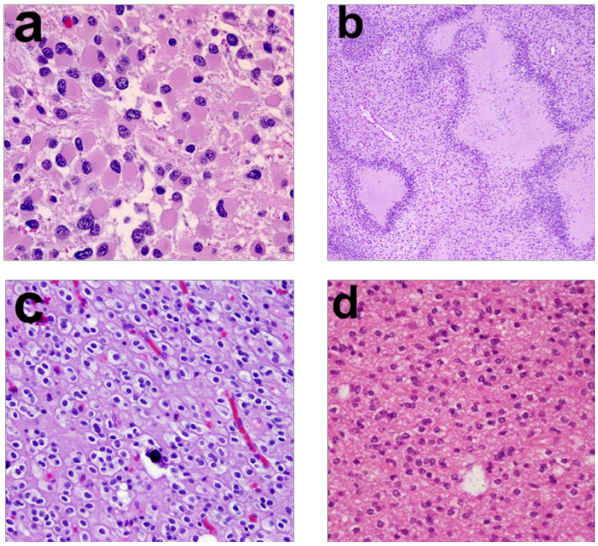

Figure 2 Histological classification of brain tumors. A: Astrocytoma showing variable nuclear pleomorphism. B: Gliobastoma showing viable cells palisading necrotic areas. C: Oligodendroglioma showing unstained cytoplasm and a fine capilliary network. D: Oligoastrocytoma showing heterogeneous diffusive tumors [36]

Astrocytomas are typically invasive and do not form a solid mass or clear margins. Well-differentiated tumor cells exhibit a moderate increase in the number of nuclei, variable nuclear pleomorphism, and a mesh-like network of glial fibrillary acidic protein (GFAP) processes. Necrosis and a florid microvascular proliferation usually indicate the presence of glioblastoma.

Generally, oligodendrogliomas are diffusive tumors which are primarily made up of sheets of cells with spheroid nuclei surrounded by a clear halo (unstained cytoplasm) and a fine capillary network. The grading is determined by the increase in mitotic activities, nuclear anaplasia and cell density.

For diffusive tumors, it is quite difficult to identify and associate to a specific family of tumors. Hence, the oligoastrocytoma category was created. However, poorly-differentiated tumor cells have been reported to have high rates of inter-observer variability which leads to misdiagnosis and inappropriate therapeutic treatment.

This is justifying further molecular analysis of tumor cells, i.e., genes sequencing, in order to identify key prognostic markers and classify a tumor based on unique molecular and cytogenetic parameters. This is making a direct link between pathological evaluation of tumor biopsy and refining the diagnostic markers based on genomics.

Furthermore, multiple immunostaining cannot identify more than four different antigens on the same sample. These bottlenecks give rise to the need for the development of novel or complimentary rapid and accessible techniques for brain tumor diagnosis.

Also, the use of labels makes the standard techniques semi-quantitative at best due to different manual interventions during the imaging of tissues. This lack of quantitative information compromises automation and advanced data analytics that could potentially overcome the limitations of pathologist.

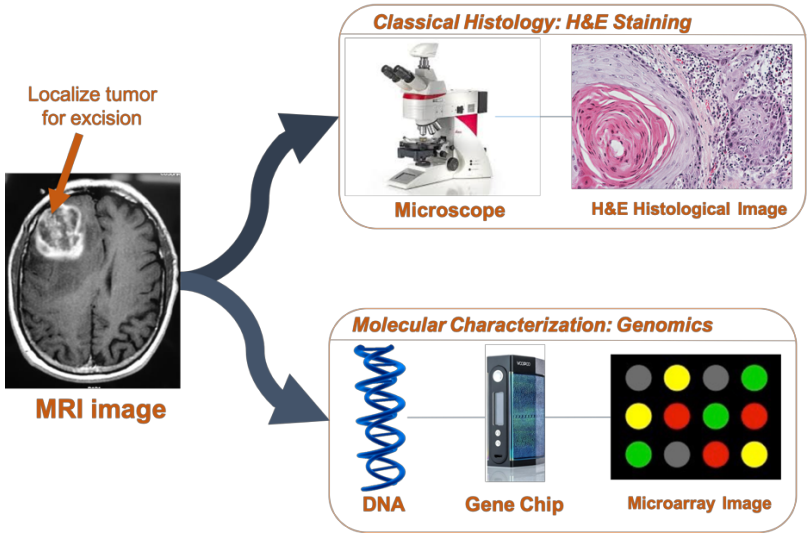

Figure 3 Overview of WHO standard tumor diagnostic tools. The use of MRI imaging as the gold standard for determining tumor site, followed by biopsy, histological imaging and molecular characterization.

1.2.2.2. Molecular characterization

The recent WHO classification is the first to incorporate molecular parameters to further define gliomas in an objective manner [32]. Several molecular genetics studies have been conducted identifying consistent gene loci anomalies associated with particular types of cancer. Not only are these genetic markers used to classify tumor subtypes, but they also are often prognostic predictors of the course of the disease.

For example, in gliomas, the most common mutations identified to date are in the IDH1/IDH2 genes with IDH1 mutations identified in approximately 80% of grade 2/3 gliomas [22]. The most common mutation is a single amino acid missense mutation in IDH1 at arginine 132 (R132H), identified in 12% of samples [23]. Glioma survival is strongly associated with the IDH1/IDH2 mutation, with IDH1 wild-type typically being associated with poorer outcomes [24,25].

Another molecular marker identified is co-deletion of the 1p and 19q arms of their respective chromosomes [24]. Use of IDH1 mutation and 1p/19q co-deletion status has nearly eliminated the previous amorphous classification of oligoastrocytoma [26].

Recent advances in sequencing along with the vast data from cancer genome atlas have enabled the classification of GBM into four distinct subtypes including classical, mesenchymal, proneural and neural [37]. This efficient classification has been reported to have resulted in the increase of the survival period for patients.

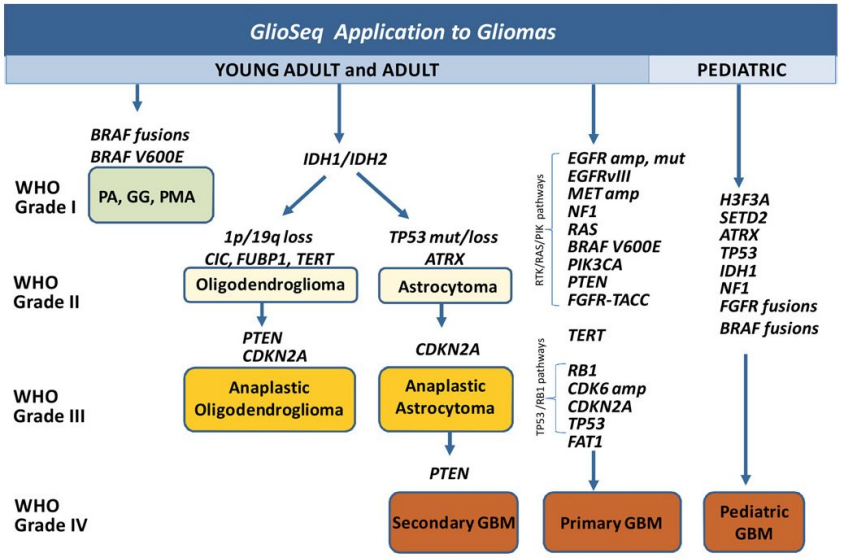

Figure 4 WHO molecular classification of brain cancer in adult, young adult and children. Showing the different grades of brain cancer; Grade I-IV, classified by the IDH1/IDH2 mutation [38].

However, a major bottleneck with molecular characterization is the running cost and the time required for complete screening of tissues. Also, the recognition of histologic heterogeneity within brain tumors containing multiple phenotypes are compelling reasons for developing more refined and accurate diagnostic techniques, which may help improve treatment outcomes [39].

These conventional techniques used for diagnosis, are also prone to biased subjective interpretation by the histopathologists. This is because these processes are largely manual and depend on the pathologist's expertise for the interpretation of results. Conventional histology is also not suited for metabolic probe of tumors which is essential in tumor development.

1.2.2.3. Chemical characterization

Alternatively, the chemical analysis of tissues can be also performed by label-free microscopies, such as those derived from spectroscopy. Combining a spectrometer and a microscope is called spectro-microscopy. These setups offer a global view of the sample chemical contents (lipids, proteins, carbohydrates and nucleic acids) which can be analyzed for extracting relevant molecular parameters for diagnosis.

As a general features for spectro-microscopies, they allow qualitative and quantitative analysis of the basic components of tissues with a depth of information that no other histological technique can determine from the same sample. This is done without the use of histochemical stains before data acquisitions, thus ensuring to analyze the tissue with all its constituent unaltered.

Spectroscopies are quantitative by nature. They allow mapping potentially a wide range of chemical information in a non-supervised pattern, which is undoubtedly a major advantage for comparison between healthy and pathological tissue specimens without any a priori knowledge about the sample.

1.3. Spectroscopies and brain tumor analysis

Spectroscopies offer an invaluable opportunity to access chemical features of biological samples in a non-supervised way. The global chemical information they provide enables the exploitation of a large array of chemical species or parameters. Spectroscopic techniques such as Mass spectrometry, Raman, Mid-Infrared and X-ray fluorescence are the only currently available techniques that can quantitatively analyze tissue content (e.g., molecular concentrations) and substructures (e.g., cells or blood vessels).

Figure 5 shows the physical principle of the mid-infrared, raman and mass spectroscopy methods. X-ray fluorescence (XRF) can be used to analyse trace elements and metal ions in biosamples, however, it is not discussed in this thesis due to its low relevance to cancer imaging.

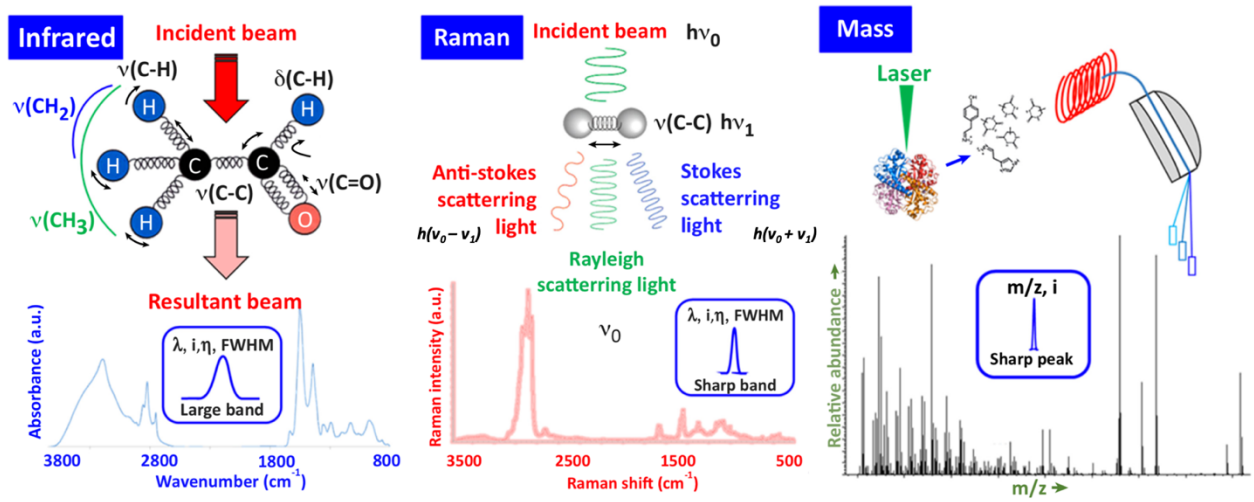

Figure 5 Physical Principles of Spectromicroscopy Methods Providing Global Chemical Information from Tissues. The infrared (IR) and Raman bands can be described by their position (l), intensity (i), full width at half height (FWHH), and Gaussian/Lorentzian fraction (η). The mass peaks are described by their intensity (i) at given mass:charge ratio (m/z). Therefore, mass spectra (MS) only require the identification or localization of the peaks and calibration of their intensity scale to extract quantitative information while IR and Raman require more sophisticated spectral data treatments will be more sophisticated. This is due to the large overlap between adjacent bands for complex biological sample spectra in IR and Raman, meaning that using the intensity at a given l is rarely characteristic of a single band. This phenomenon is even more pronounced for IR spectroscopy, which provides large absorption bands [28].

1.3.1. Mass Spectrometry Imaging

Mass spectrometry is based on ionization of the samples and separation of ions according to their mass to charge ratio (m/z). Mass Spectrometry Imaging (MSI) techniques have two possible applications: the analysis of either inorganic or organic content through mass fractions. In general, MSI techniques include a spatially resolved ionization method to collect mass spectra from an array of positions across a sample [28].

Mass spectrometry has evolved over the years and has recently gained attention from the medical community as potential routine tool for medical diagnosis due to the new developments in ambient ionization techniques [40].

The ambient ionization techniques offer a simple instrumentation and real-time assessment of tissue molecular information which has been a major bottleneck with MSI. A chemical mass spectrum displaying hundreds of compounds can be obtained from a selected region of a tissue sample placed under the ionization source in less than 1 second, depending on the choice of mass analyzer.

A major strength of MSI is its high sensitivity and specificity, several molecular details can be obtained from MSI mass spectra. A trademark of MSI is its sensitivity to small molecules such as lipids and metabolites. Due to its sensitivity, MSI has been used to study the metabolomics, lipidomics and proteomics of glioblastoma(Figure 6) [41, 42].

While the high sensitivity of MSI is of great diagnostic value, the current state of MSI technology poses some limitations to the clinical use of MSI for brain tumor diagnosis. Although major improvements have been reported, MSI general remains relatively slow for tissue imaging [43].

MSI is also limited by the spatial resolution offered by the current instruments. While some MSI techniques allow imaging at sub-micrometer resolution, a compromise of acquisition time and sensitivity is usually required for such image acquisitions [43]. Depending on the m/z range set a priori in order to define the molecular parameters which are of interest for a tissue, MSI remains a supervised method and its spectral data are challenging to analyze [28].

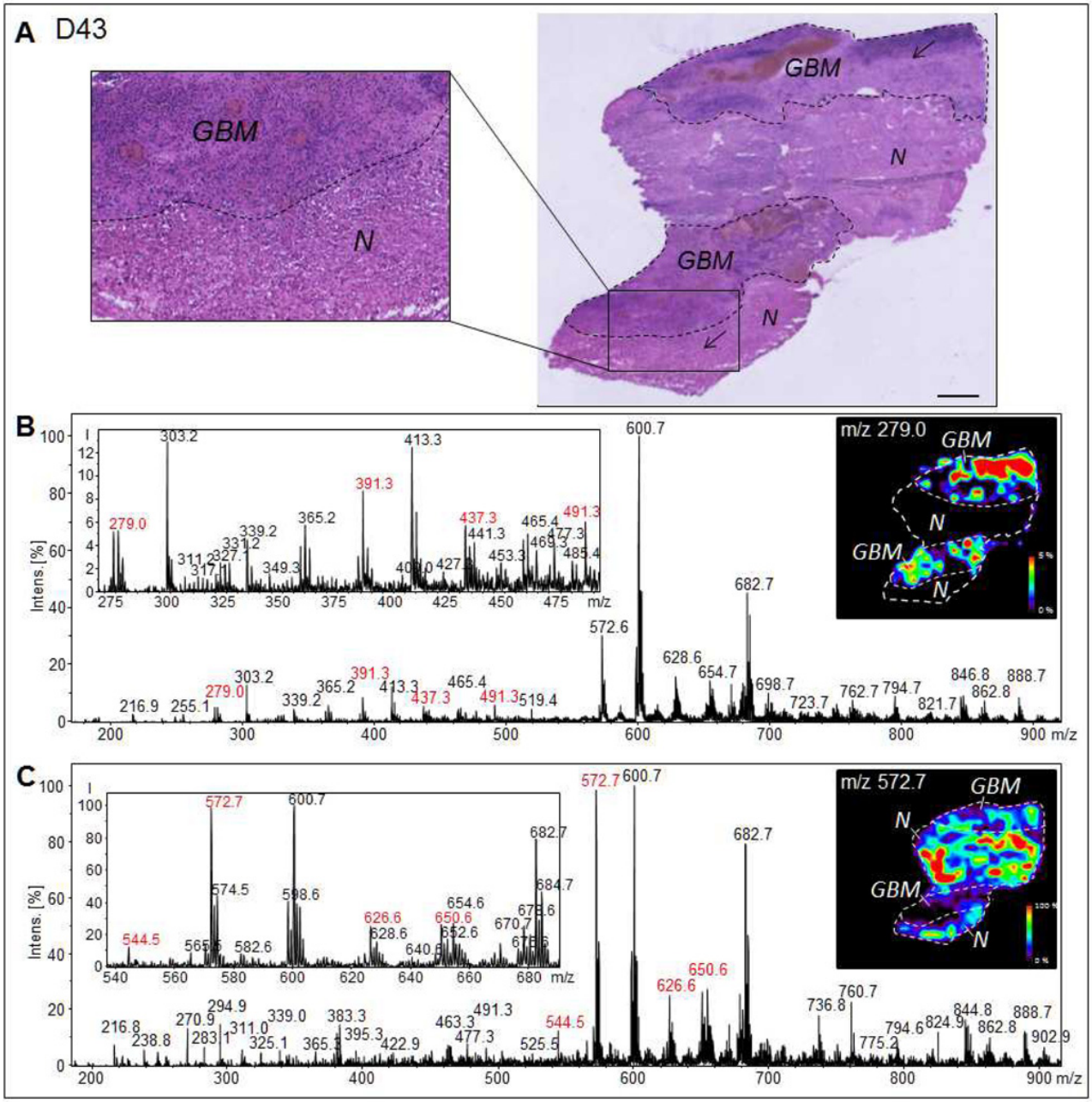

Figure 6 Necrotic and Glioblastoma tissues analysed by Mass Spectrometry (A) Optical images of a D43 section H&E stained after MSI analysis. Dotted lines on the section delineate areas of necrosis "N" and viable glioblastoma "GBM" tumor. (B) Negative ion mode mass spectrum acquired from the viable GBM area during MSI analysis (selected mass spectrum is indicated by an arrow in A). In red, m/z values corresponding to lipids species exclusively or preferentially detected in the GBM areas. Inset corresponds to a MSI ion image representing the repartition of an ion at m/z value 279.0. (C) Negative ion mode mass spectrum acquired from the necrotic area during DESI-MSI analysis (selected mass spectrum is indicated by an arrow in A). In red, m/z values corresponding to lipids species exclusively or preferentially detected in areas of necrosis. Inset corresponds to DESI-MSI ion image representing the repartition of ion at m/z value 572.7. [44]

1.3.2. Raman spectroscopy

Raman spectroscopy is based on irradiation of a sample by means of laser and recording of scattered radiation that arises from the molecular vibrations in the sample. Raman spectroscopy tests molecular vibration of asymmetric chemical bonds to detect the inelastic scattering of photons and therefore, provides information on the molecular structure and conformation of the target tissue [45].

Raman has the advantage of being insusceptible to water, which remains a problem for other spectroscopic techniques. But this is not anymore an advantage for the analysis of tissue sections in histological examinations.

Nevertheless, since there are protein content differences between tumor tissue and normal tissue, Raman spectroscopy can distinguish them at molecular level [46, 47]. Furthermore, Raman spectra can be rapidly processed and a result can be offered in real-time during the surgery

The main strength of Raman microscopy is its lateral resolution. Raman microscopy offers better spatial resolution (<1 μm) [48]. Another advantage of its high resolution is that it can be used to highlight subtle changes in small tissue substructures, such as vascular endothelial dysfunctions, abnormal inclusion of lipid droplets in cells [38], and so on. Raman has been used to investigate medulloblastoma (grade IV WHO), low-grade astrocytoma (grades I-II WHO), ependymoma and metastatic brain tumors [49] and the grading of astrocytomas [50].

In principle, the high resolution of Raman scattering should give a significant advantage to Raman spectro-microscopy for resolving small tissue substructures. However, this higher resolution is not easily exploitable.

Raman microscopy is facing three major challenges which include; big data as a result of the high resolution, longer acquisition time causing changes in ambient conditions between the moment of the background acquisition and the degradation in signal-to-noise ratio (S/N) as the acquisition resolution increase [28].

Raman microscopy is also limited by its poor sensitivity. The most-advanced studies for the analysis of tissues show that Raman spectra could provide up to 30–40 bands if an appropriate curve-fitting method is used [51], thereby limiting that only a few bands can be extracted for quantitative analyses based on a linear signal [28].

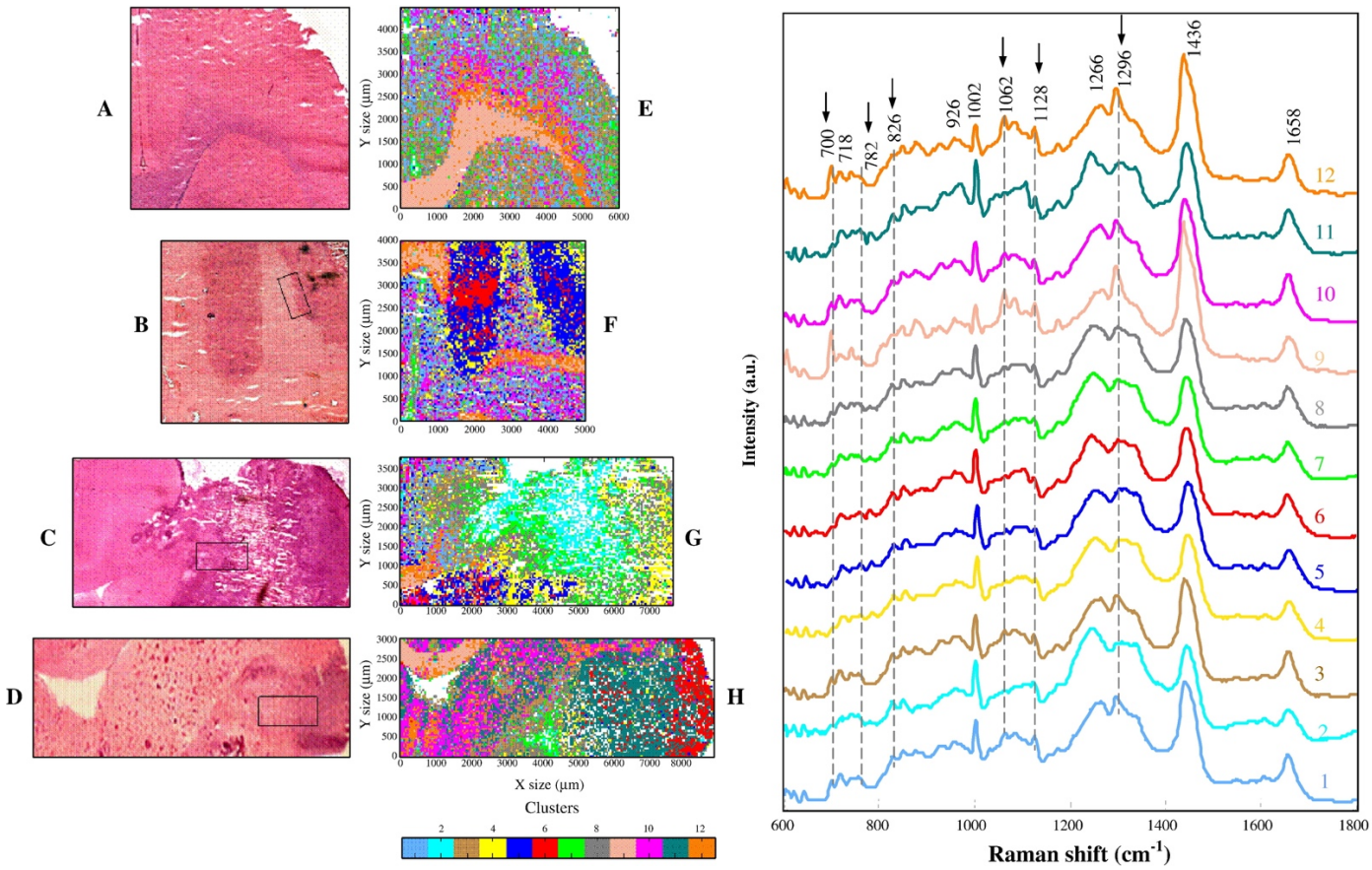

Figure 7 Discrimination of healthy and tumor tissues by Raman spectroscopy. ***(A)*** *H&E staining of healthy brain tissue section. (B–D) H&E staining of glioma brain tissue sections. Raman maps* ***E–H*** *are based on 12-means cluster analysis on sections* ***A–D****, respectively. In E, the area associated to the spatial distribution of cluster 9 correlates with white matter tissue from the corpus callosum (CC). Tissue surrounding CC was encoded by cluster 12. Other clusters (1, 3, 8, and 10) described the cortex (Gray matter). Clusters 2 and 7 described blood and could be associated to the vascularisation.* ***F to H*** *show Raman maps of glioma brain tissues. Clusters assigned to tumor tissue are clusters 4, 5, 6, 8, and 11. All clusters associated with tumor shows a decrease in the intensity of the lipids bands at 700, 1062, 1128, and 1296 cm− 1 corresponding to cholesterol and phospholipids. In contrast, other bands were more pronounced in the tumor model such as bands at 782 and 826 cm− 1 attributed to DNA and/or RNA. [52]*

1.3.3. Mid-Infrared Spectroscopy

Mid-Infrared (Mid-IR) spectroscopy is a technique based on the vibrations of molecules. An infrared spectrum is typically obtained by passing infrared radiation through a sample and determining what fraction of the incident radiation is absorbed at a particular energy. In complex biological systems, the IR spectrum is the sum of the contributions of the biomolecules present (e.g. proteins, lipids, sugars and nucleic acids) [53], creating a molecular fingerprint of the sample. The fingerprint of no two molecular structures produce the same infrared spectrum.

Mid-IR spectroscopy has an advantage of allowing rapid mapping of potentially a wide range of chemical information in a non-supervised pattern without prior sample labeling Mid-IR spectroscopy offers a higher signal-to-noise ratio (S/N) than Raman and thus more chemical parameters for analysis. While Raman has a higher spatial resolution than Mid-IR should be generally more stable than Raman because of its higher signal-to-noise-ratio. It also has the advantage of a relatively simple and affordable instrumentation [54].

Mid-IR microscopy is particularly well suited for tumor imaging as it provides high contrast between healthy and tumor tissues, which are usually characterized by major redistributions between proteins and lipids contents [27]. The technique of FTIR spectral mapping is able to detect subtle chemical changes in tumors indicative of tumor progression and for identifying prognostic indicators [55]. Mid-IR microscopy has been used in the mapping of tumor progression in tissues [53] and to discriminate between malignant and normal tissues [56, 57].

While Mid-IR microscopy has shown a lot of promise and comparative advantage over other spectroscopies for brain tumor diagnosis, however, it is currently underexploited despite its potential. This is due to several limitations of current commercial Mid-IR instruments.

These limitations include; relatively high spatial resolution compared to a technique like Raman spectroscopy which offers spatial resolution of <1-μm, relatively lower molecular details compared to a highly sensitive technique like MSI, the bottlenecks of using cooled IR detectors, long acquisition time for large tissue and the interpretation of spectra data.

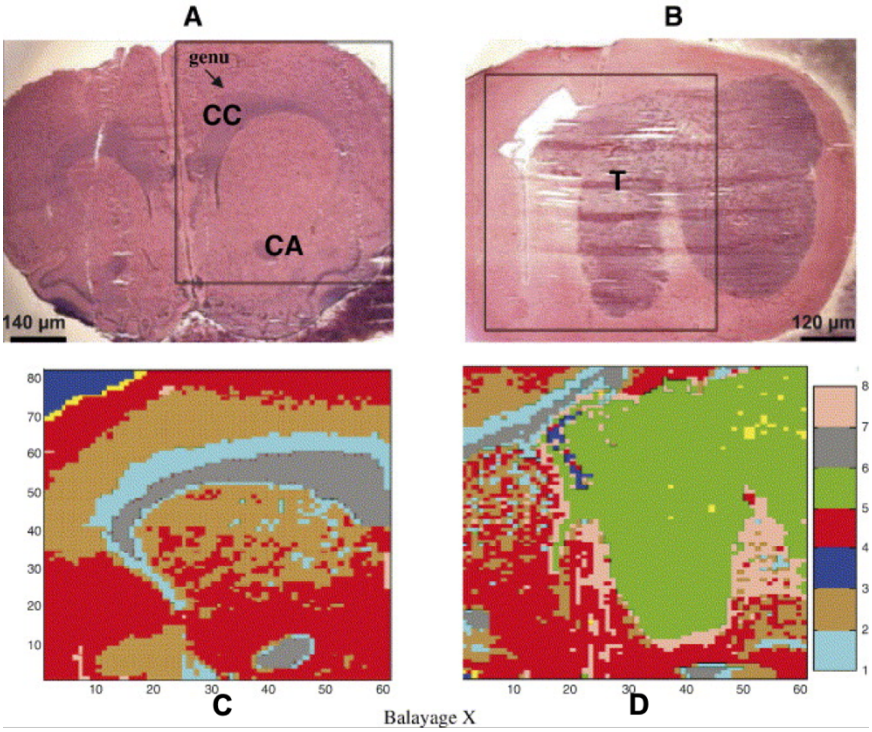

Figure 8 FTIR comparison of healthy and glioma tissue. Photomicrography of HE stained healthy brain tissue (A) and glioma tissue (B) sections. (A) shows, particular structures can be recognised such as CC that appears as a "V" shape with the genu (apex) pointing medially, and CA. In figure B, the more intensely stained area, marked "T" represents tumor zone. The pseudo-color FTIR maps (C) and (D) were obtained from the measured areas marked with a black frame on the adjacent unstained healthy (A) and glioma (B) tissues, respectively. Pseudo-color FTIR maps were constructed on 8-means clusters. Each cluster (consisting of similar spectra) was assigned to one brain feature. Blue: denotes areas in the scan where no tissue was present; yellow, red, brown and cyan: Cortex areas; grey: CC and CA areas; green: tumor tissue area; pink: infiltrative zone. [58]

Technique	**Penetration depth (μm)**	**Lateral resolution (μm)**	**Spectral interval, (resolution)**	**Field of view ($\mu m \times \mu m$)**	**Tissue area covered /min (μm^2)**	**Accessible chemical data**	**Refs**
IR	30	5-10	500-4000 cm^{-1}, (2-8 cm^{-1})	2000 x 2000	800 000	100-200	[27, 59]
Raman	50	4-32	100-4000cm^{-1},(0.5-4 cm^{-1})	Single point volume	70 000	50-100	[60, 61]
MSI	0.01	10-100	500-10000 m/z, (1-10 m/z)	Single point volume	1 500 000	100-1000	[62, 63]

Table 1 Comparison of the analytical performance of micro-spectroscopic techniques. While analyzing frozen tissues, the main analytical performances vary by technique: IR (section thickness: 5–25 mm; best 3D resolution: 10 mm;); Raman (section thickness: 5–40 mm; best 3D resolution: 5 mm;); MS (section thickness: 5–50 mm; best 3D resolution: 10 mm) [28]

1.4. Mid-IR microscopy for cancer biology

Around 1800, Harschel studied the spectrum of sunlight using a prism and measured the temperature of each color. He found that the highest temperature was just beyond the red, what we call now infrared. The electromagnetic spectrum of the IR region is conventionally divided into three parts

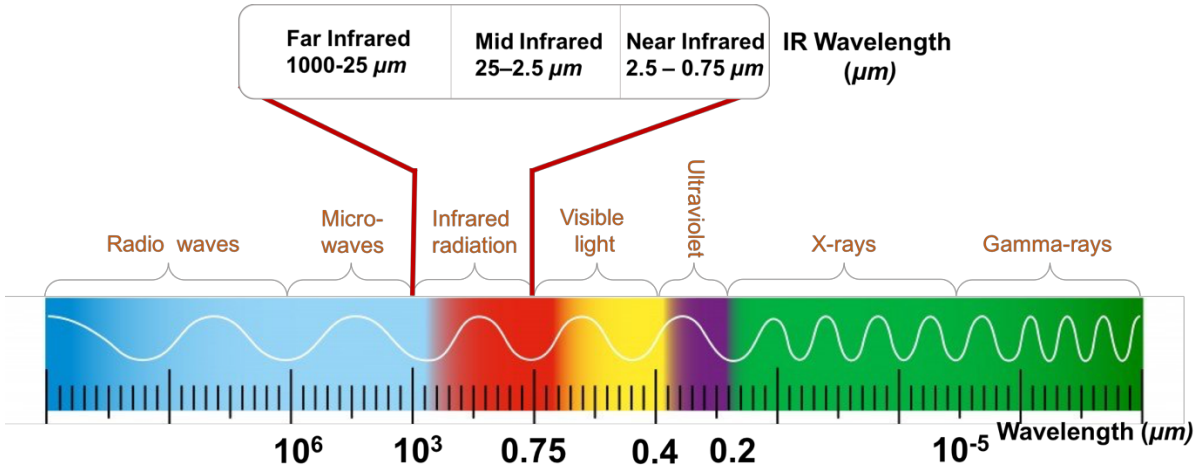

Figure 9 Electromagnetic spectrum: Showing IR divided into the far, mid and near regions and their corresponding wavelengths

Mid-IR spectroscopy basically deals with the mid-infrared region 4000–500 cm^{-1} (2.5–25µm wavelength) which is the most informative for biosamples since these reveal vibrations of molecular bonds from organic compounds, although the far-infrared approximately 400–10 cm^{-1} (25–1000µm) and near-infrared 14,000–4000 cm^{-1} (0.75–2.5µm) have also provided some benefits [64].

Since the middle of 20th century, Mid-IR spectroscopy coupled to microscopy (IR micro-spectroscopy) has been recognized as a non-destructive, label free, highly sensitive analytical method with many potential useful applications in different fields of biomedical research and in particular cancer research and diagnosis [65].

The coupling of an IR spectrometer to an optical microscope offers the unique opportunity for studying biological samples with a spatial resolution limited by the near diffraction limit of infrared light (5-10µm).

1.4.1. FTIR Spectrometer

IR spectrometry has evolved from the use of dispersive instruments which were generally slow and did not allow the measuring of all infrared frequencies simultaneously. Fourier Transform Infrared (FTIR) spectrometry was developed in order to overcome the limitations encountered with dispersive instruments.

A solution which employed a very simple optical device called an interferometer. It could measure all frequencies in a given spectral range, commonly 4000-500 μm for the mid-IR region, and with high spectral resolution, down to 1 cm^{-1} or better.

Most interferometers employ a beamsplitter which takes the incoming infrared beam and divides it into two optical beams. One beam reflects off of a flat mirror which is fixed in place. The other beam reflects off of a flat mirror which is on a mechanism allowing it to move on a short distance (typically a few millimeters) away from the beamsplitter.

The two beams reflect off of their respective mirrors and are recombined when they meet back at the beam splitter. Consequently, the path that one beam travels is a fixed length and the other is constantly changing as its mirror moves, the signal which exits the interferometer is the result of these two beams interfering with each other.

The resulting signal is called an interferogram which has the unique property that every data point (a function of the moving mirror position) which makes up the signal has information about every infrared frequency which comes from the source. This means that as the interferogram is measured, all frequencies are being measured simultaneously.
However, the measured interferogram signal cannot be interpreted directly because the analyst requires a frequency spectrum (a plot of the intensity at each individual frequency) in order to make an identification. A means of "decoding" the individual frequencies is required.

This can be accomplished via a well-known mathematical technique called the Fourier transformation. This transformation is performed by the computer which then presents the user with the desired spectral information for analysis [66].

All modern IR spectrometers use FTIR and are composed of the following common elements: an internal IR light source, the interferometer (basically a Michelson interferometer), and a single element detector connected with an amplifier and a computer [67].

1.4.2. FTIR Microscope Setup

The FTIR microscope is basically a spectrometer coupled with a microscope. The FTIR microscope is similar to visible light microscope but it does not employ glass refractive elements (glass is opaque to IR light of $\lambda > \sim 5\mu m$). For this reason, FTIR performed in transmission requires that probing samples are deposited on optical windows (e.g. ZnSe, CaF_2, and BaF_2 crystals) that do not absorb, or absorb very low mid-IR radiation and have very high values of transmittance within a wide range of frequencies in the mid-IR region.

IR radiation from the spectrometer is focused onto a sample placed on a standard microscope x–y stage. After passing through the sample, the infrared beam is collected by a cassegrain objective which produces an image of the sample within the barrel of the microscope.

In the first FTIR microscopes, a variable aperture is placed in this image plane produced by the cassegrain objective in order to define the area of analysis. The radiation is then focused on to a small-area detector by another cassegrain condenser.

The microscope also included glass objectives to allow visual inspection of the sample. In addition, by switching mirrors in the optical train, the microscope can be converted from transmission mode to reflectance mode.

In the early 1990s, FTIR microscopes were equipped with a single MCT detector. This enabled just the analysis of a single section, single spot, defined by the aperture of the microscope [68]. In order to get a high lateral resolution, the minimal aperture dimension is set to approximately 10µm x 10µm. With this set-up it is possible to investigate spectroscopically single cells, which allows the classification of "normal" versus malignant cells in a medical diagnostic-like analysis [54, 68, 56].

The drawback of this procedure is that the investigation of larger sample areas, using a reasonable lateral resolution (between 10-40µm), is extremely time consuming (taking up to days for larger samples in the cm range analyzed at a lateral resolution of 10-40µm) [69].

The breakthrough came for FTIR microscopes when array detectors became accessible [70, 71, 72]. The use of a focal plane array (FPA) detector instead of using a single MCT detector reduced the experimental time drastically for the investigation of a larger sample area. Additionally, using these detectors superior image fidelity was gained.

FPAs are made of many small, individual pixels laid out in a grid pattern. FPAs are typically available in 64x64, 128x128 and 256x256 grids (larger arrays are currently proposed). The predominantly utilized MCT detector array size is 64 x 64 pixels, allowing the acquisition of 4096 infrared spectra per experiment [65, 68].

Each small pixel functions as a single small detector. For the imaging setup, no apertures are necessary to define the analyzed sample area. The microscope images of the sample plane are directly projected onto the detector array, and thus simultaneously from each pixel of the FPA, spectral data are collected from a specific sample region within the field of view using the coupled spectrometer.

This setup proved to be a cutting edge technology when it was introduced and enabled the successful application of FTIR to samples from a variety of cell lines [73], blood cells [74], tissues [75], cervix [76], breast [77], prostate [78], lung [79], colon [80], brain [53, 81], skin [82], esophagus [83], liver [84], lymph system [85] and stem cells [86].

The results of all those studies have clearly indicated that FTIR associated with the use of some appropriate statistical data analysis methods has an accuracy in classifying normal and malignant tissues/cells in the order of 80-100% [68].

However, in spite of its many advantages, the application of FTIR to cancer research and clinical diagnostics continues to be promising or immature and to the best of my knowledge, no FTIR microscope has been put in clinical trials for cancer screening or diagnosis to date.

This is due to some bottlenecks associated with this setup have hindered the progression of FTIR to become a routine tool for clinical diagnosis. These bottlenecks can be summarized into three major problems which include, reproducibility of spectra at high S/N ratio, lack of standardized protocols for spectral data treatment and the suitability as a tool for 3D pathology [87].

1.4.3. High-throughput and Reliable IR System

One major bottleneck associated with the FTIR system is the difficulty of maintaining and reproducing spectra with high S/N ratio for large tissues at the dimension of clinical biopsies (frequently $1cm^2$). At diffraction limited resolution, i.e. about 5-10μm for the mid-IR range, the acquisition of $1cm^2$ tissue area will be too long (hours) at sufficient spectral quality (S/N ≥100) for routine cases [27].

In order to maintain high S/N ratio, as defined by the ratio of source power (SP) to the noise power (NP), in the FTIR setup, enough IR signal must be cumulated on the detector by performing a number of scans in continuous mode within the selected interval of wavenumbers (e.g. from 4000 cm-1 to 600 cm-1) at a selected scanner velocity (e.g 40 kHz).

Therefore, to increase S/N values, a possible solution is to modify the source power, SP, that is to increase the brightness or IR light source.

1.4.3.1. IR Sources

(a) Globar Source

The most common IR source is a Globar source. A silicon carbide rod 5–10 mm-wide and 20–50mm long that can be electrically heated up to 1000–1650^{o}C. Globars were introduced as IR sources inside FTIR equipment in the mid-1960s, but have not been modified further. They have been observed to have a weak photon flux [87]. This paved way for the use of synchrotron source for FTIR instruments.

(b) Synchrotron Source

Since the 1980s, the lack of commercially available powerful IR sources has pushed spectroscopists to use the synchrotron radiation IR beam [87]. Synchrotron radiation FTIR provides a higher signal/ noise ratio at the highest spatial resolution because of its intense brightness [88], thereby permitting intracellular imaging of molecular chemical structure and compared to globar IR light sources [89].

However, a major bottleneck is that synchrotron light sources are extremely cost-intensive due to the high consumption of energy and it is not feasible to use the full power of synchrotron IR radiation without damaging the thin silicon-based film of IR detectors.

Also, in spite of synchrotron radiation having photon flux that is 2–3 orders of magnitude higher than Globar in transmission, this powerful source could not provide more than a 10–20% increase in S/N ratio [90]. A lack of correlation between increases in source power and signal level is partly due to the limited sensitivity of commercially available IR detectors [87].

Recently, in order to overcome this limitations of FTIR system, high-spectral-brightness, broadly tunable IR laser source with a large-format (480 × 480), uncooled microbolometer FPA detectors has been developed [91].

1.4.3.2. Quantum Cascade Laser IR

Quantum cascade lasers (QCL) are semiconductor lasers that emit in the mid- to far- infrared portion of the electromagnetic spectrum. QCL provides higher spectral radiance than the synchrotron source and significantly more than the standard Globar source. In quantum cascade structures, electrons undergo inter sub-band transitions and photons are emitted. The electrons tunnel to the next period of the structure and the process repeats.

Therefore, unlike IR interferometers, QCLs generate the mid-IR signal wavelength-by-wavelength in absolute values and the spectrum reconstruction does not require the Fourier transform anymore (thus reducing mathematical approximations in absorption calculations) [92], and provides absolute count of photons on detector, thus ensuring more accurate quantitative analysis of biosamples.

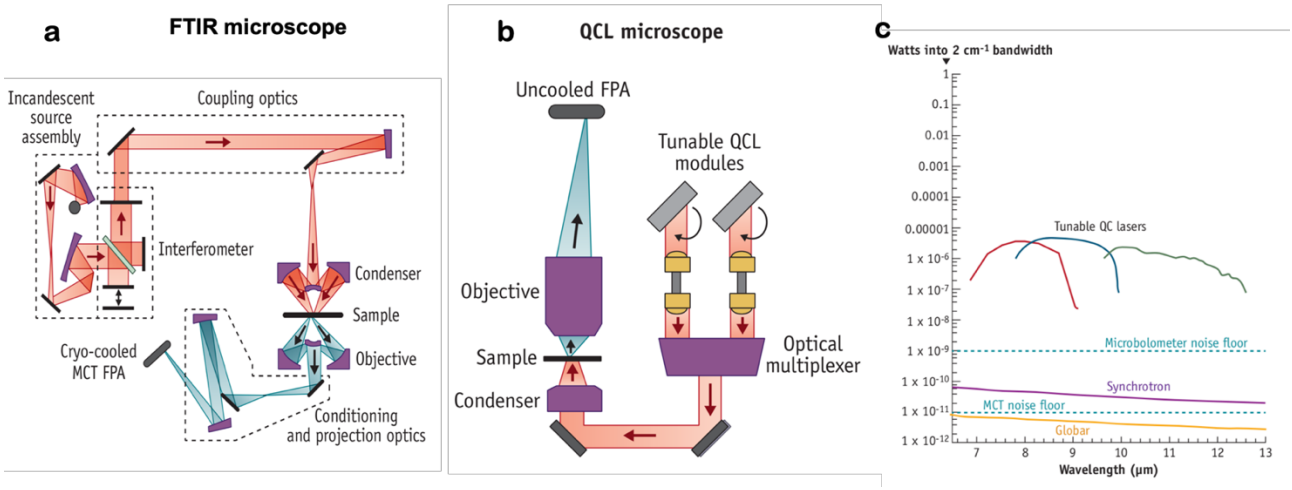

Figure 10 Setup of different kind of IR microscope and their respective spectral brightness. a) FTIR microscope setup. (b) QCL-IR microscope setup. (c) Spectral brightness of globars, synchrotron IR source, and QCL 1403BOWbarreF2 lasers over the 7–12 μm (833–1430 cm^{-1}) range difference in relation to the noise floors of commercial MCT and microbolometer FPAs [91]

Because of this wavelength-by-wavelength signals generation, obtaining a large spectral region may take time, but the development of pulsed lasers working in the ms range is compensating the periodic mode of signal generation [93].

QCL-IR microscope setup

The main components of QCL-based IR microscopes, as shown in Figure 10, include multiple QCL modules, an optical multiplexer, a condenser, a switchable objective, an automated stage, and an uncooled large microbolometer FPA (480 × 480). The architecture enables a small footprint, currently about one third that of a commercial FTIR microscope.

The laser source comprises multiple broadly tunable external cavity QCL modules that enable platform modularity and scalability. The high brightness of the QCL source takes advantage of the full dynamic range of commercial uncooled microbolometer FPAs having 14 times the number of pixels found in state-of-the-art FTIR microscopes. However, it is limited to a shorter spectral interval of 1800-830 cm^{-1}.

The QCL-IR and FTIR microscopes have been recently compared [27, 94]. The S/N ratio was found to be approximately 50% higher with a single scan using the QCL-IR system than with the best acquisition condition (1000 scans) for the FTIR system.

The comparison is even more striking if we consider that the tissue area covered by a single FPA tile dimension acquisition, is 340 x 340 μm^2 for the FTIR system (2.66 x 2.66 μm^2/pixel) and 2000 x 2000 μm^2 for the QCL-IR system (4.3 x 4.3 μm^2/pixel).

The QCL-IR has also been observed that the QCL-IR could be up to 150x faster than FTIR in acquisition time of a large tissue of 7mm diameter. However, it also observed that the coherence of laser sources modifies the shape of the spectral data resulting from sample measurements [27].

Specification	FTIR	QCL-IR
Resolution (cm^{-1})	1-16	4 and 8
Spectral range (cm^{-1})	4000-400	1800-830
Detector size (mm	40 x 40	17 x 17
FPA type (pixels, condition)	128 x 128 N_2-cooled	480 x 480 Uncooled
FPA coverage (mm)	5.12 x 5.12	8.16 x 8.16
Mag. levels	15X 36X	4X 12.5X
Final pixel size (mm)	2.66 x 2.66 1.1 x 1.1	4.25 x 4.25 1.36 x 1.36
FOV (mm)	340 x 340 140 x 140	2000 x 2000 650 x 650

Table 2 Comparison of the basic specification of FTIR and QCL-IR microscopes showing the improved capabilities of the QCL-IR. The FTIR however offers a larger spectral range compared to the QCL. [28]

The reduction in the acquisition time on large sample areas as well as the use of uncooled FPA detector enables the acquisition of reproducible, and thus reliable quantitative data from tissue samples and development of analytical techniques for diagnostics. This is giving to IR microscopy a unique advantage over other analytical techniques, notably for the ability to determine absolute concentrations of chemical and molecular species in biosamples.

1.4.3.3. IR data treatment

One of the challenges of spectroscopic techniques remains the complexity of spectra data for end users who are not specialists of their utilization, i.e. for clinicians and biologists. The data treatments developed for extracting chemical information from raw spectra remain in the domain of expertise of spectroscopists (interpretation of spectral data as biological information) or use multivariate statistics do not cross-match the usual standards of pathologists, i.e. recognizing anatomical features or labeling specific antigens on the tissue sections. Thus there is a need for the development of IR data treatment protocols that can be used by onco-pathologists for characterization and diagnosis of tumor.

The IR spectrum is defined by bands with an important overlapping between them in some spectral regions . The major marker peaks are the Amide I and Amide II characterizing the contents in proteins and polypeptides. Amide I band has a centered absorption at ~1650 cm^{-1} and identifies primarily the C=O stretching modes, vC=O, associated with vibrations of a secondary amide, whereas Amide II band absorbing at ~1550 cm^{-1} refers to the combination of both N-H bending and C-N stretching vibrations. Not only Amide I and Amide II identify protein molecule but their positions and shapes may reflect changes in the secondary protein structure [95].

In Table 3, we present the region of absorption of different biomolecules that have been identified and assigned as major spectral components by functional group analysis. Functional group analysis is particularly useful for the qualitative analysis of pure organic molecules since the IR spectrum of each molecule is unique and it can serve as a signature to distinguish among different molecules, for instance, proteins, nucleic acids, lipids and fatty acyl chains, and saccharides [65, 96].

However, an IR spectrum of a biosample contains a large number of bands, many of which will be impossible to confidently assign to the vibration of a particular functional group or to a given molecule. Moreover, cells contain many mid-IR active molecular constituents such as membrane lipids and phospholipids, glycolipids, proteins, glycoproteins, phosphoproteins, nucleic acids, carbohydrates and a variety of small metabolites that may concur to spectral features. Therefore, there is a need for advanced spectral data treatment such as spectral band decomposition and curve fitting [96] to isolate these bands individually.

Vibrational mode (functional group)	**IR frequency (cm^{-1})**	**Molecular information**
Amide A, B	3300, 3100	Fermi resonance between N-H stretch and overtone of Amide II, sensitive to secondary structure
n(-C1⁄4C-H) stretch	3010	Fatty acyl chains unsaturation
$n_{as}(-CH_3)$ stretch	2960	Predominantly due to proteins
$n_{as}(-CH_3)$ stretch	2875	Predominantly due to fatty acyl chains
$n_{as}(>CH_2)$ stretch	2924–2916	Predominantly due to lipid, frequencies qualitatively
$n_s(-CH_3)$ stretch	2870	Predominantly due to lipid, frequencies qualitatively
$n_s(>CH_2)$ stretch	2855–2848	Monitor acyl chain conformational order and packing
n(>C1⁄4O)	1730–1760	Due to acid carbonyls
n(>C1⁄4O)	1740–1720	Due to ester carbonyl, sensitive to hydrogen bonding
Amide I	1685–1630	Predominantly due to C1⁄4O stretch, sensitive to secondary and tertiary structures
n(>C1⁄4O)	1684, 1672, 1664, 1656, 1645, 1637, 1625, 1610	Proteins, b-turns, antiparallel b-sheets, parallel b-sheets, a-helix, unordered structure, a-like triple helix, antiparallel b-sheets, parallel b-sheets
n(-C1⁄4C-)	Weak	Sensitive to conjugation
Amide II	1550–1530	Predominantly due to N-H in-plane bend and C-N stretch, sensitive to secondary structure
$d(>CH_2)$, $d(-CH_3)$	1475–1460	Methylene modes in IR sensitive to acyl chain packing
$n_s(>COO^-)$	1450–1400	Due to NMF components and amino acid side chains
$v(>CH_2)$	1337	IR marker for Pro in collagen
$t(CH_2)$		Trans acyl chain
Amide III	1275–1235	C-N stretch and N-H in-plane bend, sensitive to secondary structure
$n_{as}(P=O)$	1227	Phosphates

Table 3 Major IR and Raman band assignments for Soft Tissues. [28]

1.4.3.4. IR Data Treatment Methods

There are several different methods for the analysis of IR spectra for chemical information extraction: from the simple inspection to identify peaks to, chemometrics; where mathematical, statistical, and computer sciences methods are applied to improve the understanding of chemical information contained in typically broad and complex IR data. Here we discuss the different methods used for IR data treatment.

(a) IR data pre-processing

Pre-processing is required in order to reduce and correct interferences that may generate irrelevant variances such as atmospheric water vapour and carbon dioxide, variable background absorption profiles, and differences in sample thickness. Background intensity changes along the interval of wavenumebers that may alter the baseline are usually compensated by appropriate mathematical methods for baseline correction.

Baseline Correction

An infrared spectrum typically consist of chemical information, baseline and random noise [97]. In an ideal condition the baseline of a spectrum should be a flat line, however, most of the time, the baseline is not flat; it has a linear or nonlinear distortion [98]. It is important to correct baseline distortions because it varies more or less randomly between spectra in a IR spectrum matrix, which in turn creates problems for analytical comparison of spectra and visualization of chemical information due to the problem of vignetting that arises as a result of varying intensities across the spectrum matrix.

The distortion in baseline also affects the spectral resolution and peak assignments. Baseline correction also helps to get rid of strong outlying artifact signals in the spectrum matrix. Mathematical methods such as polynomial fitting and rubberband method have been proposed for IR spectra baseline correction [97, 98, 99].

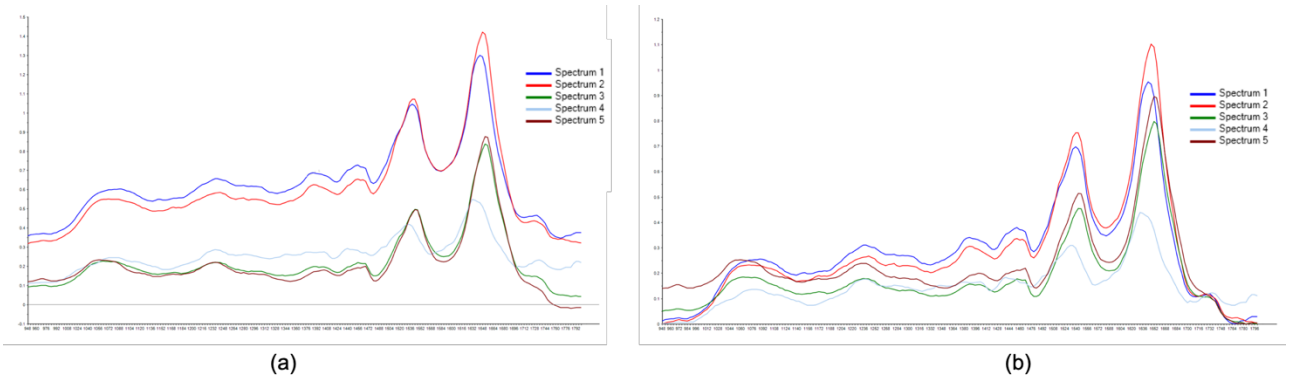

Figure 11 Baseline correction of IR spectra in order to make spectra data comparable and eliminate strong outlying artefact signals. (a) IR spectra with uncorrected baselines. (b) Baseline correction of the purple spectrum by polynomial fitting.

(b) Derivative Spectra

Numerical differentiation with respect to wavelength for qualitative analysis and for quantification. could also be performed on spectra.

If a spectrum is expressed as absorbance, A, as a function of wavelength, λ, such that $A = f(\lambda)$,

The derivative spectra in the first order can be expressed as:

$$\frac{dA}{d\lambda} = f'(\lambda) = \frac{A_{\lambda+\Delta\lambda} - A_{\lambda}}{\Delta\lambda} \quad (1)$$

The second order derivative can be expressed as:

$$\frac{d^2A}{d^2\lambda} = f''(\lambda) = \frac{A_{\lambda-\Delta\lambda} - 2A_{\lambda} + A_{\lambda+\Delta\lambda}}{\Delta\lambda^2} \quad (2)$$

The third order derivative can be expressed as:

$$\frac{d^3A}{d^3\lambda} = f'''(\lambda) = \frac{A_{\lambda-\Delta\lambda} - 3A_{\lambda} + A_{\lambda+\Delta\lambda} + A_{\lambda+2\Delta\lambda}}{\Delta\lambda^3} \quad (3)$$

The fourth order derivative can be expressed as:

$$\frac{d^4A}{d^4\lambda} = f''''(\lambda) = \frac{A_{\lambda-\Delta\lambda} + A_{\lambda-2\Delta\lambda} - 4A_{\lambda} + A_{\lambda+\Delta\lambda} + A_{\lambda+2\Delta\lambda}}{\Delta\lambda^4} \quad (4)$$

A first-order derivative is the rate of change of absorbance with respect to wavelength. A first-order derivative starts and finishes at zero. It also passes through zero at the same wavelength as λ_{max} of the absorbance band. Either side of this point are positive and negative bands with maximum and minimum at the same wavelengths as the inflection points in the absorbance band. This bipolar function is characteristic of all odd-order derivatives [100].

The most characteristic feature of a second-order derivative is a negative band with minimum at the same wavelength as the maximum on the zero-order band. It also shows two additional positive satellite bands either side of the main band. A fourth-order derivative shows a positive band. A strong negative or positive band with minimum or maximum at the same wavelength as λ_{max} of the absorbance band is characteristic of the even-order derivatives [100].

Derivative techniques are widely used in spectra analysis for background correction and molecular specificity [100, 101, 102]. The spectral resolution is enhanced when the first derivative is computed since changes in the gradient are examined. Second derivative

spectrum is a technique widely used to enhances the separation of overlapping peaks and reveals the positioning of peaks [102].

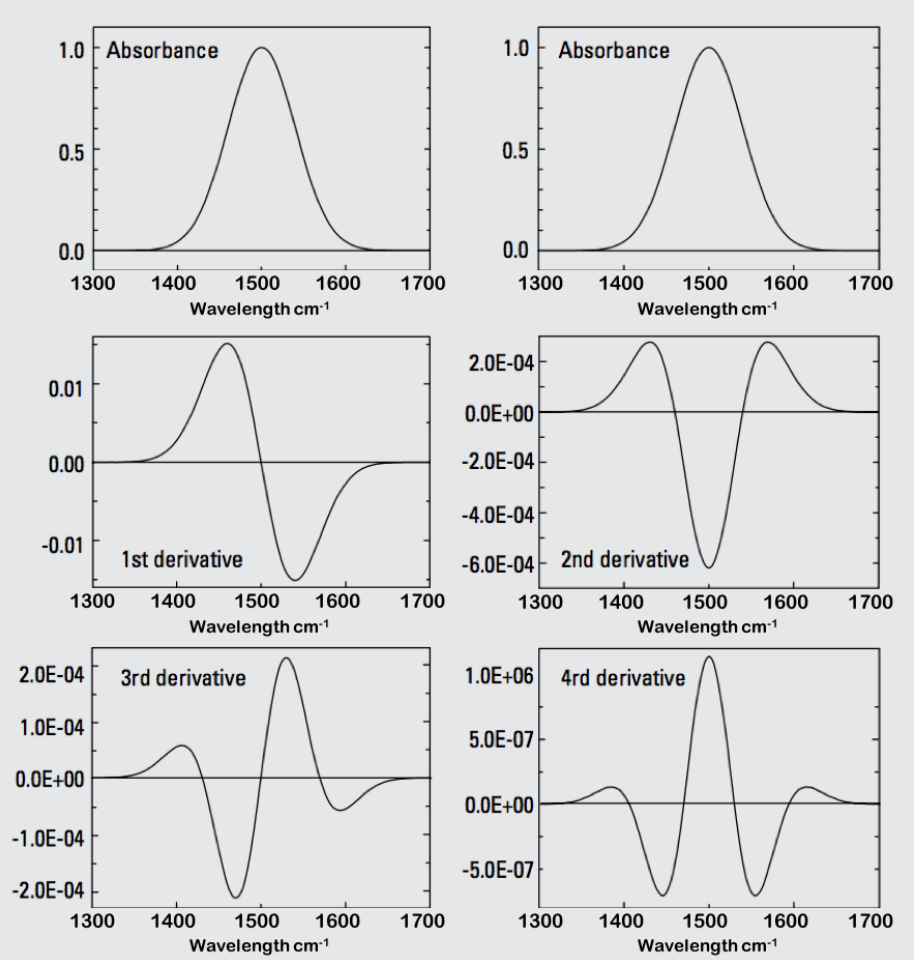

Figure 12 Derivative of a spectrum showing the 1st, 2nd, 3rd and 4th derivative spectrum. The 2nd derivative is characterized with negative peak at the λ_{max} while the 1st derivative passes through zero at λ_{max}. The 3rd derivative shows the characteristic bipolar function of odd-order derivatives with positive and negative bands at either side of the λ_{max}.

(c) Band Integration

IR spectra can also be subjected to numerical integration. A spectrum consists of bands which are series of equally spaced wavenumbers in a regular sequence. A IR spectrum typically consists of well-defined bands such as amideI, amideII, lipids, phospholipids, carbohydrates.

Mathematically, the area covered by these bands can be computed by performing numerical integration. This is useful to compute the distribution of these bands in the biosample.

Let $f(x)$ be an IR spectrum from a biosample, the integral of a band bounded by wavelengths [a, b] is defined as;

$$\int_a^b f(x)dx \tag{5}$$

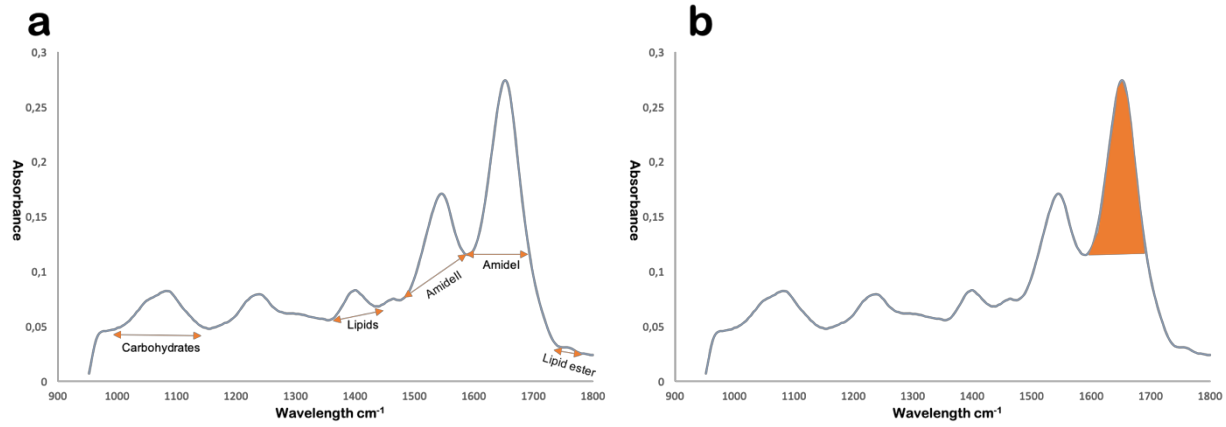

Figure 13 IR band integral of the AmideI band. a) IR bands showing different bands in soft tissues. (b)Integration of the AmideI band $\int_{1596}^{1708}$

(d) Multivariate Analysis

Multivariate pattern recognition methods compare a large number of variables (e.g. absolute and relative intensity, the position, and the width of one or more absorptions) within a dataset. The IR spectra of biosamples are very complex since they consist of the overlapping absorption of the main biomolecules.

In order to retrieve the significant and non-redundant information contained in the spectra, it is necessary to apply an appropriate multivariate analysis method which are able to process very high-dimensional data. Generally, multivariate classification with supervised or unsupervised pattern recognition can be applied to IR spectra [65].

The popular multivariate analysis techniques are principal component analysis (PCA), principal component regression (PCR), partial least squares (PLS), discriminant analysis (DA), cluster analysis (CA).

PCA is a non-parametric method for extracting relevant information from confusing data sets allowing to identify patterns in data and to highlight their similarities and differences [103]. PCA reduces the dimensionality of spectra data into principal components by maintaining as

much variance as possible [104]. Major benefit of PCA is that the large number of initial dimensions are condensed to only a few dimension (principal component), those reflecting the most relevant analytical information [105]. It can also be combined with discriminant analysis as PCA-LDA for classification into different categories.

Figure 14 shows an example of classification of embryonic stem cell spectra of different differentiation days. This figure highlights the limitations of PCA as a spectrum can belong to multiple classes in poorly differentiated cells.

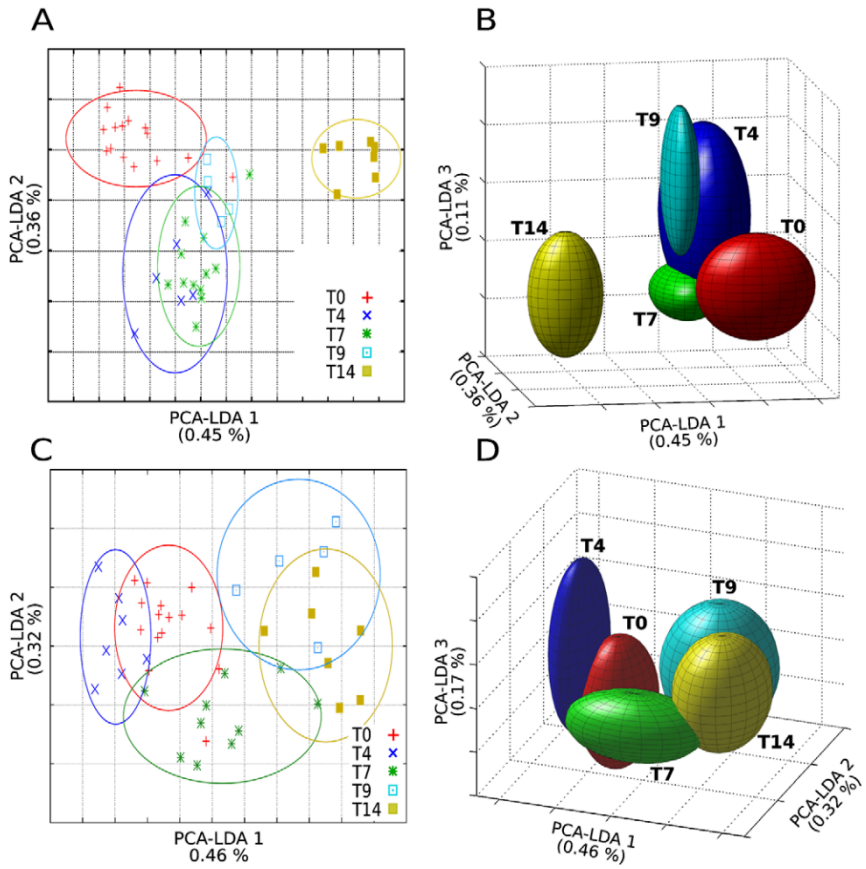

Figure 14 PCA–LDA of Embryonic stem cell differentiating second derivative spectra. Clustering of second derivative spectra from 1800 to 800 cm^{-1} is reported as 2D (A) and 3D (B) score plots. Clustering of second derivative spectra in the lipid absorption region from 3050 to 2800 cm^{-1}: 2D (C) and 3D (D) score plots. On each PCA–LDA component, the percentage of the explained variance is reported. Represented data correspond to 4, 7, 9 and 14 days of differentiation. Clusters are represented as ellipses in the 2D plot and ellipsoids in the 3D. The semi-axes of ellipses/ellipsoids in the 2D/3D plots correspond to two standard deviations of the data. [106]

PCR is a method used together with PCA. Once a set of k principal components has been obtained using the PCA method, they can be used as input variables for a multivariate regression analysis instead of the original data. By eliminating correlations in the original data, the PCR method allows to perform linear regression on spectra data.

PLS regression searches for a set of components that explain as much as possible the covariance between spectrum in the spectra data. In this way, compared to the PCR, the principal components contain more information about the relationships between predictors and dependent variables. For classification into different categories, the PLS method takes the name of partial least square discriminant analysis (PLS-DA)

(e) Spectral decomposition

Spectral Band decomposition and curve fitting is used to decompose and determine the quantitative values of underlying or narrow bands in heavily overlapped bands. While multivariate analysis provides useful information about the variance of spectra data, the nature of variance on global spectra does not reflecting individual molecular variations. Thus there is a need for a method which is able to decompose bands into individual

Spectral Band decomposition and curve fitting helps to condense spectra data into few band parameters. This important for spectral feature extraction as it helps to approximate the quantitative value of smaller bands that have been merged into bigger ones.
Band decomposition and curve fitting seeks to extract a series of bands as a Model $M = \{B_b, b \in [1...N]\}$ which is representative of all the chemical compound present in a sample.

In order to define standard protocols for the interpretation and presentation of IR spectra and images, methods must be defined for extracting the distribution of different biomolecules and translating them into biological metadata that are within the domain of onco-pathologists. This is referred to as spectromics.

Spectromics is defined as the ability to exploit any spectral information (or set of spectral information using any kind of mathematical procedure) for characterization of biosample (from chemical to molecular, biological, and anatomical tissue contents) [107].

The development of data treatment methods for quantitative IR microscopy and spectromics enables the reconstruction of a 3D quantitative chemical images of a biological tissue by IR spectro-microscopy which opens the way to 3D digital pathology (Figure 15).

1.5. Towards large scale 3D pathology

Three-dimensional (3D) microscopy is a powerful approach for imaging biological specimens and is the next frontier for modern histopathology. It offers excellent spatial resolution and facilitates the observation of tissue sub-structures and content under physiological and pathological conditions.

3D pathology is expected because tissue blocks are not naturally transparent, and they contain complex 3D networks (blood and lymph systems, membranes, nerves and other fibers, etc.), a 3D arrangement of different cell phenotypes that is not homogeneous, and an extracellular space that is composed of many other compounds and filamentous structures. From a geometric point of view, it is possible in principle to instantly visualize tissue abnormalities using 3D pathology and it has significant advantages compared to the usual 2D histology.

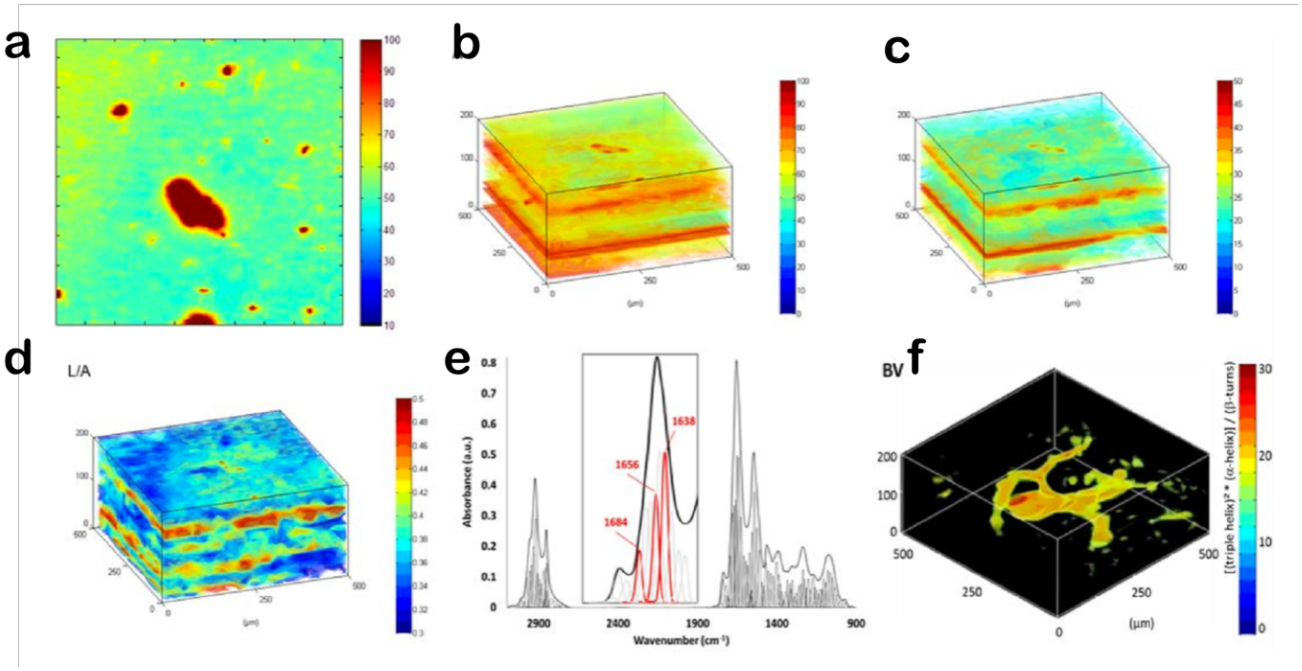

Figure 15 3D IR image reconstruction for spectral-derived features of tissue sub-structures. (a): 2D IR image of single wavelength absorption (1424 cm^{-1}) revealing blood vessels in a tissue section of mouse brain. (b-d): Stacked 3D IR images for 20 consecutive tissue section (10 µm thickness) showing the distribution of Amide I, lipids and lipids/amideI(L/A) ratio. (e) curve-fitted spectrum showing extractable IR-bands and zoom on the 1750–1600 cm^{-1} spectral interval for selecting bands allowing to reconstruct the blood vessel network BV in (f) [26]

Figure 15 shows the feasibility of the 3D reconstruction of the chemical parameters of tissue sub-structures. However, this was done empirically by manual handling of the 3D reconstruction of IR images for only 20 consecutive slices of 10 µm thickness. To extend this empirical approach to scale in clinical applications, it means moving from few spectra to billions of spectra.

Computing the 3D volume of this big data is not trivial. Thus, the effort required becomes exponential compared to the reconstruction of blood vessel network of a region of interest in a small sample and thus requires the automation of the processes.

For the new QCL-IR to be considered for use in clinical diagnosis of tumours, it must be developed for 3D imaging of tissues. Although IR microscopy is not suitable for direct tomographic measurements on biosamples because IR photons have limited depth of penetration in matter, biosamples also contain >60% of water with unmanageable absorptions, and the transmission measurements do not allow resolving absorptions in a true confocal geometry. However, its quantitative nature should allow the reconstruction of a 3D matrix of spectra of large samples [108].

As a result of a fast and high S/N level spectra acquisitions from several tissue slices, QCL-IR microscopy should allow reconstructing a large 3D matrix of IR spectra for tissue analyses. To achieve 3D reconstruction, spectral data treatment methods that allows discrimination of two objects (e.g. healthy vs. pathological tissue or sub-structures inside the same tissue volume) must be developed.

Different spectral data treatment methods have been developed so far to extract chemical information from spectra using individual IR band or well-identified regions of the IR spectrum such as amide I region. The 3D reconstruction of these data might provide unique information about a tissue, with 3D resolved sub-structures correlated to biochemical or metabolic events [107].

This would lead to the combination of morphological and molecular data into the same 3D image of a biosamples, thus comparable to the MRI/CT or PET/CT multimodal imaging methods, but with unique advantage of being quantitative and using a single technique to perform 3D reconstruction at the microscopic scale without the use of any label or imaging contrast agent, thus avoiding sample manipulations and alterations.

Figure 16 shows a proof of concept for 3D reconstruction of brain tumors. This was achieved using 20 consecutive tissue slices. The slices were manually aligned in order to visualize the spatial arrangement of the tumor in the mouse brain. In this thesis we will develop a processing sequence for automating the process of resolving billions of spectra at the scale of the whole mouse brain and computing 3D volume of tumors and tissue sub-structures.

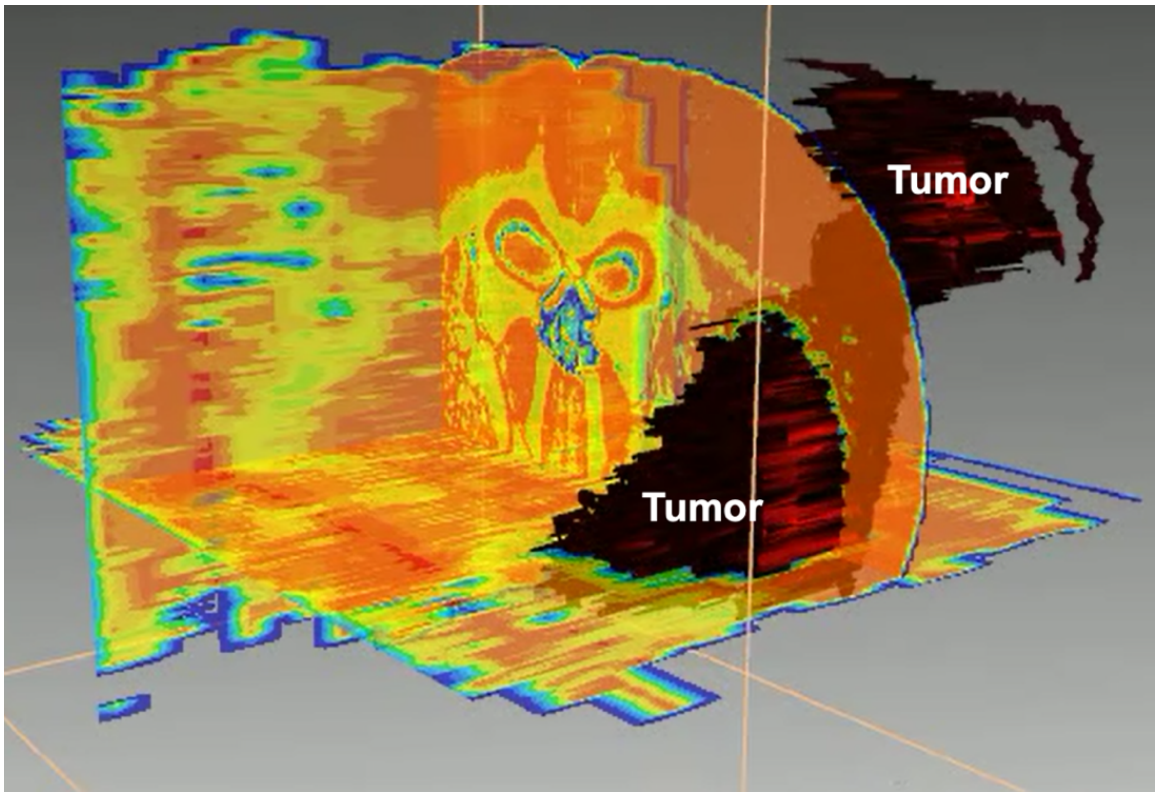

Figure 16 Example of 3D reconstruction of mouse brain tumor using 20 brain tissue slices. The development of IR imaging for large scale 3D pathology would allow the reconstruction of the tumour in the whole mouse brain.

CHAPTER 2: Techniques for 3D reconstruction of histological images

Three-dimensional (3D) histology is a powerful approach for microscopic imaging biological specimens and is the next frontier for modern histopathology. This is due to the inherent limitations of conventional 2D histology.

Histology permits the observation of structures of the internal topography of a specimen which are invisible at macroscopic scale. Although it enables the investigation of tissues at a cellular level, it is invasive and breaks topology due to sectioning.

Three-dimensional (3D) reconstruction of 2D histological slices was thus introduced to overcome the limitations of single-section studies in a dimensional scope. Three-dimensional (3D) reconstruction and examination of tissue at microscopic resolution have significant potential to enhance the study of both normal and disease processes, particularly those involving structural changes or those in which the spatial relationship of disease features is important [109].

In this chapter, we present a review of the development of 3D histology and the different image processing techniques required for 3D reconstruction histological images.

2.1. From 2D to 3D Histopathology

3D pathology is expected because tissue blocks are not naturally transparent, and they contain complex 3D networks (blood and lymph systems, membranes, nerves and other fibers, etc.), a 3D arrangement of different cell phenotypes that is not homogeneous, and an extracellular space that is composed of many other compounds and filamentous structures.

From a geometric point of view, it is possible in principle to instantly visualize tissue abnormalities using 3D pathology and it has significant advantages compared to the usual 2D histology [110].

It offers excellent spatial resolution and facilitates the observation of tissue sub-structures and content under physiological and pathological conditions. In cancer application, tumour size,

including maximum tumour diameter and tumour volume may be more accurately measured in 3D compared to 2D for diagnostics.

Visualization of 3D histology volume can also help the pathologist when they report the orientation of the tumour or when investigating the spatial relationship between the distributions of different disease biomarkers(Figure 17).

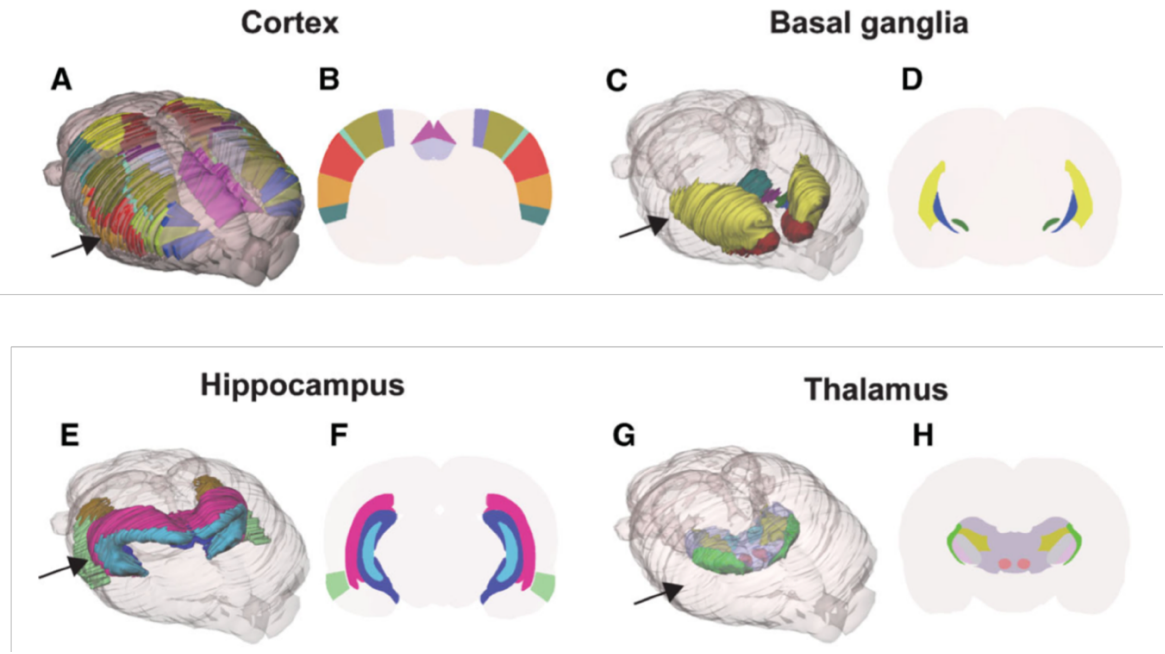

Figure 17 3D reconstruction of mouse brain anatomy showing true location, structural and spatial arrangement of different anatomical features in 3D compared to a 2D view where no information about the location of the structures are known. A-B: 3D reconstruction of the mouse brain cortex. C-D: 3D reconstruction of the basal ganglia region. E-F: 3D reconstruction of the hippocampus region of the mouse brain. G-H: 3D reconstruction of the Thalamus region of the mouse brain [111].

3D histology also reduces significantly misinterpretation that occur in 2D assessment of complex networks such as microvasculature. Particularly in the setting of restructured microvasculature during disease, where vessel and network morphometry cannot be predicted.

In contrast to large and medium-sized vessels that can be embedded and sectioned in specific directions, the orientation of arterioles and venules of the microvasculature cannot be determined from conventional 2D histological images [112].

In order to extend histological examinations from 2D to 3D, one faces a major problem of how to regain information of the structures in 3D from a series of 2D samples. Volume slicing breaks the spatial relations between structures and creates discontinuities which hamper intuitive representations in 3D and thereby, a full understanding of the sample anatomy.

Moreover, in 3D pathology, it is also mandatory to consider soft tissue distortions due to tissue removal by surgery or biopsy. The shape of the tissue is considerably altered via cryomicrotomy, and the final 3D reconstruction model that is created from serial 2D sections will be significantly distant from reality.

In addition, tissue sub-structures are independently and randomly altered due to the current manual nature of cryomicrotomy. This may result in anatomically different structures looking similar in microscope slides and conversely, slicing may cause one same structure to have different views if not consistent.

These alterations are collectively called as artefacts [113]. Artefacts include, loss of details, folds and wrinkles, cracks and holes. These alterations could result in misinterpretation of histological images as they are capable of altering the morphology tissue structures as well as result in inconsistent contrast of similar tissue structures (Figure 18).

For quantitative analyses in 3D pathology, the determination of the molecular concentrations as well as the distribution of tissue sub-structures will be directly dependent on the recovery of the native 3D shape of the tissue. While current manual methods of histology make artefacts inevitable, however, they are surmountable.

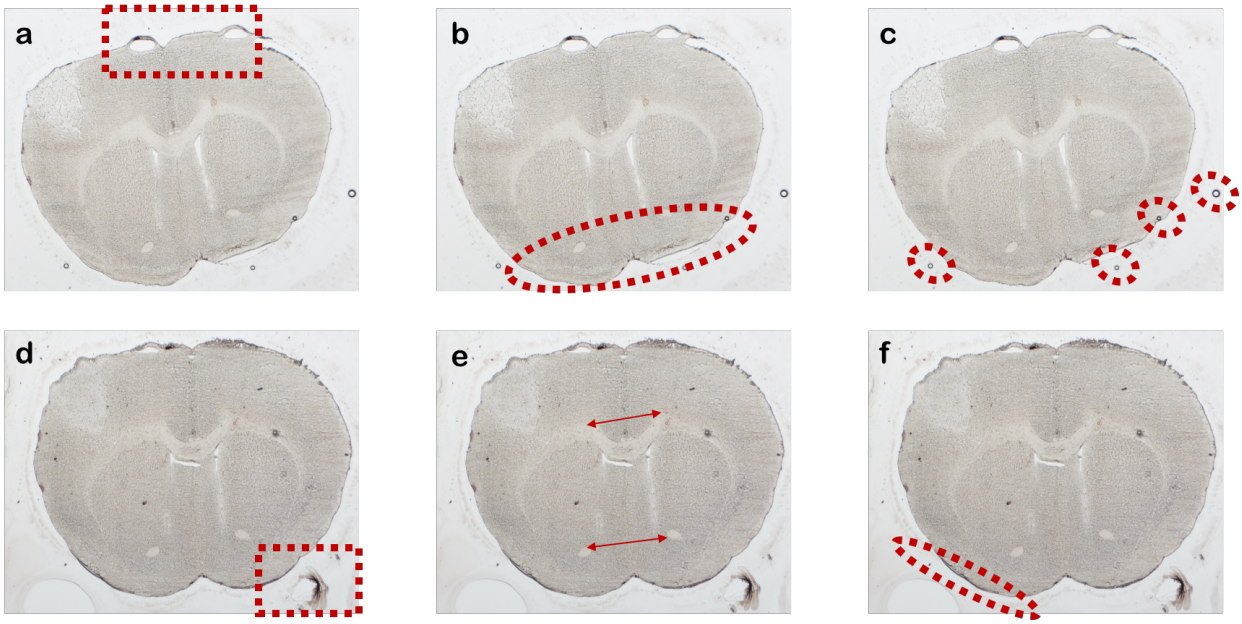

Figure 18 Problems associated with 2D histological images. (a) Tears and holes in tissue slice. (b) Global shape deformation of tissue slices. (c) Artefacts in and around tissue slice. (d) Glue deposited on sample slide. (e) Local misalignment of tissue substructures. (f) Vignette arising from difference of thickness around tissue edges.

In the light of these problems, several techniques have been proposed for 3D reconstruction of histological images [113]. These includes, techniques to solve major alterations in 2D histological images, combining non-invasive imaging with histology to relate macroscopic information to the underlying microscopic properties of tissues through the establishment of spatial correspondences and recovering of sectioning axis for 3D reconstruction.

Typically, 3D reconstruction of histological slices follows a classical image processing pipeline to solve the problems listed above (Figure 18). This consists of 3 major processes which includes; image pre-processing to resolve the problems introduced by histological sample preparation, image information retrieval process where useful information such as anatomical landmark is determined and extracted in the histological images, post-process where the extracted anatomical landmarks are refined for reconstruction.

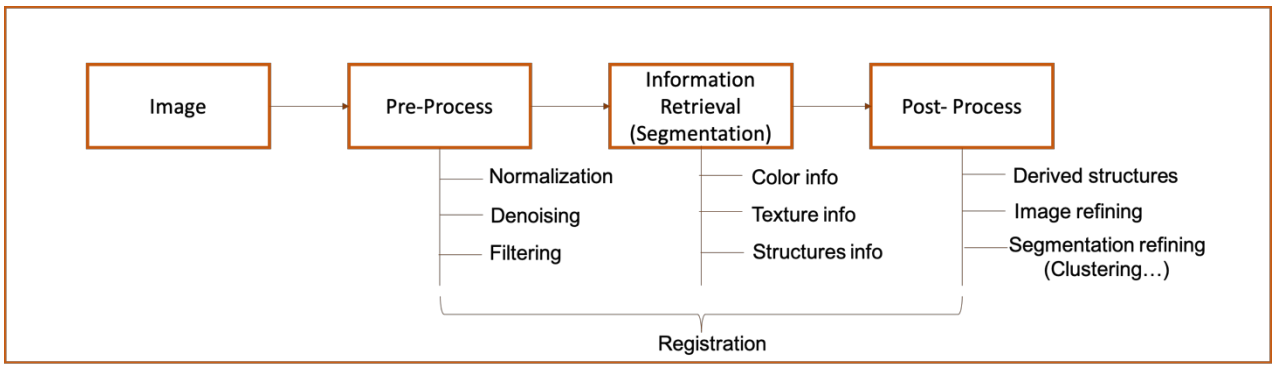

Figure 19 Typical image processing pipeline for histological image processing. This pipeline includes methods for image pre-processing such as grey scale level normalization, segmentation methods and image post-processing methods such as clustering to group into different intuitive classes.

2.2. Image pre-processing techniques for 3D digital histopathology

Image pre-processing techniques are required to solve the problem of artefacts on histological slices before 3D reconstruction. Two major problems that can be addressed by image pre-processing methods are the variation in intensity due to slight difference in tissue thickness and resolution of cracks, holes and tears in tissue sections.

2.2.1. Intensity normalization

Ideally, the absolute colour of a slide reveals the biological component that a pathologist wishes to retrieve. For example, in the case of H&E, the colour value quantifies the amount of nucleic acids (blue-purple) hematoxylin has bound to, and the amount of proteins (in pink) Eosin has bound to. However, due to the presence of artefacts or because of optical aberration from microscope and the camera used for imaging [114] slides tend to exhibit different colours.

In general, histology reconstruction methods require the use of greyscale images for intensity standardization (or the channel that provides the best contrast in an RGB image) across the series of 2D histological images. This is due to the use of differences in intensity as one of the criteria used for identifying salient structures and finding correspondence between series of histological images.

Histogram equalization [115, 116] method has been used to correct inhomogeneous intensity in a single histological slice.

Histogram Equalization

A definition of image contrast is the difference in luminance (brightness) or colour that makes an object distinguishable. Histogram equalization is a technique used to enhance the contrast of images and correct inhomogeneous brightness by manipulating the distribution of intensities on the image histogram.

This involves computing the histogram of the individual color channels and luminance values, as shown in Figure 20. From this distribution, we can compute relevant statistics such as the minimum, maximum, and average intensity values.

Histogram is the basis for numerous spatial domain image processing techniques and could be characterized by flat and bell shape (Figure 20). Bell shaped specification usually represents a normal distribution. This type of specification usually appears to have one cluster that much of data cluster around which results in inhomogeneous intensities. On the other hand, flat specification is indicative of a uniform distribution of intensities.

Mathematically, to compute the equalized histogram of an image, the probability density function and cumulative density function of the input image histogram is computed. These functions are then

applied for modifying the input image intensity levels to generate a processed contrast enhanced image.

Histogram equalization could however be subject to bias in the presence of extreme outliers. To correct the bias, methods that seek to normalize slices by using multiple slice references have also been proposed for normalizing intensity of serial histological sections [117, 118].

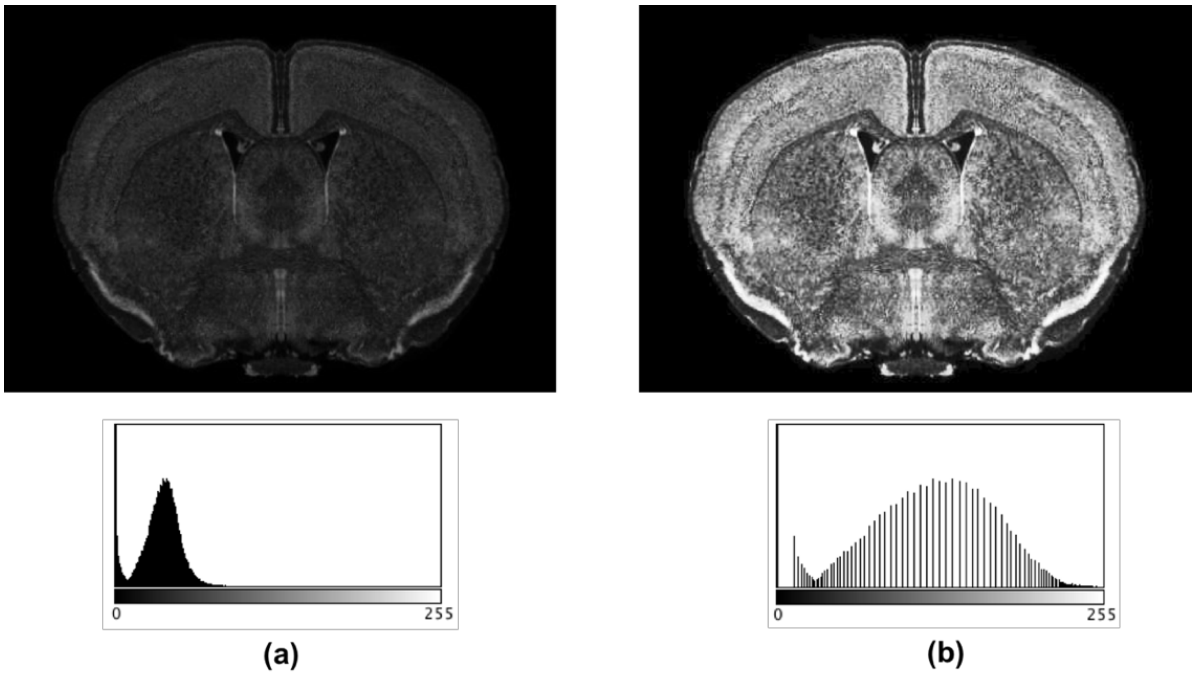

Figure 20 Histogram Equalization example. (a) Tissue sample with bell shaped closely clustered distribution of image intensities. (b) Contrast enhanced image by uniformly distributing the intensities.

2.2.2. Tissue Alterations

The problem of alterations such as tissue cracks, tears or holes within the tissue are more challenging to solve than the variations in intensities. This is particularly challenging because of the need to assert if the hole is an anatomical feature or an aberration due to histology.

Consequently, manual delineation of the torn area is the standard procedure to identify torn parts of a tissue [119]. This is followed by the use of the image histogram to identify the intensity class of the surrounding tissue to fill up the missing parts. Depending on the geometry or size of the tear, different methods can be used to fill up the crack and holes. Like intensity normalization, holes and cracks can be corrected using a single image or multiple histological images.

For a single histological image with the assumption of the horizontality of tears, a manual contouring of the torn area and filled it by repeating pixel values of the contour along the columns of that region can be used to fill up the holes and cracks (Figure 21) [120]. Landmark correspondence could also be determined between multiple images to stitch cracks, holes and torn pieces in a slice [119].

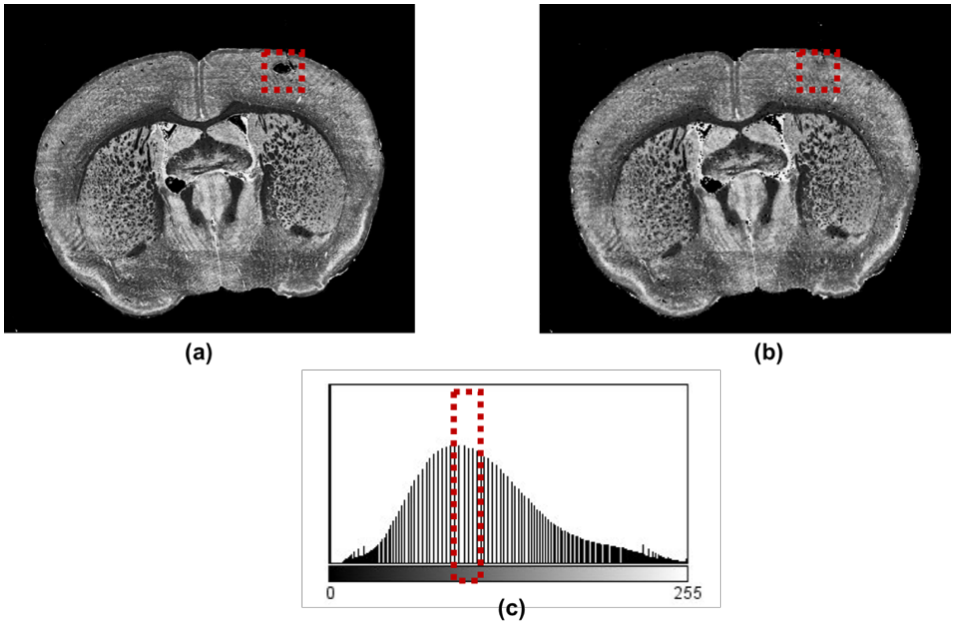

Figure 21 Tissue hole correction example. (a) Tissue with manual delineation of hole region by the dotted red box. (b) Corrected hole using the average intensity of neighbouring pixels computed from the boxed region in the image histogram (c) Image histogram showing the pixel distribution of the boxed region in the image (a).

2.3. Image segmentation techniques for histological images

Image segmentation helps to understand histological images by extracting information from the image. In practice, it is often interested in some certain areas which have the same characteristic. Typically, an image segmentation algorithm is based on certain criteria to divide an input image into a number of the same nature of the category.

An application for analysis of histological images is for both correction of aberrations during sample preparation such as glue deposit and for extracting meaningful information such as anatomical structures, delineating the border of disease in tissues, cell counting etc.

Segmentation methods could be based on simple global information of the image such as image histogram or more complex information such as topology, geometry and texture [121, 122]. Methods of segmentation such as thresholding [123] [124] [113], edge segmentation, segmentation using active contour [125] and segmentation using morphological operators [126] are relevant for histological image segmentation.

One of the most common segmentation methods is the use of thresholds. It is a characterization of pixel intensities belonging to a specific object. It directly divides the histogram. Threshold method could be local or global in domain. The global threshold method divides the image into two classes of the background and foreground while the local threshold method uses multiple segmentation thresholds and divides the image into multiple target regions and backgrounds (Figure 22).

An advantage of the threshold method is its low computation complexity. The disadvantage is that it is difficult to obtain accurate results for image segmentation problems where there is no significant intensity difference or a large overlap of the intensity values in the image [122].

This is as a result of taking into account just the intensity information of the image without considering the spatial information of the image. It is sensitive to noise and grayscale unevenness, leading it often combined with other methods using morphological operators (such as opening, erosion or dilation) to refine the results of thresholding [126].

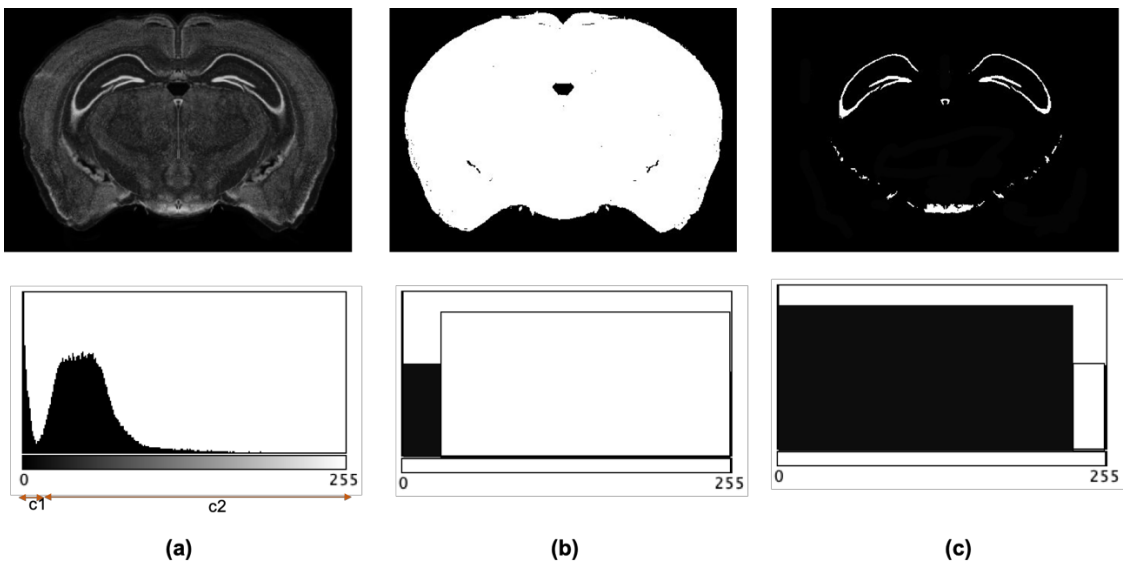

Figure 22 Threshold segmentation example. (a) Original image with histogram divided into 2 classes of white and black pixels. (b) Retrieving the tissue mask by thresholding the background pixels (class c1) and foreground pixels (class c2). (c) Using threshold segmentation to segment anatomical landmark from the whole tissue.

Generally, there is no ideal segmentation method, the choice of method depends on specific image requirement and targeted information. Below is a table comparison of different image segmentation methods and their application to histological image segmentation.

Method	Description	Advantages	Disadvantages	Application
Thresholding [127]	Based on the histogram peaks of the image to find particular threshold values	(1) It does not require prior information of the image. (2) Low computation complexity.	(1) Does not work well for an image without any significant intensity difference. (2) Does not consider the spatial details, so cannot guarantee that the segmented regions are contiguous	Tissue masking, Anatomy extraction, Contrast enhancement
Edge detection [128]	Based on the detection of discontinuity, normally tries to locate points with more or less abrupt changes in gray level.	Intuitive and works well for images having good contrast between regions	(1) Does not work well with images in which the edges are ill-defined or there are too many edges (2) Less immune to noise than other techniques, e.g., Thresholding and clustering	Tissue masking, Anatomy extraction, Disease Delineation, Cell counting
Distance Clustering [128]	Assumes that each region in the image forms a separate cluster in the feature space. Can be generally broken into two steps: (1) categorize the points in the feature space into clusters; (2) map the clusters back to the spatial domain to form separate regions.	Straightforward for classification and easy for implementation	(1) How to determine the number of clusters. (2) Does not utilize spatial information (3) Time consuming	Tissue masking, Anatomy extraction, Tissue classification, Disease Delineation

Method	Description	Advantages	Disadvantages	Application
Region based [129]	Group pixels into homogeneous regions. Including region growing, region splitting, region merging or their combination	Work best when the region homogeneity criterion is easy to define. They are also more noise immune than edge detection approach	(1) Are by nature sequential and quite expensive both in computational time and memory (2) Region growing has inherent dependence on the selection of starting region and the order in which pixels and regions are examined	Tissue masking, Tissue classification, Disease delineation
Active Contour [130]	Based on the use of image information to evolve a segmenting curve (deformable/smooth contours) which match to various object shapes and motions.	(1) Useful to track and fit non-rigid shapes. (2) Can allow user interaction.	(1) Cannot effectively handle intensity inhomogeneity. (2) Result dependent on the initial contour and parameters. (3) Long runtime	Tissue masking, Anatomy extraction, Disease Delineation.
Blob analysis [131]	Based on the analysis of image topology for continuous connected components, holes and borders.	(1) Can correctly segment the objects, even though a part of the boundary is missing or many noisy regions accompany the object. (2) Geometrical operations can be performed directly using shape information.	Does not work well with images with complex shape network or when there are too many shapes.	Tissue masking, Anatomy extraction, Disease Delineation, Cell counting,

Table 4 Comparison of different segmentation methods and their applications for histological image [130, 127, 128, 129].

2.4. Registration methods for 3D histology reconstruction

The basic foundation of all histological reconstruction approach is image registration. Regardless of the approach chosen for reconstruction, image registration methods are needed to establish correspondence and spatially align the set of histological slices.

Registration is the process of bringing two images, one usually referred to as “reference” and the other as “source” into spatial alignment and deforming the source image such that it looks like the reference image [113].

The objective is to estimate the transformation that optimizes an energy function. It is usually made of two terms, one referred to as the matching criterion and a regulator which helps to control the extent and type of transformation applied.

At its simplest, image registration involves estimating a mapping between a pair of images (reference and source images). The reference image is assumed to be spatially ‘stationary’ or ‘correct’ and used as a reference image to which the source image is mapped.

The mapping between both images can be considered as a function of a set of estimated transformation parameters of the image coordinate used to spatially align both images [132].

2.4.1. Image Transformation Models

The transformation model defines how the source image can be deformed to match the reference image; it characterizes the type and number of possible deformations [133]. A transformation model uses the coordinates of corresponding control points in two images to estimate the geometric relation between the images, which is then used to transform the geometry of source image to that of the other to spatially aligned the images [134].

The most used transformation model is the rigid, affine and deformable transformation. Rigid and affine transformations are global transformation model, i.e. applied to the whole image. They are particularly useful in reconstruction of serial histological slices because they largely satisfy the rigid

body constraint. On the other hand, deformable transformation model corrects the local deformation of the source image.

(a) Rigid Transformation

Rigid transformation in two dimensions is defined by two parameters; translation and rotation. A translation moves every point of an image or a geometric space by the same magnitude in a given direction. If a point $\boldsymbol{x}$ is to be translated by $\boldsymbol{q}$ units, then the transformation is simply:

$$y = x + q \tag{6}$$

Rotation is defined a motion of a certain space that preserves at least one point. It can be described as the motion of a rigid body around a fixed point. It differs from translation which is a motion that does not requires a fixed point.

Consider an image rotated at point coordinate (x, y), by an arbitrary angle θ, translated on the $x - axis$ by a magnidute unit of q and by a magnitude unit of k on the $y - axis$. The rigid transformation of the image is expressed as:

$$\begin{aligned} X &= \mathrm{x}\cos\theta - y\sin\theta + q \\ Y &= \mathrm{x}\sin\theta + y\cos\theta + k \end{aligned} \tag{7}$$

(b) Affine Transformation

Affine transformation is an extension of rigid transformation and are typically used in instances of rigid body movement where the image scaling factors are unknown or suspected to be incorrect.

In affine image registration global scaling (i.e. shrinkage and expansion) and global skewing are also allowed, but parallel lines remain parallel in the transformed image. Affine registration of histology images is therefore suitable for correction of shrinkage and expansion of the tissue sections. The matrix equation for affine transformation is similar to the rigid transformation with the addition of scale (S) and skew (K) factors to the function.

$$\begin{bmatrix} S_x\cos\theta & -k_y\sin\theta & t_x \\ k_x\sin\theta & s_y\cos\theta & t_y \end{bmatrix} . \begin{bmatrix} x \\ y \end{bmatrix} = \begin{bmatrix} xs_x\cos\theta - yk_y\sin\theta + t_x \\ xk_x\sin\theta + ys_y\cos\theta + t_y \end{bmatrix} \tag{8}$$

(c) Deformable Transformation

Deformable or non-rigid registration corrects the local deformation of the source image. Deformable registration finds a displacement field or a deformation map for the pixels of the source image and can vastly change the shape of the objects in the source image.

Local deformation of tissue sections can be corrected in the histology images by using deformable registration techniques. There are different approaches to model the local deformation of tissue.

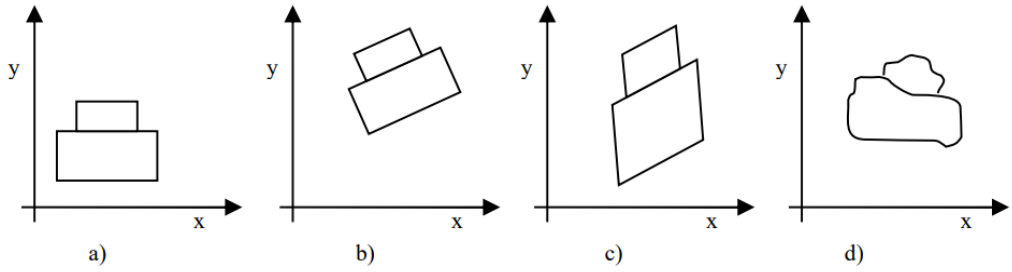

Figure 23 Image transformation models. (a) Source image. (b) Rigid. (c) Affine (d) Deformable

Several methods have been proposed for image registration of histological images and have been classified using different taxonomy based on certain criteria [135, 136]. Here we introduce some image registration methods that are used for histological images reconstruction classified based on their mechanism of establishing correspondence between images and volumes and the nature of their transformation.

Here, we classify the methods for image registration into three categories; the rigid and affine transformation based methods which is used for global registration of histological slices, the feature based methods which uses salient features in histological slices for registration and local motion estimation methods which considers the pixel level displacement between histological slices.

2.4.2. Rigid and affine transformation based methods

Rigid and affine transformation based methods estimate the translation, rotational, scaling and skew parameters to align the source image. They are used for global registration, i.e. applied to the whole image. They are particularly useful in reconstruction of serial histological slices because they largely satisfy the rigid body constraint. These methods assume that an image is a rigid body that can be subject to motion within its geometric space.

(a) Phase Correlation

The phase correlation method [137] is a frequency domain technique used to estimate the delay or shift between two copies of the same signal. This method has been easily extended to 2D and 3D images, and has been successfully applied in several image registration problems [138, 139].

Phase correlation provides straight-forward estimation of rigid translational motion between two images, which is based on the Fourier shift property [140]. The Fourier shift property states that a shift in the spatial domain of two images results in a linear phase difference in the frequency domain of the Fourier Transforms (FT).

Given two 2D functions $g(x, y)$, $h(x, y)$ representing two images related by a simple translational shift Δx in horizontal and Δy in vertical directions, and the corresponding Fourier Transforms are denoted $G(u, v)$ and $H(u, v)$. Thus,

$$H(u, v) = G(u, v)e^{-i(\Delta xu + \Delta yv)} \tag{9}$$

This means that the images have the same Fourier magnitude, while the phase difference is directly related to their spatial displacement.

The phase change $Q\ (u, v)$, is defined as the normalized cross power spectrum between G and H, which is a matrix:

$$Q(u, v) = \frac{G(u, v)H(u, v)^*}{|G(u, v)H(u, v)^*|} = \ e^{-i(\Delta xu + \Delta yv)} \tag{10}$$

where $*$ denotes complex conjugate and $Q(u, v)$ has the phase corresponding to the phase difference of the images.

Thus, the translation shifts $(\Delta x, \Delta y)$ can be estimated in the spatial domain by taking the inverse Fourier transform of the phase difference. The inverse Fourier Transform of the phase difference is a delta function centered at the displacement, which in this case, is the point of registration (x, y). The phase correlation $Corr(x, y)$ is given as:

$$Corr(x, y) = \ \delta(x - \Delta x, y - \Delta y) \tag{11}$$

While phase correlation registration is mostly used to estimate translational shifts between images, it can, under certain limited conditions, also be used to estimate in-plane rotations and scales. If the frequency domain is presented in polar coordinates, then the rotation will be a shift on the axis corresponding to the angle. Therefore, a rotation angle can be derived by phase correlation based shift estimation in polar coordinates using the log-polar phase correlation method [141].

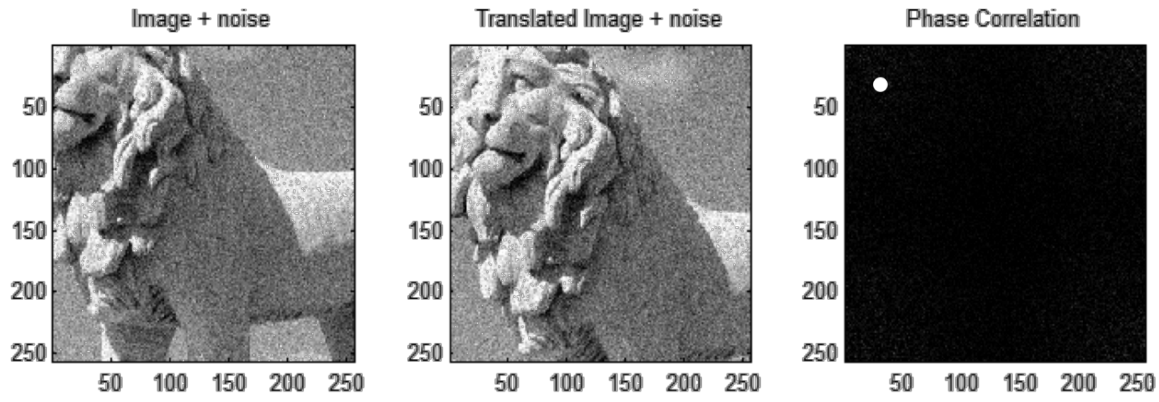

Figure 24 Phase correlation registration example showing the usage of phase correlation to determine relative translative movement between two images corrupted by independent Gaussian noise. The image was translated by (30,33) pixels. Accordingly, one can clearly see a peak in the phase-correlation representation at approximately (30,33). [142].

(b) Log-polar phase correlation

The log-polar transform is used for histological image registration due to its rotation invariant and scale invariant properties. The log-polar image geometry is used because of the fact that scaling and rotation in Cartesian domain corresponds to pure translation in log-polar domain. It is basically an extension of the phase correlation algorithm in polar coordinates.

The polar coordinates is defined as (ρ, θ) correspond to radial distance from the center and angle from the center respectively. Taking logarithm of radial distance ρ, we get log-polar coordinates. The log-polar transformation is a conformal mapping from the points on the Cartesian plane (x, y) to points in the log-polar plane $(log(\rho), \theta)$ [143].

Considering a polar coordinate system, where ρ is the radial distance from the center of the image say (x_C, y_c) and θ denotes the angle. Any point (x, y) can be represented in polar coordinates and it is given by:

$$(\rho, \theta) = \left(\sqrt{(x - x_c)^2 + (y - y_c)^2},\ \tan^{-1}\frac{(y - y_c)}{(x - x_c)}\right) \tag{12}$$

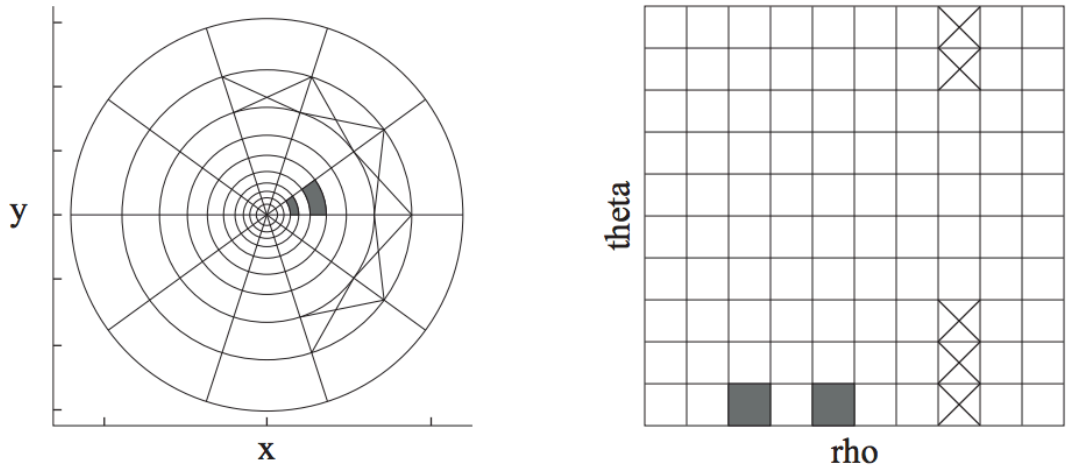

Figure 25 Approximate mapping from Cartesian space to (ρ, θ) space. The black box shows that the pixels are at a constant angle with respect to the center. The boxes with cross marks are at a constant radial distance from the center. [144]

In log-polar coordinates, logarithm of the radial axis is taken by:

$$(\rho, \theta) = (log(\rho), \theta) \tag{13}$$

Now if the image is scaled by a factor of say α, then the coordinates (x, y) in Cartesian domain will become $(\alpha x, \alpha y)$. Introduction of logarithms will simplify the procedure, the coordinates in log domain will be reflected as:

$$(log(\alpha x), log(\alpha y)) = ((log\alpha + logx), (log\alpha + logy)) \tag{14}$$

The equation 9 shows that scaling is represented as translation in log polar domain. The effects of distortions are expressed by log-polar image translation on ρ axis and θ axis, respectively in the log-polar coordinates. However, when the original image is translated by $(\Delta x, \Delta y)$, the corresponding log-polar coordinates is represented by:

$$\rho' = log\sqrt{(e^{\rho}\cos\theta - \Delta x)^2 + (e^{\rho}\sin\theta - \Delta y)^2} \tag{15}$$

$$\theta' = \tan^{-1}\frac{(e^{\rho}\sin\theta - \Delta y)}{(e^{\rho}\cos\theta - \Delta x)} \tag{16}$$

According to the above equations, the slight translation produces a modification of the log-polar image. Therefore, the log-polar image is not suitable for faithfully extracting translation parameters of images [145, 146, 147].

To overcome this limitation, the log-polar transform phase correlation algorithm first applies Fourier transform over the images and then applies the Log-Polar Transform (Figure 26) to the magnitude spectrum to recover scale and rotation by using phase correlation in log-polar space [143].

This is due to the fact that the magnitude spectrums of the image and its translated counterpart are same; only their phase spectrums are different.

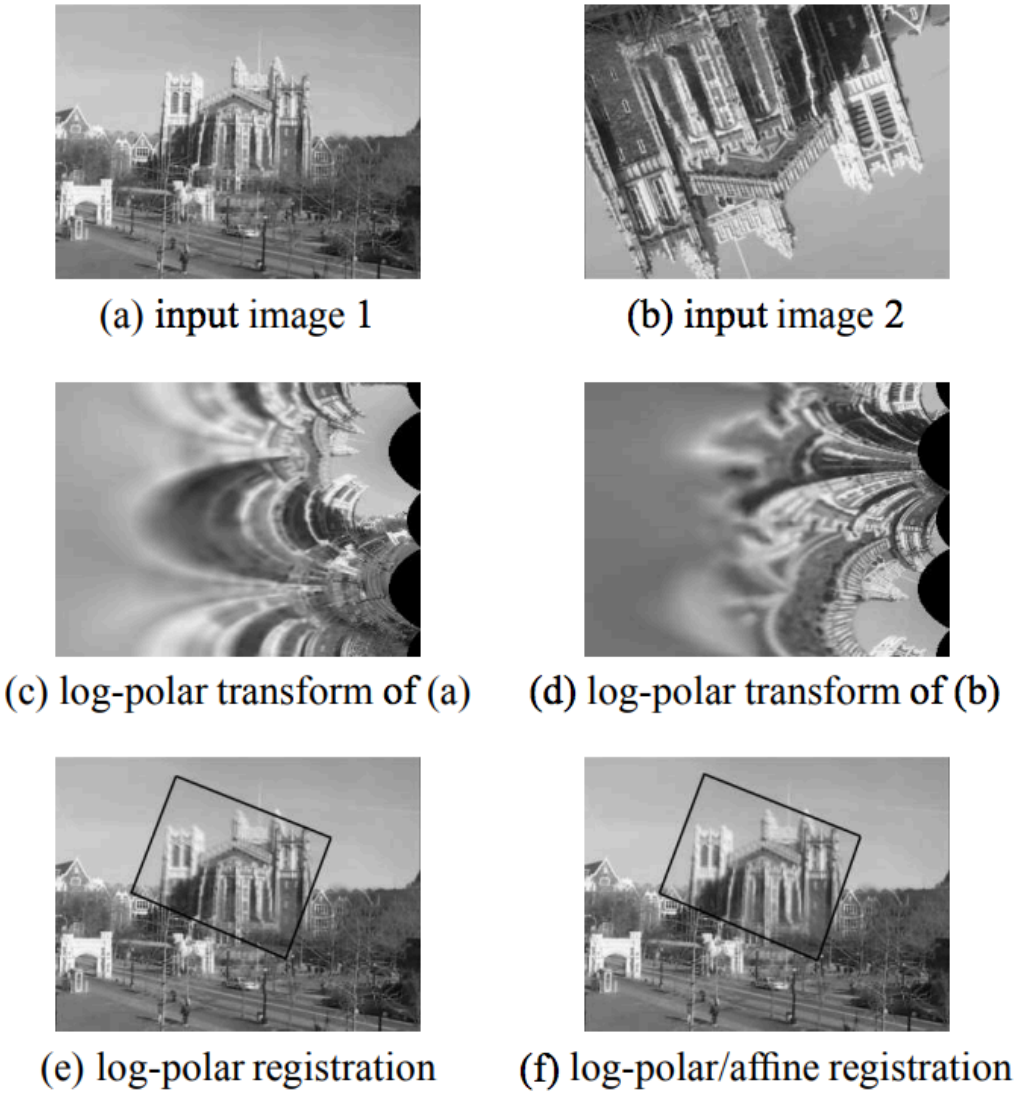

Figure 26 Log-polar phase correlation registration example showing translation and rotation recovery of image (b) by log-polar transform [148].(a) Reference image (b) Rotated image (c) log-polar transform of (a) (d) log-polar transform of (b). (e) log-polar registration of (a) (f) log-polar registration of (b).

2.4.3. Feature based methods

The feature based methods relies on the salient features of the images in order to achieve sub-pixel accuracy in image registration as opposed to the global alignment provided by rigid registration methods. The options ought to be distinct, unfold everywhere the image and with efficiency detectable in each picture.

Feature-based approaches attempt to find the correspondence and transformation using distinct anatomical features that are extracted from images. These features include points, edges, corners (regions in the image with large variation in intensity in all the directions) and contours of anatomical structures [149]. Feature-based methods are typically applied when the local structure information is more significant than the information carried out by the image intensity.

Feature based methods typically follow four fundamental steps(Figure 27), namely; feature detection and description, feature matching, transformation model estimation, image transformation and resampling [149].

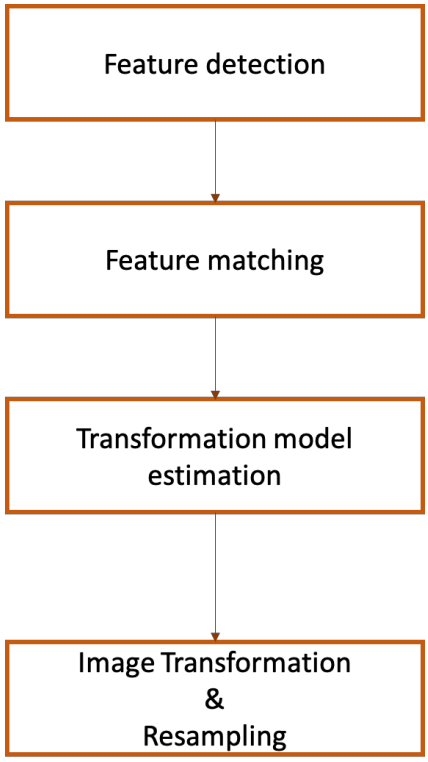

Figure 27 Fundamental steps of feature based image registration.

Feature detection and description: Any salient and distinctive objects or features like closed-boundary regions, edges, contours, line intersections, corners, etc. are detected using the various feature detectors. For further processing, these features can be represented by their point representatives center of gravity, line endings, distinctive points which are called control points (CPs) or with a vector called feature descriptor which describes the different parameters of the detected feature [150].

Feature Matching: In this step, the correspondence between the features detected in the sensed image and those detected in the reference image is established. Various feature descriptors and similarity measures are used for matching purpose.

Transformation model estimation: The type and parameters of the mapping functions, aligning the sensed image with the reference image, are estimated. The parameters of the mapping functions are computed using the established feature correspondence in the previous step. Depending on the intended transformation, affine or deformable transformation can be applied to map the source and reference image.

Image transformation and interpolation: The sensed image is transformed by means of the mapping functions. Image values in non-mapped coordinates are computed by the appropriate interpolation technique. The most generally used interpolation techniques are bilinear interpolation and nearest neighbor interpolation [4]

The accuracy of entire feature-based image registration methods are typically evaluated based on the parameters like localization error, matching error, alignment error and computational time required [150].

2.4.3.1. Feature detection methods

Below are some of the feature detection methods used for feature based histological image registration.

(a) Harris corner detection

Corners are regions in the image with large variation in intensity in all the directions. The Harris corner detector method was proposed to find whether a point shows significant change in all direction or not [151]. If yes, then point is marked as a corner point.

Harris corner detector $E(x, y)$, is based on the auto correlation function of the intensities. It basically finds the difference in intensity for a displacement of $(\Delta x, \Delta y)$ in all directions. This is expressed as below:

$$E(x,y) = \sum_{x,y} \underbrace{w(x,y)}_{window\ function} . \left[\underbrace{I(x+\Delta x, y+\Delta y)}_{shifted\ intensity} - \underbrace{I(x,y)}_{intensity} \right]^2 \quad (17)$$

The window function is either a rectangular window or Gaussian window which assigns weights to pixels underneath.

A Harris response function R (see appendix) is then computed to determine if the point (x, y) is a corner or not.
The Harris corner detector is invariant to translation, rotation and illumination change [152]. This detector is most repetitive and most informative. The disadvantage of this detector is it is not invariant to large scale change [153].

(b) Scale invariant feature transform (SIFT)

Scale invariance is an important factor in ensuring the reliability of extracted features in a series of 2D histological slices. It is important that the features extracted can be detectable even under changes in image scale, noise and illumination. The deformation of tissue slices after histological sectioning contributes to the change of scale of salient features in successive tissue slices.

The SIFT method is robust and invariant to scaling, orientation, illumination changes, and partially invariant to affine distortion. This is achieved by decomposing images into multiple resolutions and performing the registration from low resolutions to high resolutions, hierarchal registration speed, avoid local minima, and therefore improve registration performance [154].

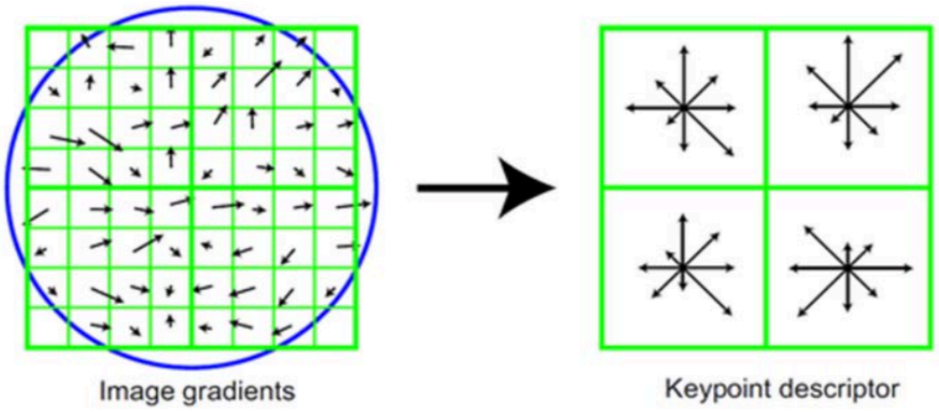

Figure 28 SIFT keypoint generation showing the four parameters of a SIFT keypoint: the key-point center coordinates x and y, its scale (the radius of the region), and its orientation (an angle expressed in radians) [155].

A SIFT key-point as shown in Figure 28 is an image region with an orientation. It is described by a geometric frame of four parameters: the key-point center coordinates x and y, its scale (the radius of the region), and its orientation (an angle expressed in radians) [155].

(c) Speeded up robust features (SURF)

SURF as the name implies, is a speeded-up version of SIFT. In SIFT, Lowe [156] approximated Laplacian of Gaussian (LoG) with Difference of Gaussian for finding scale-space. SURF goes a little further and approximates Laplacian of Gaussian with Box Filter [157].

SURF is based on multi-scale space theory and the feature detector is based on Hessian matrix and also rely on the determinant of Hessian matrix for both scale-space detection and key-point localization.

Since Hessian matrix has good performance and accuracy. In image $I(x, y)$ is the given point, the Hessian matrix $H(X, \sigma)$ in X at scale σ, it can be define as:

$$H(X, \sigma) = \begin{bmatrix} L_{xx}(X, \sigma) & L_{xy}(X, \sigma) \\ L_{yx}(X, \sigma) & L_{yy}(X, \sigma) \end{bmatrix} \quad (18)$$

Where $L_{xx}(X, \sigma)$ is the convolution result of the second order derivative of Gaussian filter with the image I in point X, and similarly for $L_{xy}(X, \sigma)$ and $L_{yy}(X, \sigma)$.

SURF creates a 'stack' without 2:1 down sampling for higher levels in the pyramid resulting in images of the same resolution. Due to the use of integral images, SURF filters the stack using a box

filter approximation of second–order Gaussian partial derivatives as shown in figure (2). Since integral images allow the computation of rectangular box filters in near constant time [158].

2.4.3.2. Feature matching

The problem of feature matching can be formulated as follows, suppose that p is a point detected by a feature detector in an image associated with a descriptor $\phi(p)$ of K dimension.

$$\phi(p) = \{\phi_k(P) | k = 1,2, \dots, K\} \quad (19)$$

where for all K, the feature vector provided by the k-th descriptor is

$$\phi_k(p) = (f_{1_p}^{k}, f_{2_p}^{k}, \dots, f_{n_{kp}}^{k}) \quad (20)$$

The aim is to find the best correspondence q in another image from the set of N interest points $Q = \{q_1, q_2, \dots, q_N\}$ by comparing the feature vector $\phi_k(p)$ with those of the points in the set Q. To this end, a distance measure between the two interest points descriptors $\phi_k(p)$ and $\phi_k(q)$ can be defined as

$$d_k(p, q) = |\phi_k(p) - \phi_k(q)| \quad (21)$$

A match between the pair of interest points (p, q) is accepted only if p is the best match for q in relation to all the other points in the first image and q is the best match for p in relation to all the other points in the second image.

In this context, it is very important to devise an efficient algorithm to perform this matching process as quickly as possible. The nearest-neighbor matching in the feature space of the image descriptors in Euclidean norm can be used for matching vector based features [159].

2.4.4. Non-rigid registration methods

A series of unregistered sequential histological slices can also be considered as a moving object in a visual scene caused by the relative motion between an observer and a scene. Image registration can thus be considered as an object motion estimate problem across frames in a visual scene.

The purpose of local motion estimation methods is to compute a motion field representing the displacement of points in consecutive images. This enhances sub-pixel accuracy in registration as it tracks the displacement of each point across the histological image stack.

This problem can be addressed using a variational formulation by modeling the problem as minimization of an energy function. Generally, the function is composed by a data term and a regularization term.

The data term is usually based on the conservation of some property during motion. A common data term is based on the brightness constancy assumption, which assumes that the object illumination does not change along its motion trajectory.

The regularization term allows to define the structure of the motion field and ensures that the optical flow computation is well posed and this can be seen as 'a priori' term [160].

Optical flow method

The notion of optical flow literally refers to the displacements of intensity patterns. This definition originates from a physiological description of the visual perception of the world through image formation on the retina.

In that sense, while optical flow is necessarily caused by relative motion between the observer and the objects of the observed scene, it only represents motion of intensities in the image plane, and not necessarily accounts for the actual 3D motion in the physical scene [161].

Computation of optical flow means computation of two vectors U and V. Vector U represents horizontal velocity of motion and V represents vertical velocity of motion. Usually U and V are computed using the concepts of energy functional. And the main aim is to minimize this energy functional. Energy functional consists of two terms: data term and smoothness term [162].

To determine optical flow, there is need to track some properties of images. Two key problems in optical flow estimation are: 1) Determine what image property to track 2) Determine how to track it [162]. Some features of the images are assumed to stay constant among multiple frames during optical flow estimation.

The most common assumption used in optical flow estimation is the brightness constancy assumption. It states that the gray value of corresponding pixels in the two consecutive frames should be the same.

Assume $I(x, y, t)$ is the center pixel in a n×n neighbourhood and moves by Δx, Δy in time Δt to $I(x + \Delta x, y + \Delta y, t + \Delta t)$. Since $I(x, y, t)$ and $I(x + \Delta x, y + \Delta y, t + \Delta t)$ are the images of the same point (and therefore the same) we have:

$$I(x, y, t) = I(x + \Delta x, y + \Delta y, t + \Delta t) \tag{22}$$

The choice of registration approach depends on the domain and scale of deformity in the set of histological images. The table below illustrates some deformation and the appropriate registration technique.

	Rigid/Affine	Feature Based	Non-rigid
Global rotation/translation	✔	—	—
Sub-tissue rotation/translation	—	✔	—
Global shrinkage/expansion	✔	✔	✔
Sub-tissue shrinkage/expansion	—	✔	✔
Tears/missing parts	—	—	✔

Table 5 Comparison of different registration techniques for histological images and their respective suitability for different kind of tissue aberrations.

2.5. 3D histology reconstruction techniques

3D histology reconstruction methods aim to restore the loss of continuity due to volume slicing of tissues. They are based on the assumption that the shape of a biological specimen changes smoothly across sections, but suffers from the various artefacts that affect every section independently during preparation.

While using 2D histological serial sections alone enables the reconstruction and representations of structures and their environment in 3D, which helps with subsequent segmentation and classification tasks [163], however, the original shape is unattainable without prior or external knowledge.

The basic foundation of all reconstruction methods is image registration. Image registration consists of optimizing the spatial alignment of variously oriented 2D slices relative to each other, while being robust to artefacts following histological preparation.

The most straightforward path to achieve 3D reconstruction of a series of 2D histological images is to register every slice with its direct neighbor and repeat the process with the following pairs. This is done by choosing a reference point to start from.

This reference point is an arbitrary slice usually the first slice or the middle slice in the series. In this approach, reconstruction is achieved by stacking of the transformations between all pairs of adjacent sections.

However, without any information about the original shape, volume reconstruction remains an ill-posed problem i.e. there exists a solution, it is not unique and there is no mechanism of validation because the true shape is unknown; for example, changing the initial arrangement of slices relative to one another will lead to a different reconstruction.

Thus, there is a need for a ground truth reference to regulate and validate the process of registration. The combination of non-invasive imaging with histology to relate macroscopic information to the underlying microscopic properties of tissues through the establishment of spatial correspondences in a multimodal framework has been studied for 3D reconstruction of the true shape of tissues and tissue substructures.

The multimodal framework for 3D reconstruction of serial histological sections can be grouped into three different approaches:

This include slice based approach which considers each slice as an individual object, volume based approach which considers the set of serial sections as a whole volume and a hybrid approach [113].

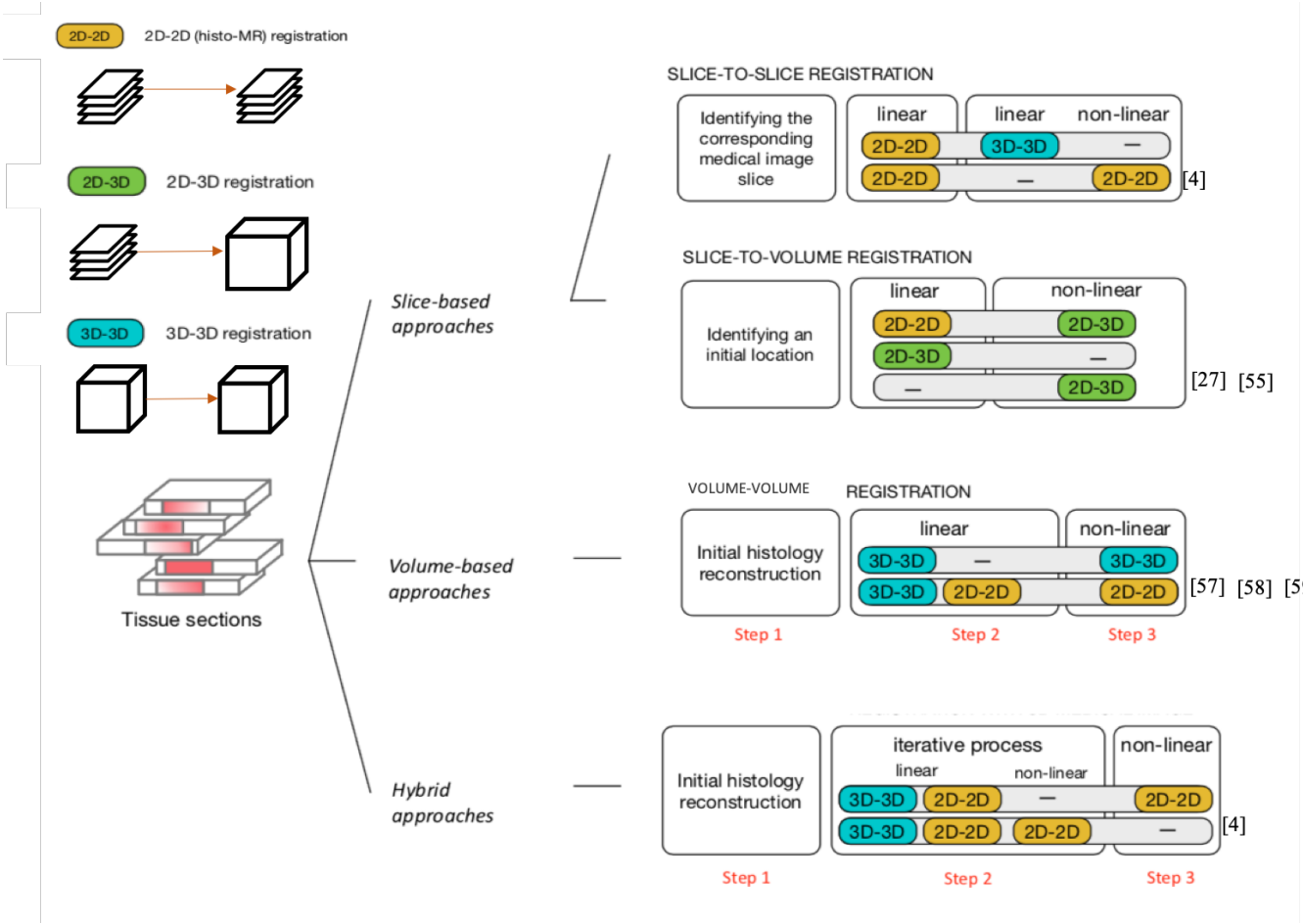

Figure 29 Strategies to register histology with volumetric medical imaging (ex or in vivo alone). The three main approaches (slice-based, volume-based and iterative) are presented. (*) In cases where ex vivo imaging is used as an intermediate modality, correspondences between ex vivo and histology are achieved through steps 2 and 3, and the mapping between histology and in vivo is completed via registration between ex and in vivo scans (extra step) [113].

2.5.1. Slice-to-slice registration (2D-2D)

In this approach, every histological slice is considered as an individual object. This approach is generally preferred in cases where the histological dataset is too sparse or has too few slices. It consists of the use of 2D histological serial section dataset and a 2D reference dataset obtained from other modalities such as MRI or standard anatomical atlas.

The methods used in this approach assume that the cutting planes of histological slices and the acquisition planes of the reference set are parallel and that there always exists a histological section that has a counterpart in the set of MR slices. The problem therefore simplifies to a 2D-2D registration between every histological slice and its corresponding slice in the reference dataset [113].

2.5.2. Slice-to-volume registration (2D-3D)

This approach extends the slice-to-slice approach by acknowledging that there is no certainty that the cutting plane of histological slices is parallel to the acquisition plane of the reference dataset. Likewise, there is no guarantee that the histological slices are parallel to each other. This implies that structures belonging to a tissue slice may extend over several slices in the reference dataset.

This in turn suggests that the corresponding 3D reference slice can only be discovered through a slice-to-volume (2D-3D) registration. In 2D-3D volume registration, 3D point cloud is generated by detecting key features, matching points or intensities between a 2D histological slice and slices of a 3D reference volume. This is done by mapping the 2D histological slice to the 3D plane of the reference dataset [164, 136].

2.5.3. Volume-to-volume registration (3D-3D)

The main drawback of slice-based approaches is their sensitivity to initialisation, the choice of the initial reference point affects the cost function and thus the convergence of the registration procedure. Other challenges involve the cost function selection and the optimisation strategy [165]. As a result, the performance of slice-to-volume registration shows greater dependence on the input images than 3D-3D registration [165]. Considering histological sections all together *i.e.*, the histological dataset as a whole, allows overcoming such an issue.
Volume-based approaches typically follow a sequential procedure. Firstly, a volume is reconstructed from the set of histological slices by serial pairwise linear registrations [166, 167] or simple stacking by alignment of tissue slices [168]. This is followed by a coarse, linear alignment of the geometries of both reference image volume and histological volumes, which may then be refined by non-linear registration.

2.5.4. Hybrid approach

The hybrid approach is similar to volume based approach except that both the serial arrangement of the histology stack (reconstructed volume) and its alignment relative to the reference image volume are jointly refined.

A 3D-3D registration, which updates the global alignment between the current estimate of the histological volume and the reference image volume is implemented alongside 2D-2D registrations, which affect the serial arrangement of slices relative to each other by aligning them with their current corresponding slice in the reference image volume used. This in turn provides a new histological volume which is used at the next iteration. This process is repeated until convergence.

2.6. Assessment techniques for 3D histology reconstruction

The validation of the accuracy and precision of 3D histology reconstruction is an ill-posed problem or impossible without the use of a reference model for comparison. Validation techniques seek to identify neuroanatomical structures that are recognizable after registration in the reconstructed 3D volume [113].
Below are some of the methods that have been used for the validation of 3D reconstruction of histological slices.

2.6.1. Visual Assessment.

Visual assessment is an intuitive way of validating the reconstruction accuracy but must be carried out by experts and does not provide with any quantitative measure. Visual assessment is very practical when comparing one method of reconstruction against others [169, 170]. This can generally be done without the help of a reference 3D volume.

In the case of histology reconstruction without the help of 3D reference volume, the criteria used to tell whether the reconstruction is successful include visually improved representations of small structures (subcortical nuclei, cortical areas) and smooth inner and outer borders [171].

When a 3D reference volume is available, visual assessment can be performed by cross-section comparison [166, 172] of the two volumes displayed in the same geometry or by superposition of adjacent sections [117, 120] in order to check for disparities.

2.6.2. Landmark-based validation

This is the most widespread method [113] used for validation of 3D histological reconstruction. It consists of the automatic or manual extraction of corresponding anatomical landmarks or key features in the reconstructed volume and the reference volume [115, 165]. This is followed by the computation of the Euclidean norm between the corresponding landmark points extracted in the two images. This is also referred to as target registration error (TRE) [168, 173].

2.6.3. Measures of Image co-registration.

Measures of image co-registration rely on regions of interest(ROIs) manually delineated by an expert in the registered histological 2D sections and the reference image. The Dice score or the Jaccard index are two measures that can be computed to quantify the amount of overlap between the two regions [117, 174, 175]. The Dice score was shown to be a reliable indicator of registration accuracy only for small and localized ROIs in several locations in the image space [176].

2.6.4. Texture-based methods.

Grey-level co-occurrence matrices(GLCM) [177] have been used to assess the quality of the histology reconstruction [178]. Such matrices were computed by calculating how often the pair made of a pixel of interest with a certain intensity and its immediate neighbour in the direction orthogonal to the cutting plane occurs in order to quantify the smoothness of the reconstruction [113].

CHAPTER 3: From IR spectra to registrable metadata images for 3D pathology

In this chapter, we propose a standard processing sequence or methodology for 3D chemical imaging of tissues by IR microscopy. The methodology combines the methods and approaches that have been discussed in Chapter 1 and 2 for IR spectra data treatment and 3D reconstruction of tissue samples.

It has been demonstrated that IR spectrum matrix can be reconstructed in 3D by stacking of serial tissue sections [26]. Our proposed methodology is aimed at standardizing the protocols that have been used experimentally for chemical imaging by IR microscopy as well as define a standard routine that can be used clinically by pathologists for 3D chemical imaging of brain tumours.

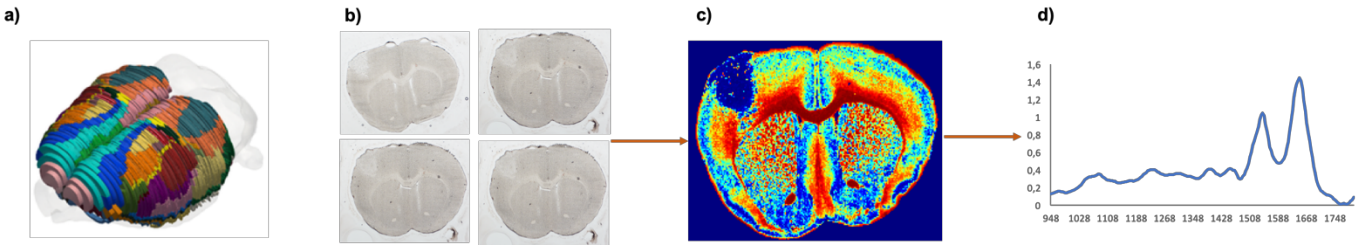

Figure 30From IR spectra to registrable metadata images for 3D pathology. (a) 3D reconstructed volume of the mouse brain. (b)Visible image of histological slices from mouse brain. (c) 2D IR mapping of spectral derived information. (d) 1D spectrum extracted from 2D IR map in (c).

3.1. Introduction

3D histology is a powerful approach for microscopic imaging biological specimens and is the next frontier for modern histopathology. They provide a 3D visualization of structures of the internal topography of a specimen which are invisible at macroscopic scale and are of diagnostic value.

Although, clinical imaging techniques such as MRI and CT offer 3D visualization of organs, which can also depict anatomical features that are of diagnostic value, however, in smaller biosystems, such as cells, tissues, or small-animal organs, these techniques are limited by their sensitivity (MRI cannot go below 100-µm in small animals). Thus, there is a lack of reliable clinical standard 3D imaging solutions at the microscopic scale for use in biological analysis [111].

Conventional histological methods such as fluorescence-based confocal imaging have been demonstrated to perform 3D analyses on small biosamples, mostly cells and small tissue blocks, but their penetration depth is limited and the use of labels restricts the analytical value of the 3D images [179].

This is a major frontier in biological research, where supervised techniques depending on labels or contrast agents can no longer satisfy the discovery appetite for biospecimens. Better-quality images of biosamples, at higher resolution, with higher contrast, and providing larger quantities of information, makes the addition of global chemical information more important. This is particularly true when several (or a multitude of) chemical compounds of tissues need to be revealed by histology [28].

While spectro-microscopies cannot rival fluorescence-based imaging techniques in terms of resolution and penetration depth. However, in terms of sample area scanned per unit of time (in minutes), IR and MS match the performance of multiphoton microscopy at appropriate resolutions.

Thus, with appropriate 3D reconstruction methods, a 3D view can be achieved; the advantage of spectro-microscopies stems from their ability to provide many different chemical data compared with the two or three labels possible with multiphoton microscopy.

Finally, the main advantages of spectro-microscopies are that they can provide extensive, if not global, quantitative chemical information about the sample without a priori supervision (compared with label-related histology).

Mass spectrometry (MS) imaging was the first spectroscopic technique that was proved to provide a 3D reconstruction of the chemical information of a tissue block [180]. In principle, mass spectra can provide thousands of signals recorded from each voxel of a 3D MS image.

A wide variety of molecules can be imaged in this way, including proteins, peptides, lipids, and endogenous and exogenous metabolites, although they cannot be imaged all together. Thus, no global chemical information can be obtained from the sample (including proteins, lipids and sugars).

IR microscopy on the other hand provides global chemical information of tissue samples. This implies that all chemical bonds present in the sample will raise absorption bands, notably for proteins and lipids, which exhibit intense absorptions, but also with major contribution from carbohydrates and nucleic acids to the final spectral information.

Also, because it is quantitative, it also allows mapping potentially a wide range of chemical information in a non-supervised pattern, which is undoubtedly a major advantage for comparison between healthy and pathological tissue specimens without any a priori knowledge about the sample.

However, IR microscopy has been limited due to its relatively high spatial resolution compared to a technique like Raman spectroscopy which offers spatial resolution of <1-µm, relatively lower molecular details compared to a highly sensitive technique like MSI, the bottlenecks of using cooled IR detectors, long acquisition time for large tissue and the interpretation of spectra data

IR microscopy is now ready for development of 3D histology due to the development of QCL microscopes; which means data acquisition can be done over a long period of time for large samples [27]. Thus, with appropriate data treatment methods and 3D reconstruction techniques, 3D quantitative chemical imaging of tissue samples can be achieved by IR microscopy.

However, in order to introduce IR microscopy as a diagnostic tool for pathology, there is a need to develop standard routines for chemical imaging by IR microscopy. Several experimental methods [181, 65, 54, 53, 55, 24] have been proposed for IR data treatment and to the best of my knowledge no method have been processed for 3D reconstruction of IR chemical images.

In this chapter, we introduce a processing sequence for 3D-IR microscopy. I propose a routine based on standard experimental techniques for IR data treatments and techniques that have been used for 3D reconstruction of histological images. I evaluate and extend the different methods for a routine application to 3D chemical imaging of tissues by IR microscopy.

Our proposed processing sequence comprises of five major sequential phases which spans from sample preparation to 3D reconstruction of tissue slices. These phases include; 1- sample preparation, 2- data acquisition, 3- IR data treatment, 4- metadata extraction and 5- 3D reconstruction.

Figure 31 3D chemical imaging by IR microscopy processing sequence.

The sample preparation phase consists of the histology protocols used for preparing tissue samples for IR imaging.

The data acquisition phase consists of setup and protocols necessary for 3D chemical imaging by IR microscopy. The major feature of this phase is the setup of a high-performance computing environment for analysis and a data storage server.

The data treatment step consists of routine computational methods that are implemented for quantitative analysis of the IR spectrum matrix. I define the basic mathematical operations required in order to aid interpretation of the 3D spectrum matrix of brain tissue samples. This is followed by the metadata production phase. This phase is the interpretation stage where specific chemical information is extracted to be mapped into derived 2D IR images from the IR spectrum matrix.

The 3D reconstruction phase is the final step of our proposed methodology. In this phase we propose a new 3D hierarchical image registration method for 3D reconstruction of derived IR images. In this phase we use of image registration techniques to partition and realign the derived 2D IR images for 3D reconstruction of tissue slices.

3.2. Sample preparation

In order to obtain the 3D spectrum matrix of brain tissues, there are basic histological steps that precede the acquisition of tissue samples using an IR microscope. These sample preparation methods are conventional methods used in histology with the exception of preparing the sample for dying or immunohistochemistry.

For IR microscopy sample preparation, the following steps are followed:

1. Sample extraction from micro environment. Could be a tissue sample from biopsy in clinical application or an organ extracted from an animal.
2. Embed the sample in optimal cutting temperature (OCT) compound.
3. For analysis of healthy tissues, the instant freezing of the sample using Isopentane (2-methylbutane) cooled at -80℃ (liquid N_2) to guarantee that the degradation in cell and tissue contents as a result of being taken out of the microenvironment is limited.
4. Otherwise, the sample is cooled at -80℃ (liquid N_2) without Isopentane for pathological tissues where cracks in tissue structures might not be of great importance in tissue analysis.
5. Continuous cryo-microtomy where the tissue sample is sectioned within the range of 4-20µm thickness.
6. Fix sectioned tissues on a 2mm thick CaF_2 window for acquisition.

The 4-20µm section thickness range is specified because 20-µm represents the thickness limit for imaging at cellular resolution. In addition, for example at 20-µm a mouse brain leads to 300-400 sections while at 4-µm, it is 5 times more, which consequently makes obtaining good shaped tissues difficult as wells elongating the time for total image acquisitions.

Also, 4-µm also raises the issue of SNR and thus IR spectra data treatments will be compromised at this resolution. It represents the diffraction limit of IR radiation.

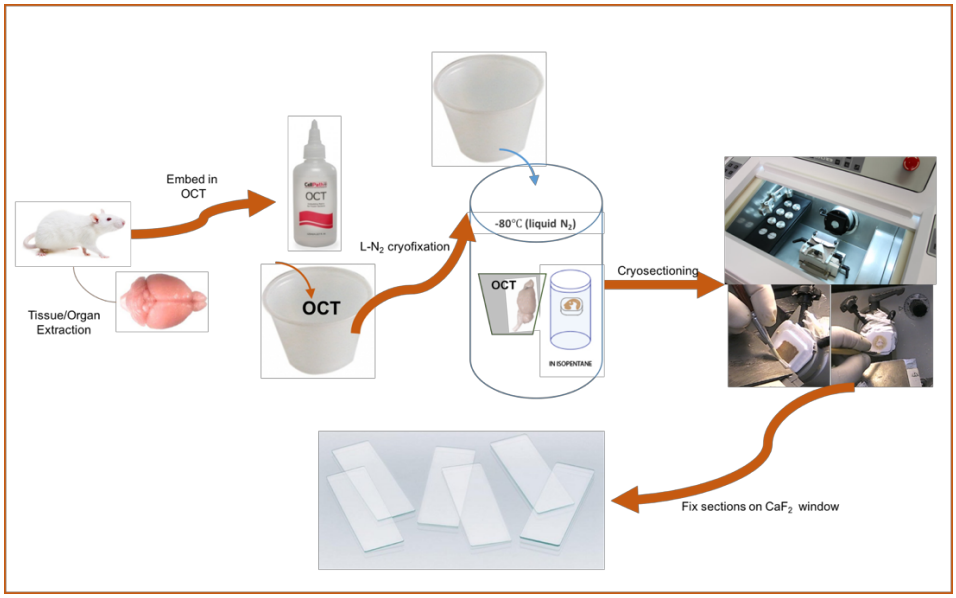

Figure 32 IR microscopy sample preparation process.

3.3. Data acquisition

To perform data acquisition of a prepared sample, the sample is mounted on the sample stage of the IR microscope. Typically, IR microscopes comes with a proprietary software to simplify the data acquisition process. On the software, the area of interest in the sample is defined, the range of wavenumbers to probe is also defined. A repository to store the data is defined and the acquisition is launched. The duration of the acquisition depends on different factors such as the type of IR microscope, spectral resolution, pixel size and the size of the sample.

I propose a setup for reliable and replicable IR data acquisition. This setup consists of the instrument, data repository and analytical node. In order to ensure proper data management. we propose the use of this high-performance computing setup and data storage for IR samples. This is important as the separation of concerns allows a fault tolerant system that can be easily traced for errors.

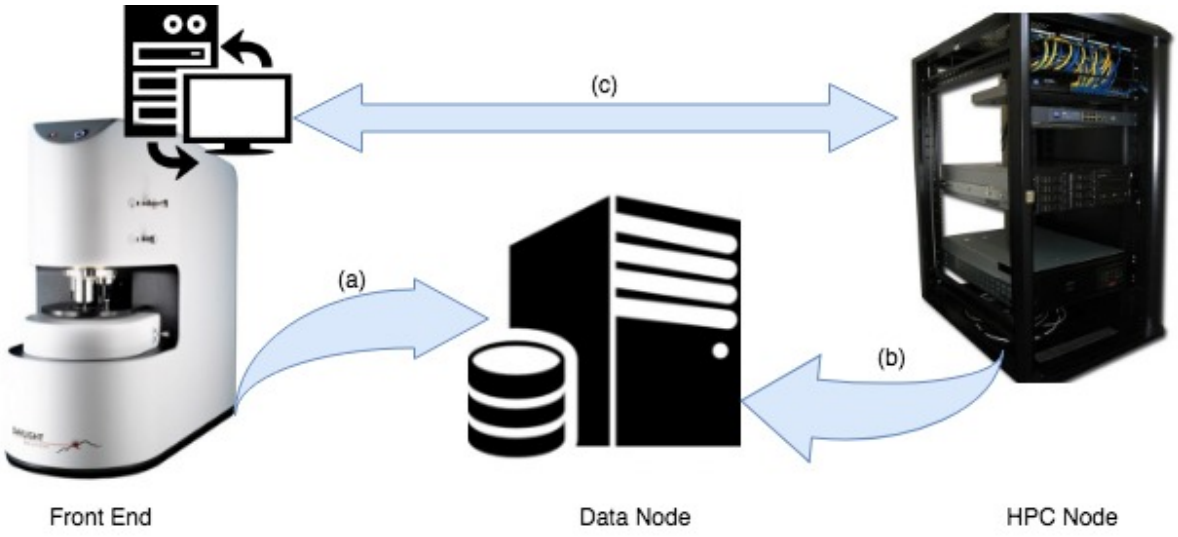

Figure 33 Data acquisition setup for 3D IR microscopy

In the figure above, the 3-tier architecture proposed enables the separation of the point of 1- data acquisition, 2- storage and processing node in order to achieve a secure and fault tolerant system for 3- IR data processing. It is a major requirement to separate the data storage node and the processing node from the point of acquisition because the processing of IR data is computationally intensive and the data size is huge depending on the size of the tissue.

Similarly, performing computation on this huge data requires huge computational capacity. For example, given the problem of spectra decomposition, a 32-cores CPU would require approximately ½ day to compute IR-band decomposition of one tile (230,400 spectra) of the sample tissue. Hence, this big data also requires a high performance computing node for high-throughput computation.

In Figure 33, the architecture also defines a secure pathway for data collection and information retrieval. There is no direct access to retrieve data from the storage server. This ensures that the IR data is secured and can only be modified through access to the data storage server. The computations and information retrieval is processed on the HPC node which provides a fast access to relevant information.

3.4. IR data treatment

Raw IR spectra like other measurements derived from analytical instruments, typically consist of chemical information, baseline and random noises [182]. These random noises and different baselines contribute to varying intensities across tissue samples and make quantitative spectral information incomparable.

IR data treatment methods are used to correct raw IR spectra for baseline distortions, irregular intensities in order to make IR spectra ready for quantitative analysis. Data treatments can also enhance qualitative spectral information in terms of visualization due to the correction of irregular intensities arising from distorted baselines.

In this section, we propose a routine data treatment process for correcting raw IR spectra. These includes an automated baseline correction method and a method to remove histological artefacts by analyzing spectra data.

3.4.1. Automated Baseline Correction

Raw IR spectra must be corrected for enhancing the quantitative aspect of spectral information and make them comparable through baseline correction. Typically, the corrections of baseline offset or distortions are performed to avoid further artifacts in spectral data treatments. Sub-routines must be applied to all spectra with the same thresholds, intensity levels... etc. to avoid quantitative change between spectra [26].

Several baseline corrections exist in the literature and have been applied for IR spectra baseline correction [97, 183]. However, these techniques are manual, thus not practical for use over large dataset with hundreds of tissue sections.
Thus, we propose a simple automated baseline correction procedure defined by Bobroff et al [26] for large dataset of tissue sections. To automate the correction of baseline, we apply the following procedure:

1. For FTIR systems, the correction of ambient absorption (CO2 and water vapor) by the removal of the 2400- 2300 cm^{-1} ($\nu(CO_2)$) band.
2. Iterate through the spectrum to determine the lowest absorbance value
3. Apply an offset of baseline inducing negative absorption values are corrected so that the whole spectrum curve is raised by the lowest absorbance value;

4. Alternatively, correct baseline by applying an offset with the lowest absorbance value set to zero.

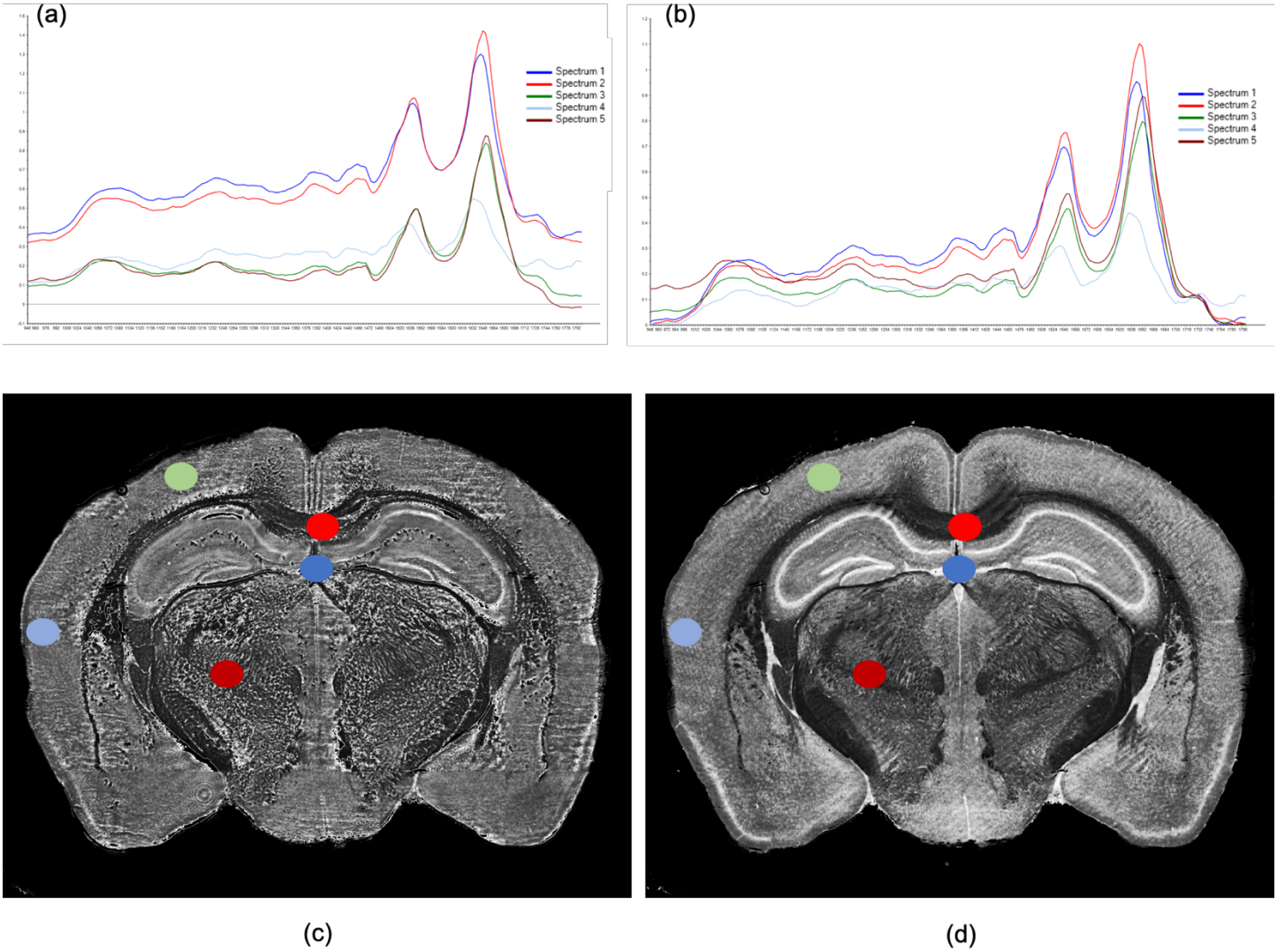

Figure 34 Baseline correction for enhancing quantitative and qualitative spectral information. (a) Example of spectrum taken from different regions of a pathological mouse brain tissue showing quantitatively incomparable baselines for each anatomical region. (b) Automated baseline correction showing corrected baseline by rasing the whole spectrum curve with the lowest absorption value. (c) IR image before baseline correction. (d) IR image after baseline correction.

3.4.2. Automated Spectra Cleaning

Spectra cleaning is a process used in the removal of artefacts such as holes and glues that arise from histological sample preparation (Figure 35). While this can also be achieved on spectra derived images of tissue slices to enhance visualization by using image processing techniques such as thresholding and segmentation, cleaning at spectra data level offers two significant advantages.

It enhances the speed of computation on spectra data because of the removal of spectra that arises from artefacts. It also enhances comparative analysis between spectra due to the elimination of irregular spectra that arise from artefacts, thus eliminating baselines associated with these spectra.

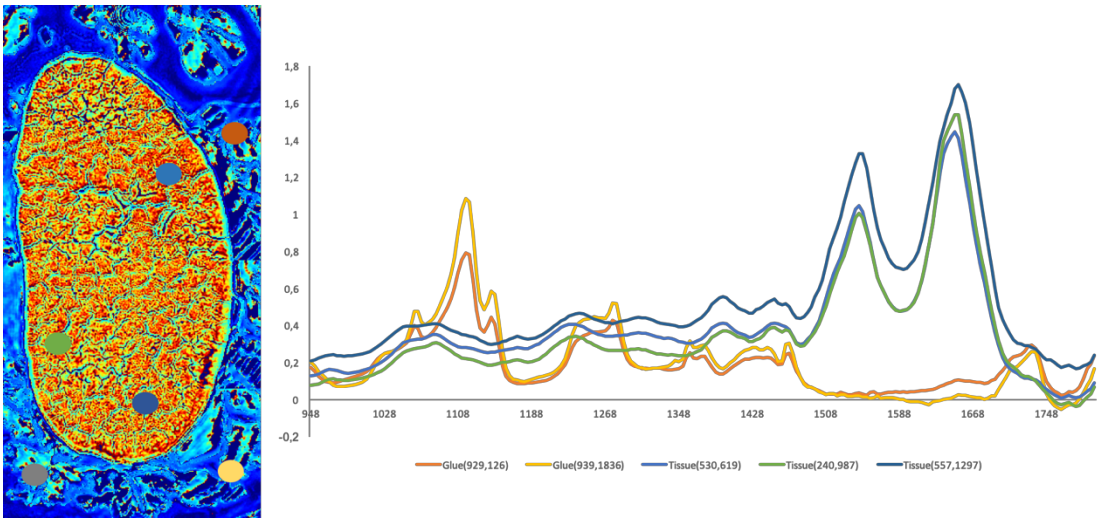

Figure 35 Untreated mouse kidney sample tissue spectra showing spectrum corresponding to surrounding glue and tissue. The spectra corresponding to glue shows irregular absorption pattern and baselines.

The aim of an automated IR spectra cleaning algorithm is to define a function $f(s)$ which compares the IR spectra in a 3D spectrum matrix and returns a modified 3D spectrum matrix where irregular IR spectra are nulled.

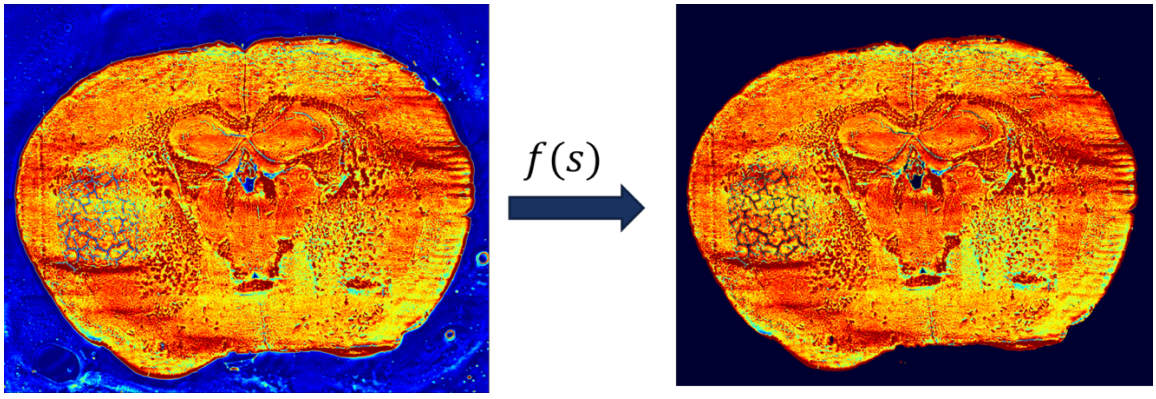

Figure 36 Spectra cleaning algorithm result showing the removal of surrounding glue from the spectrum matrix.

This generally requires an iteration strategy, metric of comparison and a threshold to validate a spectrum. There are several methods that can be employed to achieve this depending on the complexity of artefacts on the tissue sample.

(i) Unsupervised Clustering

The automated spectra masking function $f(s)$ could be defined as an unsupervised clustering task, where the set of s spectra is grouped into k clusters.

$$f(s) = \min_{s} \sum_{i=1}^{k} \sum_{x \in S_i} \|x - \mu_i\|^2$$

μ_i represents a feature vector whose class is either an artefact, slide background, a tissue region or myelinated tissue structure.

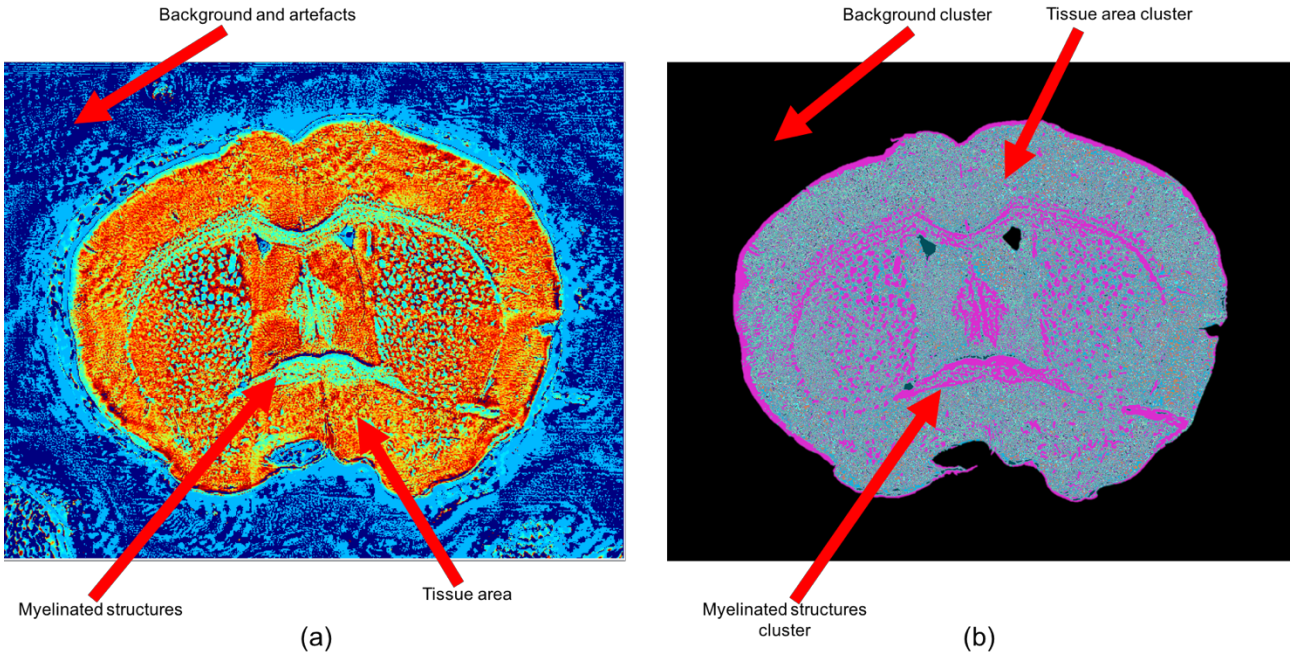

Figure 37 Spectra cleaning by segmentation. (a) A sample mouse brain tissue showing different components of the spectra matrix differentiated by colour. (b) Segmentation result creating 3 clusters, of slide background, tissue area and myelinated structures.

(ii) Principal Component Analysis

The automated spectra masking function $f(s)$ could also be defined as a task of retrieving orthogonal components of the 3D spectrum matrix. The data could be subjected to Principal Component Analysis (PCA) to obtain more detailed information about sources of variance in the 3D spectrum matrix. Typically, the first principal component is expected to contain only tissue related spectra (unless more than 50% of the IR image is occupied by glue, then the 1st PC will be related to it), thereby eliminating the artefacts.

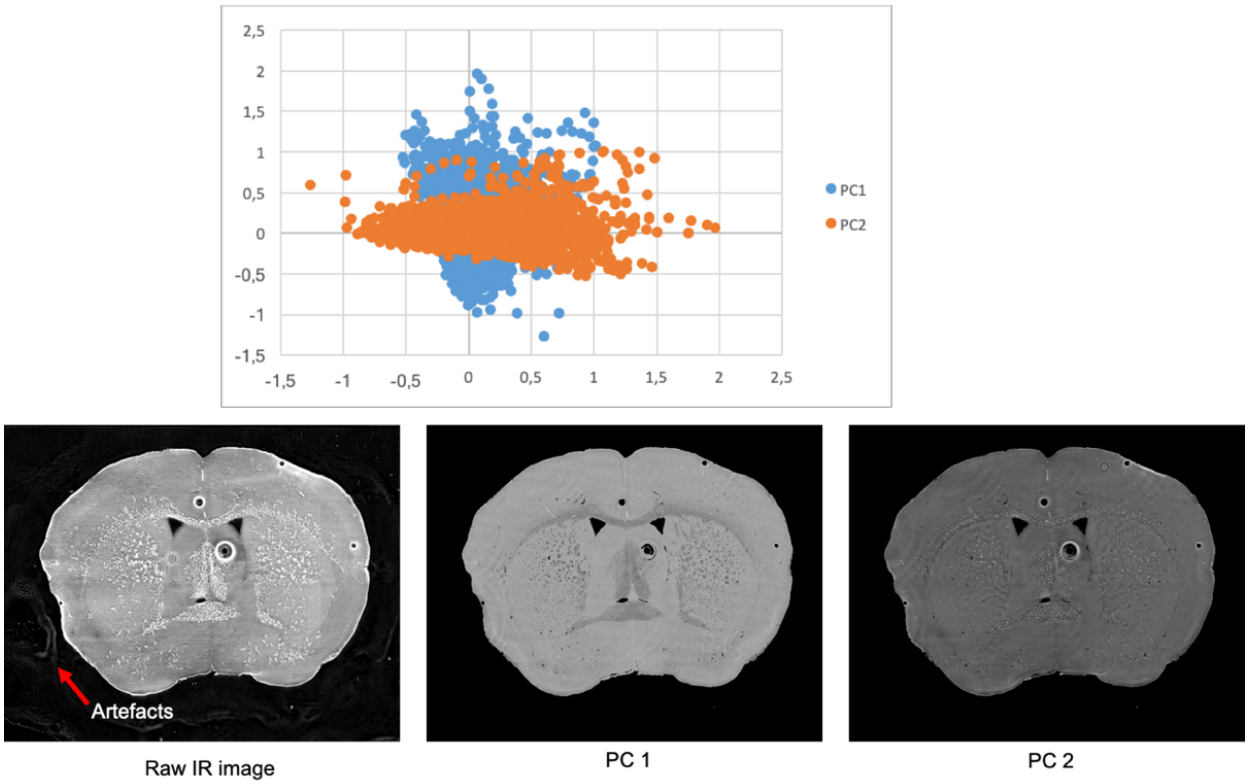

Figure 38 Spectra cleaning by principal component analysis of a sample brain tissue. The 1st and 2nd principal component contains tissue related spectra only, thereby elimenating the artefacts present in the tissue slice

(iii) Peak Ratio (Supervised Cleaning)

Supervised masking as the name implies this method is derived after an experiment on the spectrum of different types of artefacts. The ratio of the ν(P-O-C) stretch peak (1088 cm^{-1}) and Amide I peak (1652cm^{-1}) can be used to remove regular artefacts that arise from glues surrounding the tissue.

This is a fast alternative to unsupervised clustering and PCA as it does not require multiple iteration (unless the 1088 cm-1 peak is low due to weak absorption of glue or contribution from tissue molecular contents).

Typically, the Amide I peak is absent in tissues, this is used as the threshold to filter out the spectra corresponding to artefacts.

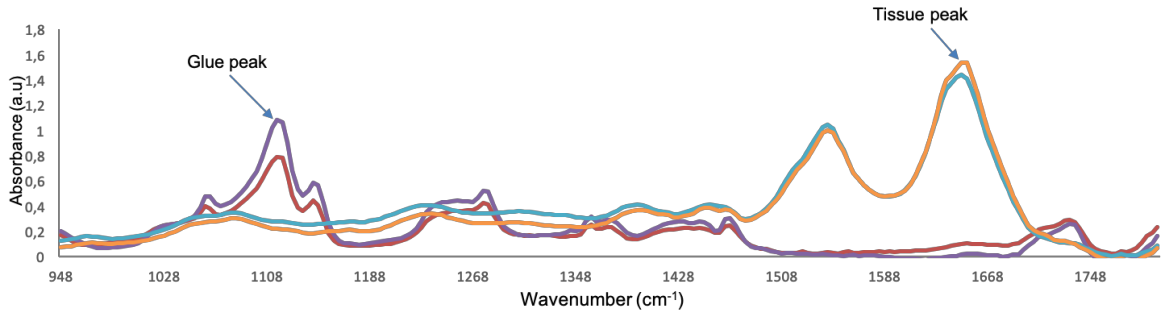

Figure 39 Spectra collected from glue samples. Showing the 1088 cm^{-1} peak and the absence of the Amide I peak.

The table below shows a simple performance comparison of the above listed techniques for automated spectra cleaning.

Method	Speed	Accuracy	Tissue Size
Clustering (2 classes)	Moderate	High	Medium
PCA (2 principal components)	Slow	Very High	Small
Peak ratio	Fast	Normal	Large

Table 6 Performance comparison of spectra cleaning techniques using a mouse brain sample of 591,667,200 spectra..

3.5. Metadata extraction from IR spectra

The metadata extraction phase involves the manipulation of quantitative spectral information to extract specific biological markers from tissue sample. Metadata can be extracted directly from treated raw spectra or from advanced spectral data processing technique like band deconvolution or curve fitting [26, 24, 184, 185, 2].

The task of extracting all possible metadata from IR spectra is too large and out of the focus of this thesis. In this section, we focus on two major metadata for brain pathology application that can be extracted directly from treated raw IR data. These are the anatomical regions of the brain and the metabolic aberrations of a tumor.

We propose the use of standard spectral data treatments (integration of absorptions bands on raw spectra, peak-picking on secondary derivative spectra, etc.) to reveal the anatomy of the brain based on chemical contents variations between regions. Importantly, we could also calibrate several metabolic concentrations (glucose, glycogen, lactic-acid) in tissue samples using this approach [186].

3.5.1. Anatomy

The anatomy of tissues can be extracted from IR spectrum matrix based on the chemical profile of different anatomical structures. For example, for brain histology applications, the anatomy of brain tissues can be extracted by exploiting the global chemical profile of the brain.

The brain is a lipid-rich organ. The white matter of the brain contains well-defined long myelinated fiber tracts. On the other, the gray matter houses numerous neuronal cell bodies which are rich in different proteins for neurotransmission, among other purposes. Thus, exploiting the lipid and protein information for IR spectra can lead to distinguishing different anatomical features in the gray and white matter.

The protein information can be extracted by computing the spatial distribution of protein using the numerical integration of the band region $\int_{1480}^{1708}$ while the lipid information can be extracted by computing the spatial distribution of lipids from the integration of the $\int_{1360}^{1432}$, $\int_{1720}^{1752}$ and $\int_{2800}^{3020}$ (for FTIR systems) bands. To further distinguish between the gray and white matter anatomical structures, the ratio of the integration of the protein band and lipid band can be taken($\int_{1480}^{1708}$ / $\int_{1360}^{1432}$).

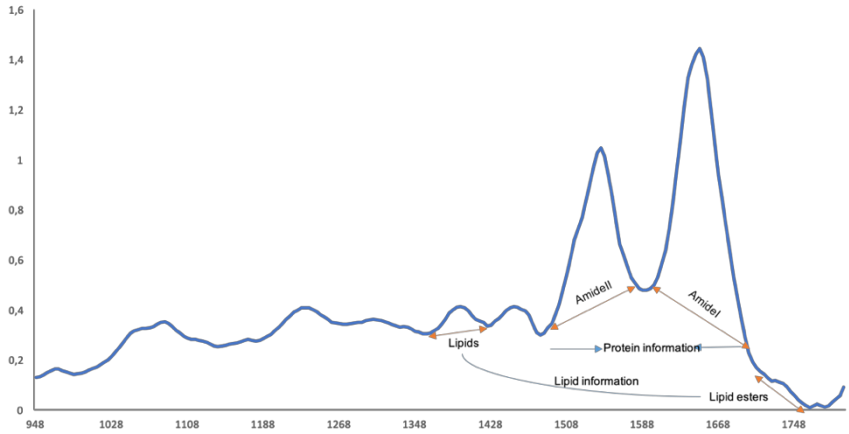

Figure 40 Mouse brain tissue sample using lipid and protein information from spectra to highlight different regions in the slice.

3.5.2. Metabolism

Metabolism is broadly defined as the sum of biochemical processes in living organisms that either produce or consume energy [187]. Metabolic alterations are a hallmark of an ischemic or hypoxic condition of brain, which occurs during stroke, cancer growth and generally in neuro-degenerative disease.

Conventional histology at best offers a semi-quantitative histochemical glycogen analysis without information about glucose and lactate. Thus, IR microscopy offers a unique advantage in the area of metabolic analysis due to the ability to resolve glycogen, glucose and lactate stores in tissue samples from spectra data [188].

In order to reveal the metabolic information from IR spectra, the second derivative of the spectrum matrix is taken to reveal underlying band peaks in the carbohydrate band region of the IR spectrum . Most of the peak positions in the carbohydrate band are easily found in the second derivative spectra.

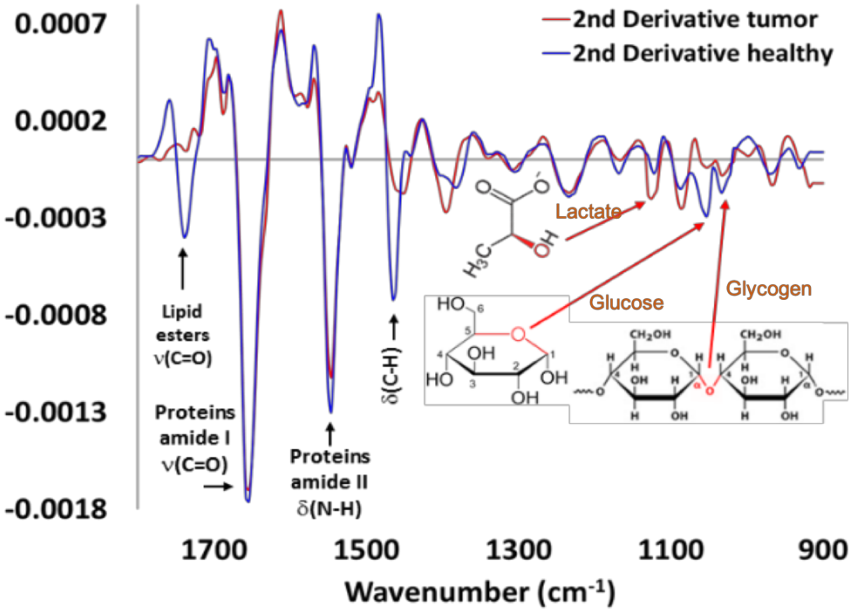

Figure 41 Second derivative spectra of a pathological mouse brain showing the peak position of glucose, glycogen and lactate in the spectrum from tumor site and healthy tissue [186].

The peak position of glucose is revealed at 1031cm^{-1}, glycogen is revealed at band peak 1024 cm^{-1} and 1162 cm^{-1}. Lactate is revealed at band peak position 1127 cm^{-1}. Figure shows an example of metabolism analysis of a pathological mouse brain by IR microscopy. The figure shows the depletion

of glucose-glycogen store and consequently the increase of lactate, thus showing the presence of an increase in glycolysis.

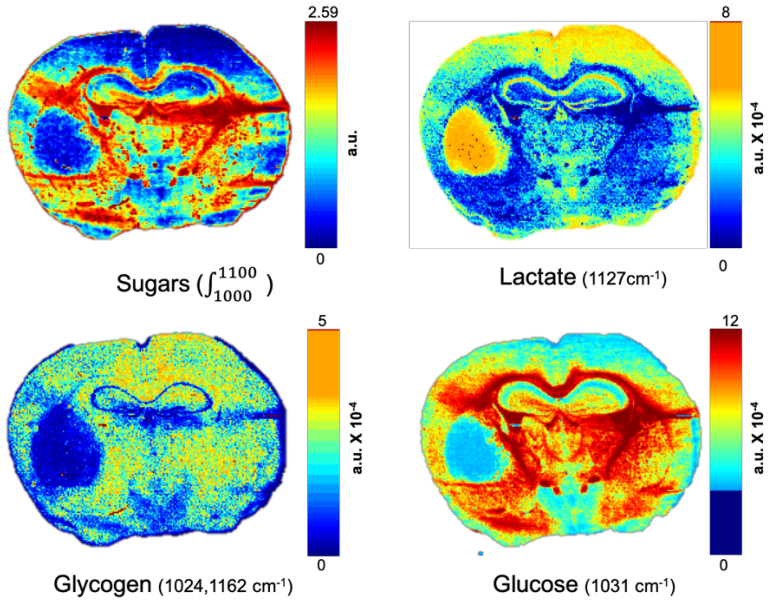

Figure 42 Metabolic analysis showing increase in glycolysis in the tumor region resulting in increase in lactate distribution and the depletion of glucose-glycogen store

3.6. 3D Reconstruction

In this section, we present a general methodology for reconstruction of 3D volume of IR metadata images. In line with the objective of this thesis, we focus on brain imaging application. Thus our experimental strategy is demonstrated on the 3D reconstruction of mouse brain metadata images.

Several methods have been proposed for the 3D reconstruction of tissue blocks, but the tissues were first stained or block-face photographic volume registration was used with MRI to help correct the shape in the soft tissue images [113, 189]. However, the use of labelling and staining methods or gadolinium injections for MRI prevent further “unaltered” chemical analysis.

Our methodology overcomes such a bottleneck, providing both an image registration and correction method for reconstructing 3D tissue blocks, and can determine the molecular concentrations in 3D at microscopic resolution. The key advantage is the development of a genuine combination of in vivo 3D imaging with quantitative spectro-microscopy for producing a 3D quantitative chemical image of a tissue block [186].

Our strategy is a multimodal approach based on the combination of *in vivo* acquisition of the 3D image of the mouse brain in the skull with metadata images from infrared (IR) spectro-microscopy for the histological analysis.

This is a Volume-to-Slice based approach for 3D reconstruction of histological images. Virtual tissue sections from the X-ray tomogram allows the correction of the shape distortions in 2D-IR image. Consequently, we could obtain a 3D patch of corrected 2D-IR images, constituting a 3D-IR spectrum matrix for the quantitative chemical analysis of native brain contents.

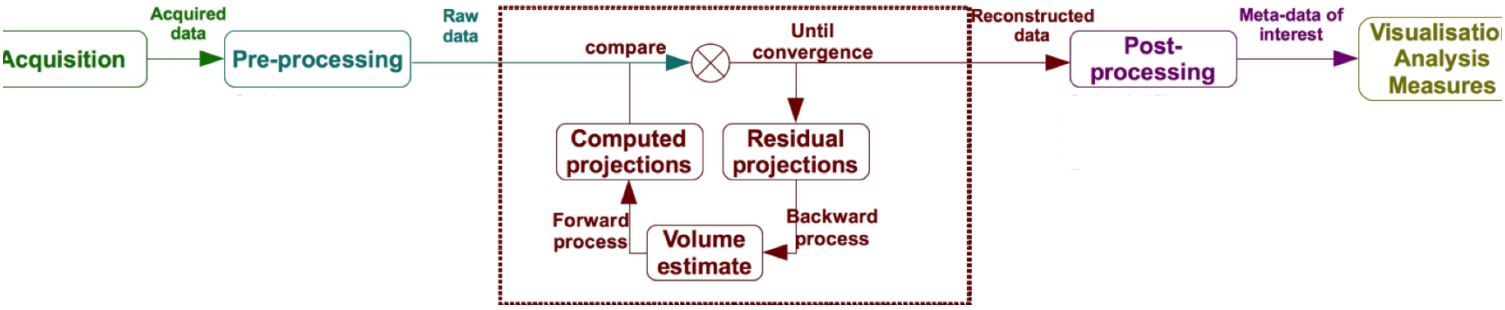

Figure 43 Pipeline for 3D reconstruction of IR metadata images. This includes the acquisition of x-ray tomographic data, pre-processing by denoising, smoothing and artefact correction, tomographic reconstruction by iterative methods, post-processing methods such as segmentation, deformable registration with IR data and visualization methods such as shape analysis and chemical analysis of reconstructed volume.

This methodology is divided into two major parts. The reference model acquisition which entails X-ray tomographic reconstruction of different x-ray projections of the mouse brain skull and the hierarchical image registration method for 3D reconstruction of 2D-IR images.

3.6.1. Reference Model Acquisition

3D reconstruction of tissues generally is an ill-posed problem with many possible solutions in the absence of a real model to validate the stacking of tissues. Thus as detailed in Chapter 2, we propose the use of a reference model for guiding the 3D reconstruction of mouse brain tissues.

The heads of the mouse can be analysed with and without brain inside the skull to obtain the actual brain volume by subtraction of segmented 3D images. This can be achieved by micro-radiology using X-ray imaging.

The objective is to obtain a 3D image of the brain without altering its contents due to X-rays, and the choice of X-ray microscopy is also to avoid the use of contrast agents or labelling methods (as for MRI), which modify the chemical contents of the tissues.

The volume rendering from 3 axial absorption projections allows to obtain a reconstructed realistic CT shape of the mouse brain which can be used to virtualize all tissue sections and create a 2D mask of their planar limits.

X-ray Tomographic Reconstruction

The goal of tomographic reconstruction is to recover the interior structure of a body using external measurements from many different projections (directions), and tomography is based on deep pure mathematics and numerical analysis as well as physics and engineering.

To reconstruct the X-ray images obtained at different angles of the skull into a 3D volume, we use the knowledge of the principle of tomodensitometry which is also used in CT imaging. Tomodensitometry measures the attenuation of the radiation going through an object in an X-ray line.

As X-rays travel from the X-ray source through an object to an X-ray detector, they are attenuated by the material on the x-ray line (neglecting scatter and diffraction). In monochromatic X-rays, the linear attenuation coefficient is proportional to the density of the object; thus, if we are able to estimate the attenuation, we can recover the density of the object [190].
So, let $f : \mathbb{R}^2 \rightarrow R$ be the density of the object. Mathematically, the goal of X-ray CT is to recover f from the attenuation measurements. Given a point x in an object, according to Beer's Law, if $I(x)$ is the number of X-ray photons in the beam when it arrives at x, then the intensity in a small segment of length Δx is decreased by the multiplicative factor $f(x)\Delta x$.

This is a classical Radon transform(Appendix) problem and is given as:

$$R_\theta(\rho) = \int_{-\infty}^{\infty}\int_{-\infty}^{\infty} f(x,y)\delta(\rho - x\cos\ \theta - y\sin\theta)dxdy \tag{23}$$

To reconstruct 3D volume of an object from the x-ray attenuation measurements, the classical algorithm used in CT image reconstruction from different projections is the filter back projection algorithm. However, this algorithm is ill-posed and requires a lot of projections for accurate 3D reconstruction. This is not practical for our application due to the risk of burning of the mouse brain sample from heat of x-ray radiation.

The iterative reconstruction algorithm shows more advantages than conventional filtered back projection (FBP) algorithm in dealing with the reconstruction problem with incomplete projection [191]. The iteration process can be initiated with an empty image estimate or using prior information, for example, a standard FBP reconstruction or a volume of a similar object. In general, the better the prior images match the final images, the faster the process converges towards a stable solution.

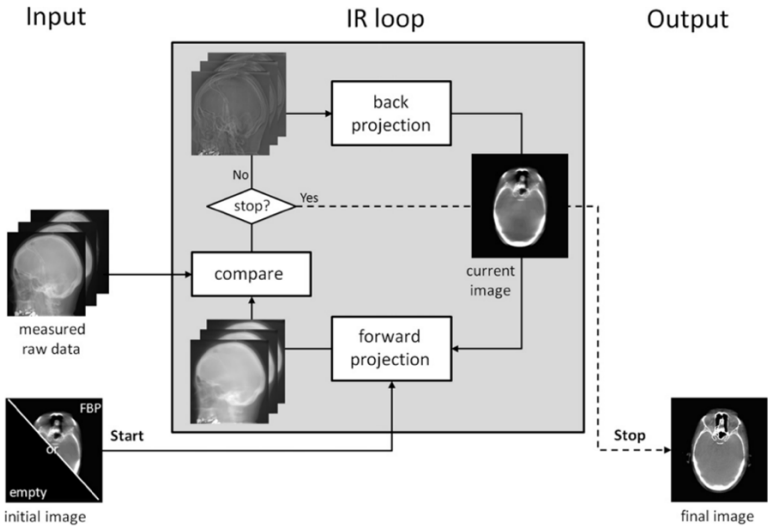

Figure 44 Iterative tomographic reconstruction algorithm process.

Iterative reconstruction methods consist of three major steps which are repeated iteratively as shown in Figure 44. First, a forward projection of the volumetric object estimate creates artificial raw data which, in a second step, are compared to the real measured raw data in order to compute a correction term. In the last step the correction term is back projected onto the volumetric object estimate [192].

The iterative process is finished when either a fixed number of iterations is reached, or the update for the current image estimate is considered small enough or when a predefined quality criterion in the image estimate is fulfilled.

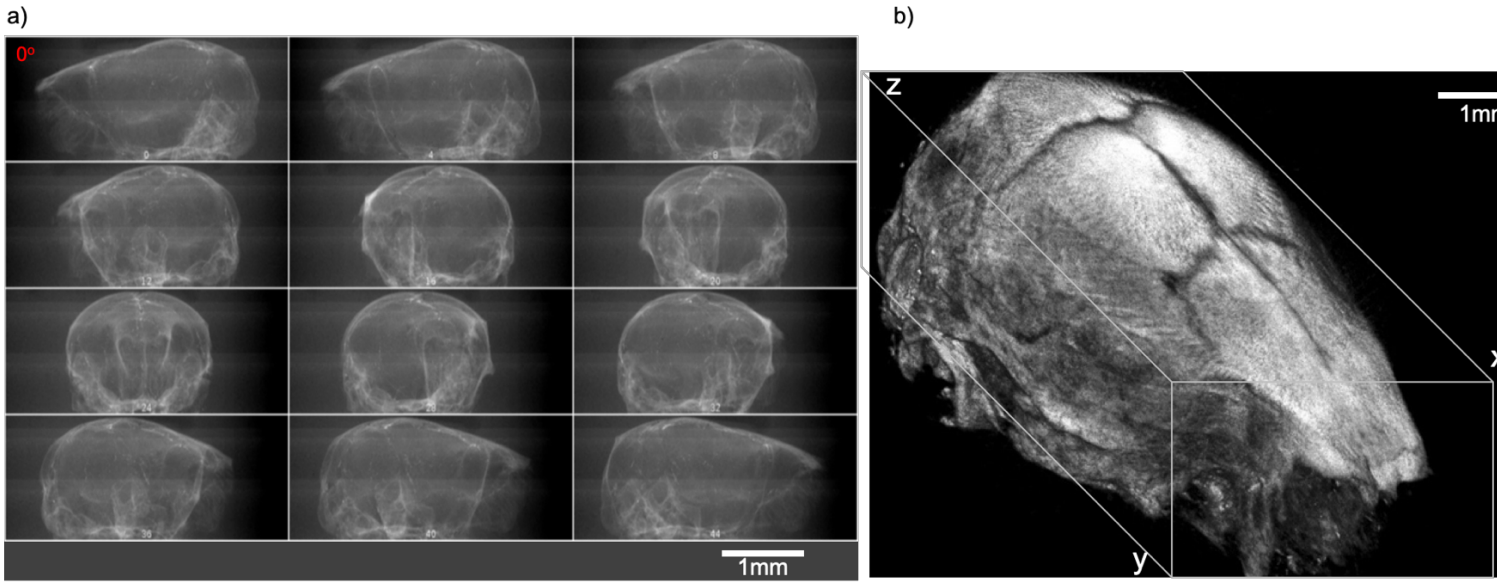

Figure 45 X-ray tomographic reconstruction of the mouse skull from x-ray projections.(a) 12 x-ray projections of the mouse skull used for the tomographic reconstruction of the mouse skull volume in (b).

3.6.2. 3D Hierarchical image registration method for 3D reconstruction of 2D-IR metadata images

I propose a novel 3D reconstruction method for 2D-IR stack. Our method is a hybrid approach which combines volume-to-volume and slice-to-slice registration methods for 3D reconstruction.

The volume-to-volume registration is applied to achieve a global alignment between the 3D volume of IR stack and the reference image volume obtained by x-ray tomography. This is done together with a slice-to-slice registration to correct large and small anatomical structures in the IR stack.

Our proposed method can be divided into three serial steps implemented in a hybrid CPU/GPU model to high performance and to improve computation speed. The first step is the global alignment of the 2D-IR stack, this is followed by registration of the tissue stack using virtualized section from the x-ray reference model on the GPU server and then a final refinement is done by locally deforming similar anatomical structures to using optical flow method.

(i) Global alignment of slices

The step of our proposed method is a global alignment of the 2D-IR stack. I propose a rigid transformation method to correct the translation and rotational differences between slices. As discussed in, log polar phase correlation method offers an accurate rigid transformation parameters estimation.

The accuracy of the global registration depends on the initializing slice. I propose a manual selection of a 'correctly' oriented slice chosen as the center slice. In an iterative manner, all slices are aligned in conformity to this slice by estimating the rotation and translation difference from the center slice.

(ii) Global registration with X-Ray model

The global registration with X-ray model step is to correct the global shape of tissue slices. The x-ray tomogram is virtually sectioned to the number of tissue slices and a mask of each virtual section is obtained.

This is followed by a simple shape matching algorithm to estimate the virtual mask that corresponds to each tissue slice. An affine transformation is performed to deform teach tissue slice to its corresponding virtual slice.

(iii) Local registration of brain sub-structures

Local registration is done to correct the deformity between similar anatomical structures in serial tissue sections. As discussed in section 2.4. Registration methods for 3D histology reconstruction, we propose the use of optical flow estimation with deformable transform to estimate and correct motion changes between similar anatomical structures in between tissues.

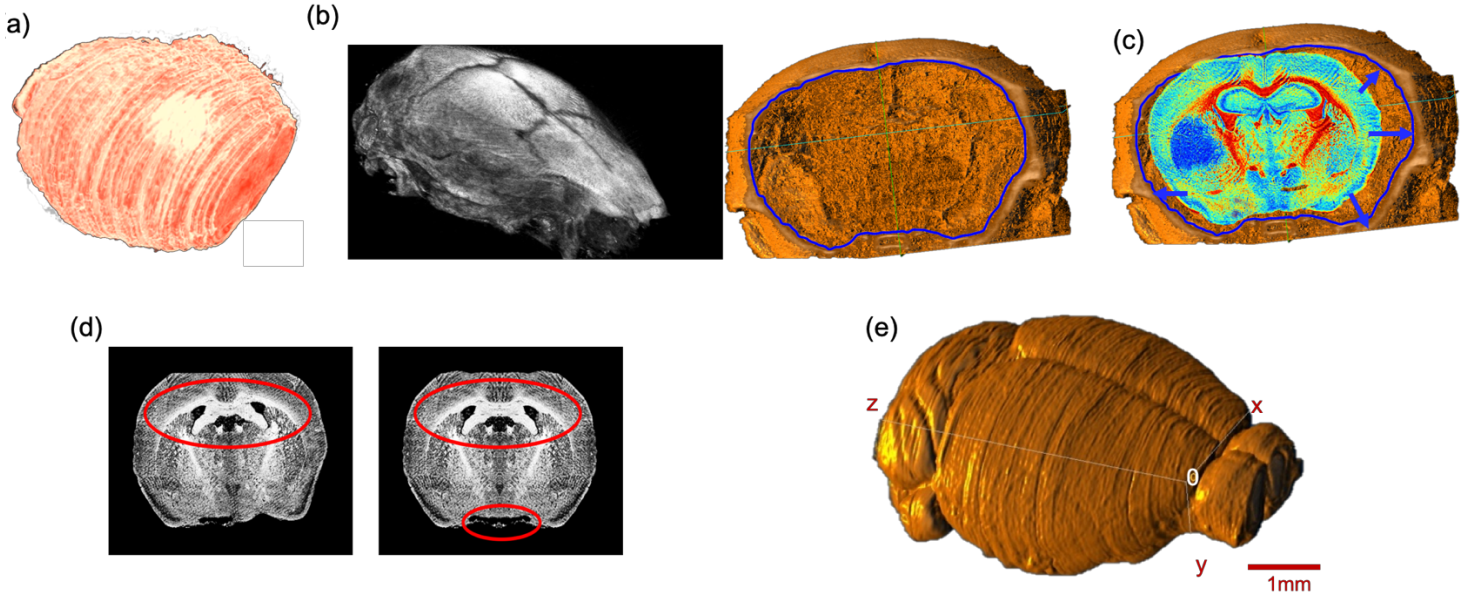

Figure 46 Global and local alignment of sample mouse brain dataset. (a) 3D volume obtained after rigid alignment tissue slices showing global shape deformity. (b) Virtual sections created from X-ray model. (c) Mapping and deforming IR metadata image to x-ray virtual section. (d) Local motion correction of tissue substructures. (e) 3D reconstructed volume of mouse brain.

Below is a detailed step of our proposed 3D hierarchical image registration for 3D reconstruction of 2D-IR metadata images.

Algorithm

Input: set of unaligned 2D-IR metadata images S = {1,…n}, 3D x-ray reference model M

Output: 3D reconstructed IR metadata volume

1. Let $\boldsymbol{S_0}$ be an arbitrary slice manually selected as the center slice.
2. Compute the rigid transformation parameter of all slices of each slice with respect to $\boldsymbol{S_0}$.
3. Apply affine transformation on all slices to align them to $\boldsymbol{S_0}$.
4. Virtually section $\boldsymbol{M}$ into a set of virtual sections $\boldsymbol{V}$.
5. $\forall\, \boldsymbol{v} \in \boldsymbol{V}$, compute the mask $\boldsymbol{v_m}$ of the virtual section slice.
6. $\forall\, \boldsymbol{v_m} \in \boldsymbol{V_m}$, find the most correlated slice $\boldsymbol{s} \in \boldsymbol{S}$
7. Compute the deformable transform that deforms $\boldsymbol{s}$ to correspond to $\boldsymbol{v_m}$
8. $\forall\, \boldsymbol{s} \in \boldsymbol{S}$, estimate the optical flow of $\boldsymbol{s_{i+1}}$ and $\boldsymbol{s_{i-1}}$ which are the section that preceded and follow $\boldsymbol{s}$
9. Apply a deformable transformation to correct motion changes in $\boldsymbol{s}$
10. Stack the globally aligned and local motion images in S to obtain a 3D reconstructed volume of the sample.

CHAPTER 4: 3D Chemical Imaging of Tumors in Mouse brain

In this chapter, we introduce a direct application of our proposed methods for 3D imaging by IR microscopy. I demonstrate the application of our methods to investigate to precision a specific anatomical structure in the mouse brain. I applied our proposed methods to the chemical imaging of tumors in the mouse brain. Our aims can be summarized as follow:

a. To demonstrate that 3D chemical imaging using IR spectro-microscopy can be used for the 3D pathological investigation of large tissue blocks and the comparative advantage over classical histology.
b. To demonstrate that quantitative metabolic parameters can be extracted from the IR spectra for the characterization of the brain metabolism vis-a-vis tumor metabolism (assessing the Warburg effect in tumors).
c. To demonstrate that 3D IR spectro-microscopy can achieve a quantitative molecular analysis of tissues

Here, we present the methods used in our experiments and thereafter the results and perspectives drawn from our experiments using a mouse brain in which glioma tumor cells had been implanted to grow a tumor in 28 days before the acquisition of 3D in situ and 2D histological images.

4.1. Methods

Below are the methods used in our experiments from sample preparation to 3D quantitative molecular analysis of tumors in the mouse brain:

4.1.1. Sample preparations

The 3D image model of the mouse brain used for 2D and 3D IR image corrections has been obtained on healthy animals (10 to 12-week-old male rag-$\gamma 2C^{-/-}$ immunodeficient mice). A series of 12 animals were used for acquisition of the head 3D image after dissection. The dissection consisted in the removal of the skin, eyes, tongue, teeth, etc. as to obtain the skull and the brain sample.

The X-ray tomographic images were obtained in sequence with and without the brain (360 projections over 180 degrees, providing a 2-µm resolution meshing of the brain). For skull imaging, the brain was aspirated through the occipital hole. The internal part of the skull was further cleaned from possible tissue remains by enzymatic digestion (Liberase TL, Roche ref 05401020001) for 20 minutes at 37°C.

The low-dose X-ray images of the brain further used for IR analyses were obtained using 3 projections (-90, 0, and 90 degrees) in same conditions as the 360 projection high resolution images, thus limiting the x-ray dose to negligible amount (not heating the brain before histological analyses). The aim was to reconstruct the 3D model of the brain with limited 2D projections by using the high-resolution X-ray tomographic images as references.

The mouse brains prepared for 3D histological analyses had been xenografted with NCH421K glioma tumor spheroids (proneural, stem-like cells). Briefly, primary tumor-derived NCH421K spheroids (5 spheroids of $10.^4$ cells per mouse) were implanted into the right cerebral cortex using a Hamilton syringe fitted with a needle (Hamilton, Bonaduz, Switzerland) and following the procedure already described [24].

Animals were anesthetized using Imalgene 1000 (Ketamin 10 g/100 ml) injected intraperitoneally. Mice were fixed using a stereotaxic alignment instrument. Injections were realized in the striatum (2.2 mm on left from bregma 0 and 3 mm of depth) using Hamilton syringe. An analgesia is realized (Buprenorphine 0.1mg/kg) before and after brain implations according to the ethical criteria.

Full brains (with xenografted tumor on one lobe and healthy brain on the other lobe) were removed from sacrificed mice after 28 days of tumor growth. The sample holder with brain were inserted in a plastic tube and plunged into liquid N_2 for instant freezing. The frozen brain was deposited in the upright position (with cerebellum on the bottom) on cooled glue (polyvinyl alcohol for cryostat, -20°C) to avoid tissue embedding. The total duration from the death of animal to the complete freezing of brain was always less than two minutes, what guaranty that degradation in brain cell and tissue contents was limited.

After freezing, additional glue was used to homogenize the sample as a regular block intended for cryosections (Cryostat CM1900, Leica-Microsystems, France). A complete sectioning of the brain was performed at 20-µm thickness. A total of 340-385 sections was obtained depending on the brain

dimensions (the sectioning was stopped in the cerebellum mass). In the example of 3D brain reconstructions shown in the results, 1 section was reserved for histology (deposited on gelatin-coated slides) and the following section was reserved for IR microscopy (deposited on CaF_2 windows having the same dimension as histological slides), and so on alternatively for the complete series of sections.

For histological imaging, all tissue sections were incubated with antibodies against human vimentin antigens (Santa Cruz 6260) and a green fluorescent secondary antibody (goat anti-mouse 488 antibody, Interchim FP-SA4010). Imaging was carried out by using a Nikon eclipse E600 microscope.

4.1.2. X-ray image acquisitions

Microradiology was performed with unmonochromatized (white) synchrotron X-rays emitted at the 01-A beamline wavelength shifter of the National Synchrotron Radiation Research Center (NSRRC, Hsinchu, Taiwan). The photon energy ranged from 4 keV to 30 keV with critical energy at ~12 keV; the beam current was kept constant at 360 mA with the top-up operation mode all over acquisition periods.

To obtain 4.59×3.43 mm images X-rays were converted into visible light using a $CdWO_4$ single crystal scintillator and then detecting the photons with an optical microscope equipped with a 1600 × 1200 pixel CCD camera (model 211, Diagnostic Instruments). I reduced the radiation dose by attenuating the X-ray beam with two 550 μm silicon wafers. The dose was 33.9 Gy per 100 ms for a specimen thickness of 1 cm placed before the sample. The sample-scintillator distance was 5 cm. I used a 2× lens in the optical microscope to obtain the desired field of view; the pixel size in the final image was 2×2 μm^2.

A simple background flattening image filter was used for large area micro-radiology images. The conceptual details of synchrotron-based microtomography, including absorption and phase contrast, have been discussed in previous study[53]. The high-resolution tomographic images were captured with 360 angles over 180 degrees. The low resolution (and low X-ray dose) images were captured with 3 angles (-90, 0, 90 degrees) and reconstructed using the high-resolution models.

4.1.3. IR acquisitions for 20-µm spatial resolution imaging

I analyzed the mouse brain tissue sections by IR microscopy. The QCL-IR microscope (Spero®, DaylightSolutions, CA, USA) is equipped with 4 IR lasers providing wavelengths every 4 cm^{-1} along the 1800-900 cm^{-1} spectral interval, thus 225 absorption values. The microscope is constantly purged with dry air and sample compartment is isolated from ambient air by a plastic box. The detector is a non-N_2-liquid frozen focal plane array (FPA) detector with 480x480 elements.

The acquisition of IR images was setup for a final 21-µm resolution (the closest dimension with respect to the 20-µm tissue sectioning thickness), although the raw images had a 4.2-µm lateral pixel size (using the low magnification optics). The 20-µm pixel size was obtained after acquisition by binning 5x5 pixels. IR image acquisitions lasted up to 2 hours per section at the largest tissue section dimensions, ~6x8 mm).

A total of 170-190 IR images was obtained per brain for the 3D-IR image reconstruction (same number for the corresponding histological image providing a comparison between tumor volumes). The microscope was installed in a thermally controlled room (20°C) for standardizing the ambient conditions during acquisitions over the total duration of acquisitions (2 months). Raw IR image data were stored on server and duplicated for saving a set of 2D-IR images at ~20-µm resolution.

4.1.4. 3D IR and 3D histological images reconstruction

For the 2D- and 3D-IR images presented here, we used a mouse brain from which 370 sections were obtained by continuous cryomicrotomy. Therefore, 185 2D-IR images were obtained and represented a matrix of 9.4-million IR spectra and 140 Gb of raw data on a storage server (after processing the 5x5 pixel binning).

The same number of histological sections was obtained, alternatively to the IR sections during the continuous cryomicrotomy. The visible images of IR and histological sections, obtained right after sectioning on a transmission optical microscope (Nikon AZ100M), were merged into a full set of reference images of the mouse brain. These visible images were coupled to the 2D masks of virtual brain sections extracted from the 3D X-ray tomogram of the mouse brain for further corrections and resizing.

The resizing of 2D-histological images was done by edge-guided image interpolation. The first and last images corresponding to the actual set of tissue sections (histological and IR – 370 images) are defined according to the optical (visible) images took immediately after cryomicrotomy. The 2D-mask of each image is extracted from the actual volume of the mouse brain (respecting a 20-µm distance between 2D-masks to match the thickness of histological sections).

The lacking 2D-masks (370 sections vs. 100 images in the Allen brain atlas) are completed for correction of all tissue sections. Histological images were corrected for shape alterations by edge-guided image interpolation with their corresponding 2D-mask for reference.

The IR images were corrected by re-pixelation and redistribution of the full spectral absorbance at the 2D image level. A pixel grid at resolution of the IR image (here 21-µm lateral resolution) covers the 2D-mask that the 2D-IR image must match. The IR spectra contained in IR image pixels are redistributed in the pixel grid of the 2D-mask.

The total spectral absorbance of the 2D-IR image is calculated before and after IR spectra redistribution to ensure that the chemical information of the tissue section remains unchanged. The 185 histological images are positioned in the actual volume model of the mouse brain for 3D alignment and patching.

The alignment is performed by anatomical pattern recognition with respect to the Allen brain atlas images and the 2D-masks. Typical anatomical features are salient angles found at the surface of brain volume, such as the longitudinal cerebral fissure, the lobes-cerebellum interfaces, etc.). The 185 2D-IR images are also aligned and patched according to the same procedure as for histological images.

4.1.4. Brain metabolic assays

In a series of 10 mice with 18-23 days of tumor development in the right hemisphere, brains were harvested for dissection of the left hemisphere (healthy tissue). Tissues were immediately weighted and brain homogenates were obtained by sonication in 10% wt/vol of 0.1 N NaOH and 0.01% SDS and centrifuged for 15 min at 16,000 g at 4°C.

The supernatant was acidified and diluted with 0.03 N HCl. Glycogen and glucose were measured by a fluorescence enzymatic assay using the amyloglucosidase method[39]. Glycogen was digested with

amylo-α-1,4-α-1,6-glucosidase (AG) (Sigma). The glucose levels were determined with hexokinase and glucose-6-phosphate dehydrogenase (Sigma) through formation of NADPH from the reduction of $NADP^+$.

Glucose levels obtained from samples without AG were subtracted from samples with AG to determine glycogen levels. Glycogen and glucose were expressed both as micromoles per gram of fresh brain tissue (µmol/g). The effects of SD were evaluated by t-tests. For lactate, brain homogenates (20 mg) were added to 100 µl of ice-cold 3 M perchloric acid, homogenized using a homogenizer, and then centrifuged at 1,000 g for 5 min at 4°C. The resulting supernatant was mixed with buffer containing glycine, hydrazine, and NAD and then added to LDH.

The fluorescence measurements were taken at 350 nm excitation and 450 nm emission. The lactate concentration was calculated from a standard curve. For comparison with IR spectral data, statistical tests were considered significant if $P < 0.04$.

4.1.6. IR spectra data treatments

(a) IR image post-processing:

The corrected 2D-IR images were cropped to remove pixels (and thus IR spectra) out of the brain section (containing OCT glue and other features that could bring artefactual data after spectra data treatments, and thus alter the quality of the final 3D images derived from the 3D IR spectrum matrix) and the 3D-IR image was patched as a 3D spectrum matrix of the brain only.

All IR spectra were baseline corrected using a standard procedure (elastic correction based on null absorption at 1800 cm^{-1}). Absorbance spectra were first used to check that spectral intensity scale was consistent between IR images.

(b) 3D-IR image reconstruction:

The ∫(1800-900 cm^{-1}) spectral intensity integration was calculated for all IR spectra and the 3D image was reconstructed (full spectral intensity 3D image of the brain). The full spectral intensity typically ranges between 0 and 300, and this scale was applied to all 2D-IR images before 3D reconstruction.

The 3D patch of 2D-IR images was first performed with uncorrected 2D-IR images (figure 2) to show the mediocre volume rendering induced by the multiple tissue sections shape alterations due to surgery, sample deposition on sample holder, and cryomicrotomy.

The same 3D patch performed with corrected 2D-IR images by X-ray imaging allowed to align properly each 2D-IR image according to observable external anatomical details as explained above. Therefore, although the spectra data treatments were applied on 2D-IR images, the positioning of each 2D-IR image in the 3D alignment was fixed for all volume renderings.

(c) Tumor volume:

Importantly, the positioning of the 3D-IR image of the brain inside its skull was used to check that all 2D-IR image resizing and corrections could accurately recover the internal anatomy of the brain, which also resizes the tumor.

I performed the segmentation and meshing of the tumor volume after a classical spectroscopic analysis, i.e., by calculating the protein-to-lipid absorption ratio $\int(1700\text{-}1480\ cm^{-1})/\int(1760\text{-}1710\ cm^{-1})$. The mesh of the tumor volume is extracted as an independent volumetric image for shape comparison with its 3D-histological image.

The meshed tumor volumes, IR and histological, were subtracted as polysurfaces to check the relevance at using the protein-to-lipid absorption ratio to reveal a glioma tumor in the brain. The difference between IR and histological meshed volumes was measured and expressed as a percentage of the histological (reference) volume.

The difference between meshed volumes of the tumor from uncorrected and corrected 3D-IR and 3D-histological images was also calculated to show the effect of 2D image corrections on tumor volume rendering.

(d) Anatomical regions:

To exploit the full spectral intensity 3D-IR image of the brain, anatomical regions were directly segmented from intensity scale manipulation. In 2D images, many different anatomical regions appear as a color gradient respective to the intensity scale rendering.

For every 2D-IR image, we segmented the color gradients and checked for anatomical regions reconstructions in 3D from the 3D-IR image (where successive segmented 2D images provide continuous 3D structures).

To that end, we selected 10, 25 or 50 color gradients, depending on the refinement expected in 2D images, depending on its complexity. I used a standardized min-max intensity scale on all 2D-IR images with rainbow-related rendering: blue-green-yellow-red-white. The same color gradient scaling was used for all 2D- and 3D-chemical images presentations.

Once an anatomical structure could be highlighted and meshed in 3D, it was extracted and saved as an independent image for separated analysis. The full 3D-IR image of the brain could be used again for determining other anatomical regions using other levels of color gradients on intensity scale, and so on. The anatomical regions were systematically compared to the existing anatomical atlases of the mouse brain, the Allen brain atlas for example.

(e) Quantitative metabolic analyses:

Several metabolic parameters (glucose, glycogen, lactate) were quantified in 2D-IR images and the distribution of concentrations was determined as follows:

1- Second derivative IR spectra were calculated for the whole 3D spectrum matrix of the mouse brain. IR spectra of the left hemisphere (healthy tissues) and for the tumor (from its meshed volume) were analyzed separately.

2- The absorptions of glucose (1031 cm^{-1}) [53], glycogen (1024 and 1162 cm^{-1}), and lactate (1127 cm^{-1}) [188] were measured by integrating band areas on second derivative spectra (glucose: 1040-1027 cm^{-1}; glycogen: 1027-1018 and 1167-1157 cm^{-1}; lactate: 1135-1114 cm^{-1} – expressed in a.u.² $x10^{-4}$);

3- Since there is no histological method to determine the concentration of these metabolic molecules on histological sections, the calibration of molecular concentrations was established considering the average value of their absorptions as equivalent to the values of metabolic assays on the brain homogenates obtained in parallel with another batch of 10 mice (same sex, age and experimental conditions, with a glioma tumor implanted the same day as for mice used on histological/IR experiments). The calibration was performed using only the left hemisphere part of the 2D-IR images (healthy tissues not affected by the tumor). The scaling of molecular concentrations was done according to the distribution of IR absorption for each molecular absorption (a.u.² $.10^{-4}$ ± SD vs. µmol/g → µmol/g ± SD). The normal distribution of absorptions (mean ± 3x SD, in a.u.² $.10^{-4}$ - data not shown) was calculated for the left hemisphere of the brain and for the tumor volume to reveal the heterogeneity of metabolic parameters between anatomical regions (mean ± 3x SD, in µmol/g).

4- The IR spectra corresponding to the anatomical regions meshed from the left hemisphere (cf. "Anatomical regions" paragraph) were analyzed separately to reveal the mean ± SD values of metabolic parameters and plotted
5- 3D-plots of molecular concentrations in the whole mouse brain were produced with volume rendering. The double intensity label (a.u.² .10^{-4} and µmol/g) is provided.

4.2. Results

The results shown in this thesis are related to a mouse brain in which glioma tumor cells had been implanted to grow a tumor in 28 days before acquisition of 3D *in situ* and 2D histological images. The presence of a tumor in the brain was the perfect challenge for a quantitative chemical analysis of tissues: tumors are highly different from healthy tissues in terms of chemical composition (usually with higher protein and lower lipid contents [193]) and metabolism [194]. I achieved to show these differences with a quantitative chemical analysis of the mouse brain using the following methodology:

4.2.1. Acquisition of the actual 3D shape of the brain

I first used mice heads for X-ray tomographic analysis of the brain volume. Heads were analyzed with and without brain inside the skull to obtain the actual brain volume by subtraction of segmented 3D images. The segmentation method we used allowed to obtain the meshing of brain with a 2-µm accuracy.

The high-resolution images were used as models for resizing the low-dose 3-projections X-ray images. The objective was to obtain a 3D image of the brain without altering its contents due to X-rays, and the choice of X-ray microscopy is also to avoid the use of contrast agents or labeling methods (as for MRI [195], PET/SPECT [196], intravital imaging [197], mass-spect imaging [198], etc.), which modify the chemical contents of the tissues.

It would have thus affected the chemical analyses by IR microscopy after histology. The volume rendering from 3 axial absorption projections allowed to obtain a realistic CT shape of the mouse brain that was used to virtualize all tissue sections and create a 2D mask of their planar limits.

The main issue following the acquisition of a brain volume from 3 axial absorption projections was to determine the beginning and ending point of brain sectioning as well as the actual axis of

sectioning. This issue was solved by using an available anatomical atlas of the mouse brain, the Allen Developing Mouse Brain Atlas [199].

I resized the atlas with respect to the actual volume of the mouse brain. I used a graph-theoretic slice-to-slice reconstruction with a global histology-to-CT reconstruction to achieve high accuracy, both in the alignment of features between slices and in the 3D shape of the reconstructed brain.

4.2.2. Acquisition of a 3D IR spectrum matrix of the brain

After acquisition of the three X-ray projections for volume rendering of the brain, the organ was removed from skull and deposited in the upright position (with cerebellum on the bottom) on sample holder for continuous cryomicrotomy at a 20-µm thickness. A series of 340-385 sections could be obtained depending on the organ size.

Alternatively, one section was reserved for conventional histology (named histological images) and one section was reserved for IR microscopy analysis (named IR images). The goal was to obtain a series of histological sections sufficiently representative of the whole brain for comparative analyses between IR microscopy and histology, and for 3D image reconstructions.

An example of 2D IR image of the mouse brain with typical IR spectra from different anatomical regions is shown in Figure 47.

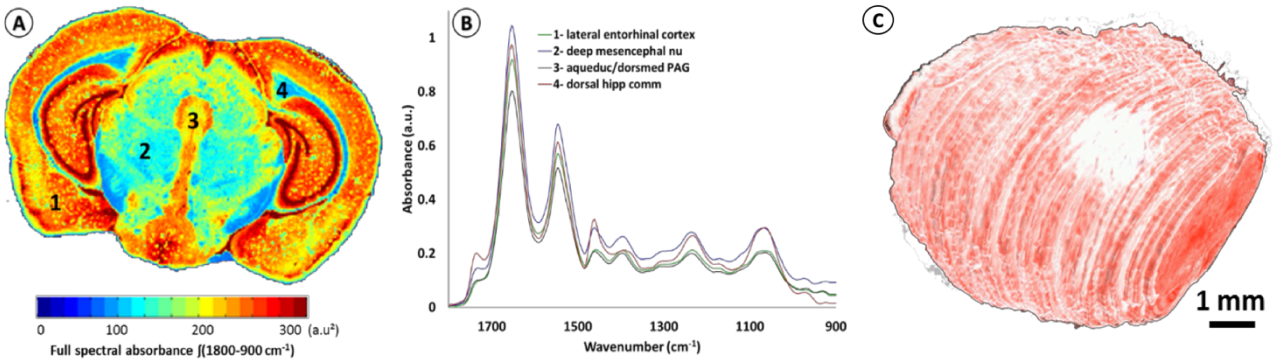

Figure 47 3D-IR reconstruction of mouse brain. a) Sample IR image of the full spectral absorbance. (b) Sample spectra from infrared image. (c) 3D reconstruction of uncorrected IR image stack.

Figure 47 show a 3D-IR image obtained from a mouse brain:

A. The 2D-IR image of the section shown is approximatively located at Bregma -4.04 mm / internaural -0.24 mm. The mouse brain has been sectioned at 20-µm thickness (370 sections). The IR image is shown as a full spectral absorbance (in a.u.²).
B. The IR spectra in corresponding to the 1-4 positions marked in (A) are shown in the central panel. They show important absorbance intensity variations throughout the spectral interval (1800-900 cm^{-1}, also called the fingerprint region). These absorbance intensity variations allow recognizing the major anatomical regions of the mouse brain, which can be used for proper alignment using anatomical atlas of the brain (such as the Allen Developing Mouse Brain Atlas).
C. For the 3D-IR image reconstruction, the full spectral absorbance intensity scale was set free (set at 0 for artefactual pixels in 2D images, <1.5% of pixels for all images) for the 185 raw 2D-IR images obtained from mouse brain sectioning. The 3D patch shows that many tissue shape alterations where present on 2D-IR images.

IR spectra from different regions of the brain show quite different absorption profile, thus confirming that variations of chemical contents are significant. For individual 2D-IR images, the ∫(1800-900 cm^{-1}) intensity scale ranged 0-192 to 0-331 for the whole set of 185 images.

The intensity scale was set free for the 3D-IR image reconstruction. The first reconstruction of the 3D-IR image from 2D raw IR images (without any planar shape correction) was just center-aligned using the central axis between lobes as anatomical reference.

As shown in Figure 48, the general shape of the 3D-IR image of the brain contains numerous distortions. They came from organ shape alterations during surgery (due to the relapse of the brain volume once extracted from the skull, which exerts a pressure on brain tissues, and also due to the gravity-related collapse of this very soft tissue at deposition on the sample holder).

This is also due to the well-known tissue alterations during cryomicrotomy, where tears, bends, cracks, etc. appear at the tissue sectioning or deposition process. This is showing clearly the relevance of using a 3D *in situ* (or *in vivo*) imaging method for obtaining a realistic volume rendering of the mouse brain before histological analyses. This is also a critical to ensure further quantitative chemical analysis from the 3D-IR image.

4.2.3. Correction of the 2D histological images from 3D X-ray tomogram

The IR and histological images were corrected for shape alterations using the X-ray tomogram and the 100 virtual slices (from 100 images - Figure 48) given by the Allen Mouse Brain Atlas.

I first compared anatomical images with the IR and histological images to define the sectioning plan effectively used while obtaining all histological sections. The anatomical images are resized according to the actual 3D volume of the mouse brain. They serve as reference for comparing anatomical regions observed on visible, histological, and IR images.

Importantly, they allow defining the first and last sections obtained on a mouse brain by cryomicrotomy, which number is variable according to the size of the organ and some potential loss of sections at extremities. They are also used for proper alignment and 3D patching after shape corrections, as shown in Figure 48.

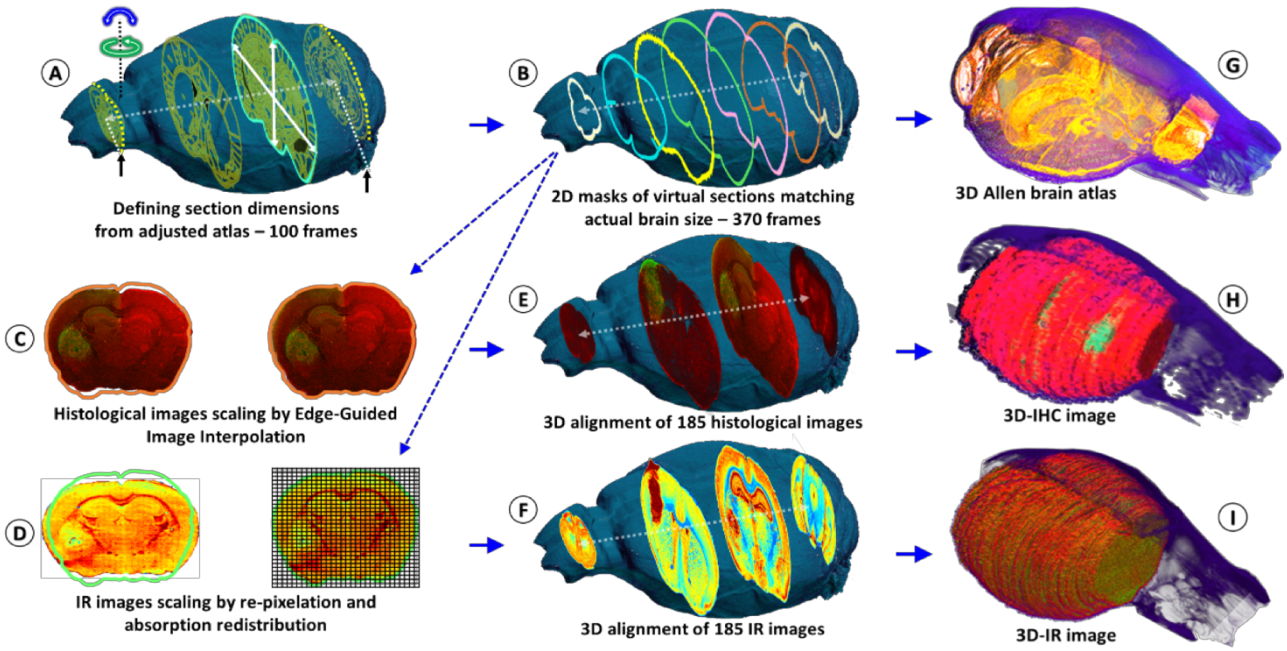

Figure 48 Schematic of the shape corrections process for 2D images and 3D volume reconstructions.

Figure 48 shows a detailed overview of the shape correction process.

A. The actual volume model of the mouse brain is used to resize the anatomical images of the Allen Mouse Brain Atlas. The first and last frames corresponded to the limits of the full set of tissue sections obtained by continuous cryomicrotomy (histological and IR – 370 sections).
B. The virtual 2D masks of the 370 images are extracted from the actual volume of the mouse brain.

C. The histological images are corrected by edge-guided image interpolation.
D. The IR images are corrected by re-pixelation and redistribution of the full spectral absorbance. The total spectral absorbance of the 2D IR image is calculated before and after IR spectra redistribution for validation of the image correction process.
E. The 185 histological images are positioned in the actual volume model of the mouse brain for 3D alignment and patching. The alignment is performed by anatomical pattern recognition with respect to the Allen brain atlas images in (A) and the 2D masks obtained in (B).
F. The 185 IR images are also aligned and patched according to the same procedure.
G. 3D reconstructions of the Allen brain atlas.
H. 3D-IR image resized to match the actual dimensions of the mouse brain.
I. 3D-IHC image resized to match the actual dimensions of the mouse brain.

The sets of IR and histological images (185 images for each set) were used for a brain volume rendering and the 3D histological image was segmented to highlight the tumor. I can observe that the reconstructed 3D images of the brain perfectly match the actual volume of the brain defined in by X-ray tomogram.

I applied a classical IR spectroscopy analysis to highlight the tumor from the 3D chemical image, i.e., the protein-to-lipid ratio defined by absorption ratio $\int(1700\text{-}1480\ cm^{-1})/\int(1760\text{-}1710\ cm^{-1})$, or the absorption ratio between amide I and lipid esters [2]. This analysis highlights the tumor mass, containing higher concentration in proteins and lower concentration of lipids than its surrounding tissues.

4.2.4. Anatomy of the brain based on 3D chemical data

An important objective of our study was to demonstrate that 3D chemical imaging by IR spectro-microscopy can be used for the 3D pathological investigation of large tissue blocks. I segmented the tumor mass based on a simple spectral analysis to compare it with tumor volume rendering from the 3D histological image.

As expected, the IR spectra extracted from the tumor and at a similar location in the left hemisphere show important differences for most of absorption regions. The shape of tumor volume was found very similar between IR and histological analyses, the calculation of Hausdorff distances between the

two volumes showing only marginal differences (3D-IR = 9.39 mm^3; 3D-IHC = 12.24 mm^3; difference ~30%).

The ability to extract the 3D spectrum matrix of the tumor mass is important to analyze specifically its chemical contents. This is also true for the healthy brain tissues (at least the left hemisphere, which is not affected by the tumor metabolism and the mechanical pressure it exerts on the surrounding tissues).

Figure 49 shows examples of segmentation performed on the mouse brain 3D-IHC and 3D-IR images, both for the tumor mass extraction and for defining anatomical structures from chemical analyses on the 3D IR image.

This segmentation can be based on absorption profiles extracted from spectra (as for the tumor mass with the lipid/protein contrast). It is noteworthy that healthy brain tissues and anatomical entities can be successfully separated directly from IR spectra (also using the important absorption differences shown in spectra of Figure 47).
Therefore, an anatomical atlas of the mouse brain might be developed from its 3D quantitative chemical image.

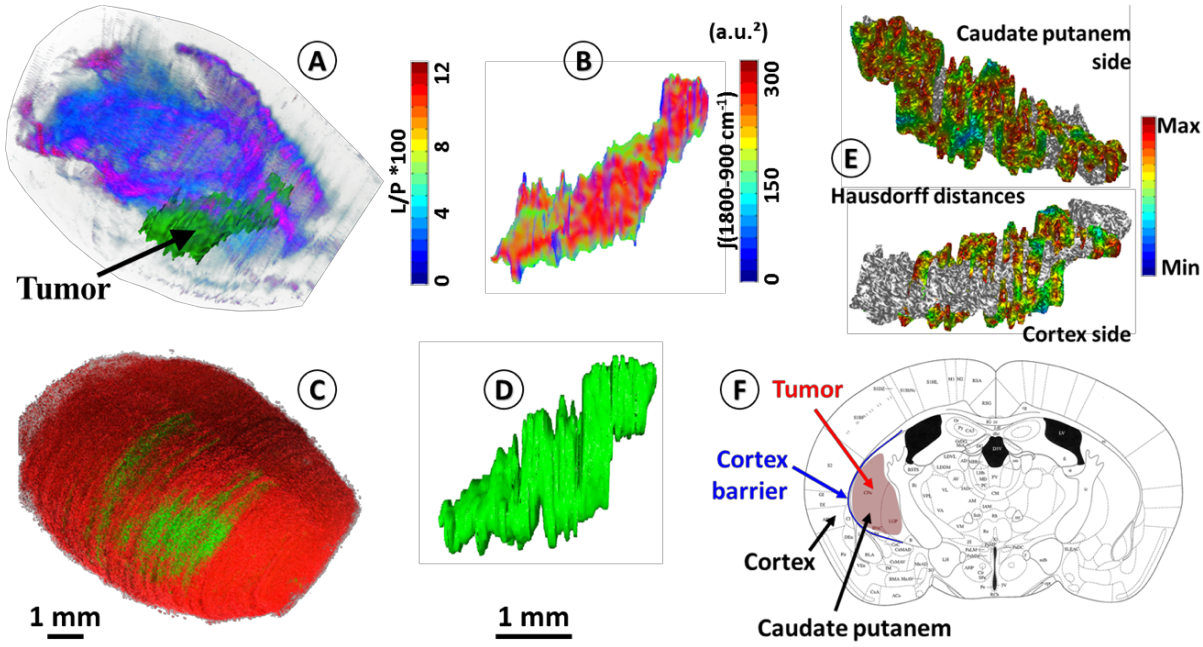

Figure 49 Segmentation of brain regions based on chemical contents.

Figure 49 shows the results obtained after the segmentation of different brain regions based on their chemical composition.

A. The 3D-IR image of the mouse brain in the skull highlighting the tumor mass using the [∫(1760-1710 cm^{-1})/∫(1700-1592 cm^{-1})*100] absorption ratio (L/P as indicated in figure scale legend).
B. 3D-IR image of the tumor mass extracted from whole brain by segmentation of the voxels presenting the chemical profile of the tumor (full spectral absorbance).
C. Tumor mass in the skull
D. Tumor mass extracted from the 3D-histological image by green channel segmentation.
E. Representation of the Hausdorff distances between the 3D-histology (reference) image of the tumor mass and its 3D-IR counterpart (both sides of the tumor mass).
F. Illustration of the tumor growth mechanics as revealed by the segmentation of 3D-IHC and 3D-IR images of the tumor volume with respect to the brain regions invaded.

The Hausdorff distance calculation shows very interesting features. The 3D-IHC tumor image is showing the tissue volume occupied by tumor cells while the 3D-IR tumor image is showing the tissue volume which chemistry is significantly altered by tumor.

The 30% difference between the two volumes represents the tissue volume where tumor cells are present but where they did not alter yet significantly the chemical composition of the tissue (i.e. tissue areas where tumor cells are dispersed).

The Hausdorff distance calculation between these two volume renderings of the same tumor informs us about the way the tumor developed: on one side, in front of the cortex, the 3D-IHC to 3D-IR differences are limited or null, thus the tumor was blocked by a cortex barrier (except along the "tunnel" formed by the needle when implanting the tumor cells); on the other side, the differences are larger, showing that the tumor had easier way to invade the parenchyma through the caudate putamen region.

This result illustrates the importance of 3D histology for understanding the anatomical-mechanical-chemical features that drive the development of a pathology.

4.2.4. Quantitative 3D metabolic images based on 3D chemical data

The last major objective of this study was to demonstrate that 3D IR spectro-microscopy will develop 3D pathology as a new avenue for biological research, notably by providing quantitative chemical analyses that no other technique had achieved till now.

With the example of a solid glioma tumor, the challenge was to analyze major metabolic parameters of the brain [200], the glycogen stores and the glucose-lactate metabolism through the concentration of these molecules. They collectively allow to address the so-called Warburg effect in tumor [194].

To obtain a quantitative analysis, we performed an absorption integration from the glucose [53] (1031 cm^{-1}), glycogen [188] (1024 and 1152 cm^{-1}), and lactate (1127 cm^{-1}) most specific IR bands on all IR spectra of the 3D IR image of the brain after calculating their second derivative, a standard procedure for a fast IR spectral data extraction[38].

From 2nd derivative spectra, the 3D mapping of molecular concentrations in the brain was found consistent between tissue sections and thus no major contrast aberration came to alter the visual rendering of these analyses as shown in Figure 50.

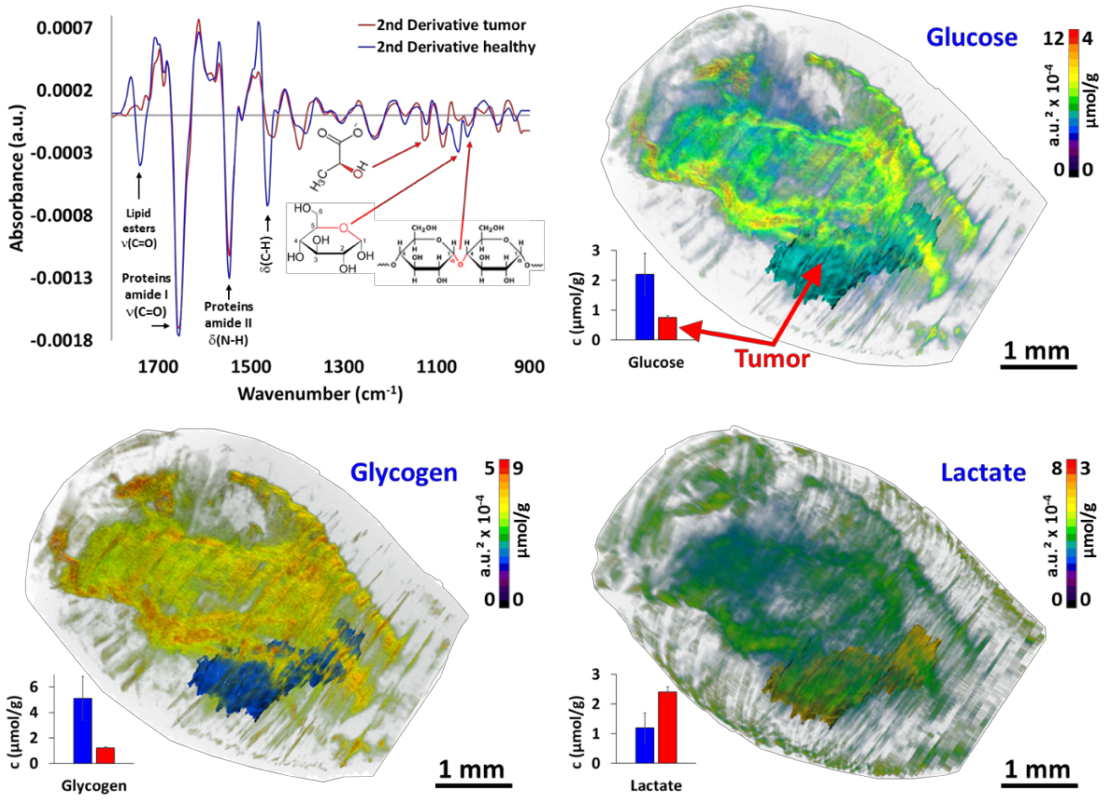

Figure 50 Quantitative metabolic analysis of the brain showing the distribution of glucose, lactate and glycogen in a pathological mouse brain.

From the 2nd derivative of the 3D spectrum matrix, the glucose, glycogen and lactate IR absorptions are quantified and mapped for the whole brain. The 3D volume renderings with molecular concentrations have been determined according to the healthy brain (left hemisphere) as a reference. Images are scaled with equivalent absorption (a.u.² .10^{-4}) and concentration (µmol/g) values.

To achieve a quantitative analysis of molecular concentrations by IR spectro-microscopy, our strategy was to use the intensity scales of the glucose, glycogen and lactate IR absorptions from spectra of the left-brain hemisphere.

I first compared the molecular concentrations between enzymatic assays and IR spectra data analyses. A group of 10 mice with similar tumor mass in the right hemisphere were sacrificed to analyze their left hemisphere.

Fluorescence enzymatic essays [201] were made on tissue homogenates and provided a 2.2 ± 0.7 µmol/g of glucose, 4.1 ± 1.7 µmol/g of glycogen, and 1.2 ± 0.5 µmol/g of lactate. These results are consistent with other studies on mice [202, 203, 204] that have been reported from similar enzymatic assays. Interestingly, the regional distributions of glucose [202] in mice brain have been found varying with a 3-fold amplitude, and 2-fold for lactate [205] and glycogen.

Such concentration variations per brain region were also found in our 3D IR images. When we considered the distribution of absorption intensities for glucose, glycogen, and lactate IR absorptions, we observed that 95% of spectra ranged within a 2-3-fold intensity scale values.

Extreme values were rejected from calculations (notably the 0 values, representing 86% of rejected spectra, probably due to noisy signal or to distorted baseline preventing the use of 2nd derivative spectra absorptions).

Spectra included in this study (>95% for each anatomical region) allowed to define a distribution of concentrations in accordance with enzymatic assays performed on brain regions, glucose scale ranging 1.3 to 3.5 µmol/g, glycogen 3.6 to 8.4 µmol/g, and lactate 0.7 to 1.9 µmol/g (basically, each metabolite has a 2.5-fold concentration variation in the brain).

These concentration variations in the mouse brain are thus consistent with previous studies [202], although not fully comparable since microscopic studies of metabolic concentrations in brain have never been done previously on fresh – snap-frozen only - tissues.

It is also important to note that the tumor exhibited a significantly lower glucose (0.8 ± 0.1 μmol/g; $P<0.05$) and glycogen (1.2 ± 0.1 μmol/g; $P<0.05$) concentrations compared to the healthy tissue counterpart in left hemisphere (considering similar locations), while the lactate concentration was much higher (2.4 ± 0.2 μmol/g; $P<0.05$).

With respect to the healthy brain tissues, these metabolic changes in tumor mass are typical of a Warburg effect, where glycolysis is increased and thus depletes the glucose-glycogen stores and consequently raises the production of lactate as a by-product [206]. However, the distributions of metabolic concentrations in the tumor mass were found very homogeneous, which is also characteristic for that size of glioma solid tumor [207].

Importantly, a direct quantitative visualization of brain metabolism could be achieved by 3D-IR imaging, where internal anatomy and quantitative molecular concentrations were revealed through a transparent-based 3D volume rendering.

4.3. Discussion

A classical view of the advantage of 3D pathology over standard 3D histological examinations is that it allows a direct visualization tissue features, particularly those involving structural changes or those in which the spatial relationship of disease features is important. But, this is restrictive since tissues are not only defined by structures; their chemical contents play a major role in the homeostasis of organs, notably within extracellular space.

3D pathology will thus make sense once the anatomical (or sub-structure networks) and chemical features of a tissue block are revealed jointly. However, analyzing the chemical parameters of the tissue (which can be translated as molecular, biochemical, etc. parameters) would require developing a quantitative method for 3D reconstruction and visualization on a common intensity scale.

Until now, the use of 3D pathology has not been routine in research and clinics due to technical difficulties in reconstructing 3D tissue blocks from 2D images of seriated sections. Others have

developed methods for a 3D reconstruction of tissue blocks, but these ones were first stained [109] or used block-face photographic volume registration [110] with MRI to help maintain the shape of very soft tissues, such as brain.

But still, the use of labeling and staining methods or gadolinium injections for MRI prevent further "unaltered" chemical analysis. I thus developed a new methodology to overcome such bottleneck, providing both an image registration and correction method for reconstructing 3D tissue blocks, and achieving to determine molecular concentrations in 3D at microscopic resolution.

The key advantage was the development of a genuine combination of *in vivo* 3D imaging with quantitative spectro-microscopy for producing a 3D quantitative chemical image of a tissue block, here a mouse brain. Our technique requires only a fresh-frozen tissue block to obtain a 3D image made extremely rich of chemical information thanks to the spectral data it contains. And the use of high-resolution X-ray tomograms of the mouse head to reconstruct a brain volume intended to histological analyses from only 3 projections ensured to limit the X-ray dose to the minimum.

Other *in vivo* techniques might be used for obtaining similarly the actual shape of the brain without the use of imaging contrast agents [195], but μCT is well known and accessible to most of modern research laboratories and pathology services. Furthermore, since we are not using either labeling and staining procedures for histology or contrast agents for *in vivo* imaging, the chemical contents of the tissue are not altered [90], which is the mandatory condition to expect further quantitative chemical analyses.

I first demonstrated that the 3D spectrum matrix formed by patched 2D-IR images can be used for many different data extractions from the same dataset. I used the Allen brain atlas as a worldwide recognized reference for the mouse brain anatomy.

Using the full spectral intensity 3D image of the brain, we could segment and mesh many different anatomical regions. It is noteworthy that the full spectral intensity images of the brain were already delineating many different brain regions comparable to what is usually observed from coloration of IHC images (hippocampus, cerebral cortex, hippocampal regions, cerebellum lobules, hypothalamus and thalamus, etc.).

I separated the right (with tumor) and left (healthy) hemispheres to segment anatomical regions only based on spectral data and that was perfectly matching the reference atlases for the mouse brain. The 3D spectrum matrix of the tumor could be also extracted and its chemical contents analyzed separately.

It is therefore possible to separate tissue regions, analyze their chemical content variations, changes induced by borders or interface between anatomical regions, compare healthy and pathological specimens, and many more.

The second major objective of this methodology development for 3D pathology was to extract and reconstruct quantitative chemical information from relevant tissue parameters. To date, quantitative histology has remained limited to the quantitation of objects [208] and sub-structures [209] in tissue sections, but not to its chemical contents [87]. I demonstrated that a 3D quantitative chemical image provided by IR spectro-microscopy is able to solve one of the most limiting aspect of conventional histological methods: the lack of quantitative analysis of molecular contents in tissues.

I focused on tissue metabolic parameters which regulation is deeply altered by growing tumors [194, 200], such as gliomas. I first calibrated the absorption values for glucose, glycogen, and lactate using their 2^{nd} derivative spectra with respect to biochemical assays performed on brain homogenates obtained in parallel.

I used well-known procedures for extraction of IR absorptions [193, 2] that we could translate as concentrations [210]. The variations in metabolic molecule absorptions are consistent with the literature [188], where a 2-3-fold concentration change can be observed for these metabolic parameters between regions. The brain regions exhibit important glucose concentrations changes [202].

Therefore, we used the meshed anatomical regions of the brain as previously defined to determine their glucose, glycogen, and lactate concentration variations. Our results were found very similar to the few other studies available, i.e., which analyzed brain tissue areas separately (by microdissection [201, 202, 205]) and used quantitative methods (enzymatic assays).

Interestingly, the tumor volume exhibited more homogeneous metabolic concentrations, but with glucose and glycogen 60-70% lower and lactate 110% higher than the brain healthy tissues

counterpart. This example of quantitative anatomo-metabolic analysis shows the potential of the method for 3D pathology in general.

I have thus combined an efficient anatomical rendering of the mouse brain with a quantitative chemical analysis of its contents from the same dataset. The 3D volume renderings for anatomical, chemical and metabolic contents of the mouse brain with a tumor reached an incomparable level of information for a 3D microscopy analysis.

It was also shown that co-registration between *in vivo* and histological analyses could be enriched by existing anatomical atlases. The quantitative volume rendering with transparency allows a direct 3D visualization of internal anatomy of the brain with concurrent quantitative analysis of its molecular concentrations.

This new methodology opens a new era for histology since two major features can be developed now: the 3D study of tissues/organs and their quantitative chemical analysis for an infinite range of possibilities, as much as chemical information can be produced from IR spectral data to create relevant metadata.

I can assert that this methodology is the first realistic candidate for the development of 3D pathology as a routine for biomedical research, and possibly also for clinical applications. Indeed, all the steps of the image acquisition and data treatments can be automated for a standardized output of results.

Thanks to the chemical information that IR spectroscopy provides, it will be feasible to extract many different features of a tissue block, such as the blood vessel network [26], its biochemistry, its metabolism, for instance. The development of sophisticated spectral data treatments will allow defining the chemical (spectral) profile of these tissue features for 3D reconstruction at microscopic resolution.
As we demonstrated for anatomical and metabolic features of a mouse brain, the exploitation of the whole spectral information, called ‘spectromics’, from a tissue block will expand tremendously the possible applications of this methodology. This is also opening the way to multimodal data treatments, where machine learning algorithms will be able to cross-correlate events from different sources: anatomical, metabolic and biochemical, with omics to improve my knowledge in health and disease.

CHAPTER 5: 3D Anatomo-Chemistry of mouse brain

In this chapter, we introduce a broader application of our methodology in the reconstruction of the anatomy of mouse brain. I propose the use of IR imaging to reconstruct the anatomy of the mouse brain based on the chemical composition of different anatomical regions.

As demonstrated in the previous chapter, our methods can be used to resolve anatomical structures in mouse brains based on their chemical profile. However, resolving the whole anatomy of the mouse brain comes with a lot of complexity due to subtler chemical variations between anatomical regions, thus leading to more accurate internal segmentation, which in turn requires more accurate corrections of anatomical modifications induced by organ extraction from skull, sectioning/deposit procedures, and signal intensity normalization over the 3D spectrum matrix.

While resolving a full anatomical atlas of the mouse brain based on the chemical profiles of different anatomical region is feasible, however, it was out of the scope of this study due to the constraint of time. It remains an elusive task due to the complexity of resolving to precision every subtle difference in chemical profile identified, thus leading to more accurate internal segmentation, which in turn requires more accurate corrections of anatomical modifications induced by organ extraction from skull, sectioning/deposit procedures, and signal intensity normalization over the 3D spectrum matrix.

Our willingness was rather to demonstrate that we could analyze a large tissue block at the scale of an organ like the mouse brain. Consequently, we present in this chapter, the results of resolving salient anatomical regions based on their chemical profile.

Figure 51 shows the overview of our experiment. I aim to resolve spectra data to anatomical sections and thereafter reconstruct the whole the anatomical structures in 3D.
Our aim can be summarized as follow:

a. To demonstrate that 3D chemical imaging using IR spectro-microscopy can be used to investigate large tissue blocks.
b. To demonstrate that 3D chemical imaging using IR spectro-microscopy can be used to differentiate anatomical regions in the mouse brain based on their chemical profile.

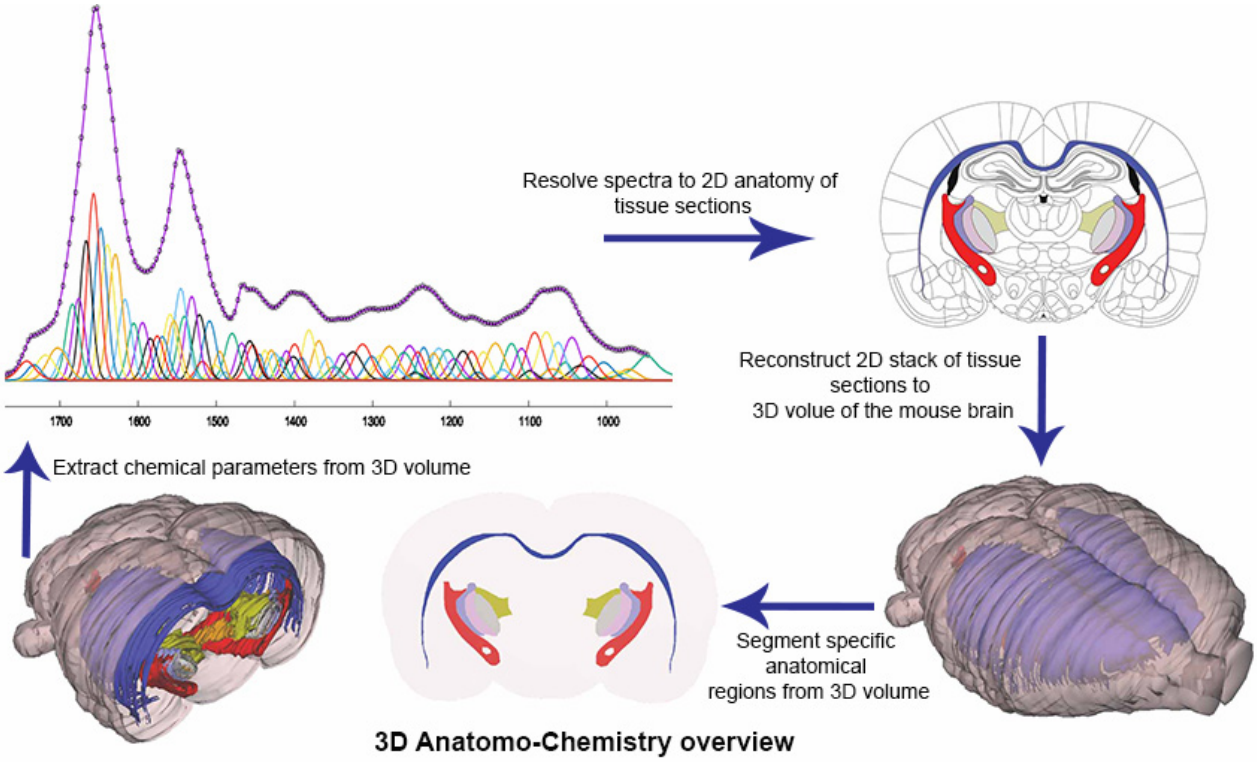

Figure 51 Overview of 3D anatomo-chemistry of mouse brain [111]

Here, we present the methods used in our experiments and thereafter the results and perspectives drawn from our experiments using a healthy mouse brain.

5.1. Methods

Below are the methods used in our experiments from sample preparation to 3D reconstruction of anatomical regions of the mouse brain:

5.1.1. Sample preparations

Full brains were removed from sacrificed mice. The sample holder with brain were inserted in a plastic tube and plunged into liquid N_2 for instant freezing. The frozen brain was deposited in the upright position (with cerebellum on the bottom) on cooled glue (polyvinyl alcohol for cryostat, -20°C) to avoid tissue embedding.

The total duration from the death of animal to the complete freezing of brain was always less than two minutes, which guaranty that degradation in brain cell and tissue contents was limited.

After freezing, additional glue was used to homogenize the sample as a regular block intended for cryosections (Cryostat CM1900, Leica-Microsystems, France). A complete sectioning of the brain was performed at 20-µm thickness. A total of 224 sections was obtained and were deposited on CaF_2 windows.

5.1.2. X-ray image acquisitions

Microradiology was performed with unmonochromatized (white) synchrotron X-rays emitted at the 01-A beamline wavelength shifter of the National Synchrotron Radiation Research Center (NSRRC, Hsinchu, Taiwan). The photon energy ranged from 4 keV to 30 keV with critical energy at ~12 keV; the beam current was kept constant at 360 mA with the top-up operation mode all over acquisition periods.

To obtain 5.59×3.43 mm images X-rays were converted into visible light using a $CdWO_4$ single crystal scintillator and then detecting the photons with an optical microscope equipped with a 1600 × 1200 pixel CCD camera (model 211, Diagnostic Instruments). I reduced the radiation dose by attenuating the X-ray beam with two 550 µm silicon wafers.

The dose was 33.9 Gy per 100 ms for a specimen thickness of 1 cm placed before the sample. The sample-scintillator distance was 5 cm. I used a 2× lens in the optical microscope to obtain the desired field of view; the pixel size in the final image was 2×2 µm².

A simple background flattening image filter was used for large area micro-radiology images. The conceptual details of synchrotron-based microtomography, including absorption and phase contrast, have been discussed in previous study[53].

The high-resolution tomographic images were captured with 360 angles over 180 degrees. The low resolution (and low X-ray dose) images were captured with 3 angles (-90, 0, 90 degrees) and reconstructed using the high-resolution models.

5.1.3. IR acquisitions for 20-µm spatial resolution imaging

I analyzed the mouse brain tissue sections by IR microscopy. The QCL-IR microscope (Spero®, Daylight Solutions, CA, USA) is equipped with 4 IR lasers providing wavelengths every 4 cm^{-1} along the 1800-900 cm^{-1} spectral interval, thus 225 absorption values.

The microscope is constantly purged with dry air and sample compartment is isolated from ambient air by a plastic box. The detector is a non-N_2-liquid frozen focal plane array (FPA) detector with 480x480 elements.
A total of 214 IR images was obtained for the 3D-IR image The microscope was installed in a thermally controlled room (20°C) for standardizing the ambient conditions during acquisitions over the total duration of acquisitions (4 months).

Raw IR image data were stored on server and duplicated for saving a set of 2D-IR images at ~20-µm resolution. The 214 2D-IR images were obtained and represented a matrix of 10.9-million IR spectra and 248 Gb of raw data on a storage server.

5.1.4. IR spectra data treatments

(a) IR image post-processing:

The corrected 2D-IR images were cropped to remove pixels (and thus IR spectra) out of the brain section (containing OCT glue and other features that could bring artefactual data after spectra data treatments, and thus alter the quality of the final 3D images derived from the 3D IR spectrum matrix) and the 3D-IR image was patched as a 3D spectrum matrix of the brain only.

All IR spectra were baseline corrected using a standard procedure (elastic correction based on null absorption at 1800 cm^{-1}). Absorbance spectra were first used to check that spectral intensity scale was consistent between IR images.

(b) Anatomical regions:

As stated in the aim of our experiments, we do not seek to resolve the whole anatomy of the mouse brain. Thus, we chose to resolve large myelinated anatomical regions of the mouse brain. In order to resolve these regions, we performed the segmentation of anatomical regions after a classical spectroscopic analysis, i.e., by calculating the protein-to-lipid absorption ratio $\int$(1700-1480 cm^{-1})/$\int$(1760-1710 cm^{-1}). Due to the high lipid composition of myelin, these regions are well delineated and can thus be extracted by segmentation.

To extract the different salient regions obtained after spectroscopic analysis, we exploit the intensity scale to initially eliminate smaller regions and thereafter perform a topographical analysis to segment

the different regions. For every 2D-IR image, we performed a topographical analysis to identify discrete anatomical structures with the anatomical regions and this is followed by a parameterized shape segmentation procedure in order extract each structure as an independent shape as well as control the minimum size of anatomical structures resolved.

Once an anatomical structure could be highlighted, it was extracted and saved as an independent image for separate analysis. The anatomical structures extracted from each 2D-IR image were systematically compared with each other to establish correlation between similar structures in subsequent structures. When a correspondence is established, the similar structures are assigned the same color for proper visualization.

5.1.5. 3D-IR image reconstruction:

I applied our hierarchical 3D reconstruction method for the 3D reconstruction of the extracted anatomical structures. This procedure is divided into 3 major parts, the global volume correction, global slice corrections and local structures correction.

The $\int(1800\text{-}900\ cm^{-1})$ spectral intensity integration was calculated for all IR spectra and the 3D image was reconstructed (full spectral intensity 3D image of the brain). The full spectral intensity scale typically ranges between 0 and 300, and this scale was applied to all 2D-IR images before 3D reconstruction.

The 3D patch of 2D-IR images was first performed with uncorrected 2D-IR images (Figure 48) to show the mediocre volume rendering induced by the multiple tissue sections shape alterations due to surgery, sample deposition on sample holder, and cryomicrotomy.

To correct the shape aberrations due to surgery, sample deposition on sample holder, and cryomicrotomy, firstly, we performed a slice-slice registration in order to correct global alignment problems. The aligned 2D-IR images were then reconstructed to show that this procedure only solves the global alignment problem that results from cryomicrotomy. However, the problem of relaxation and shape loss due to sample extraction from its micro environment still persists. Thus the need for a global shape correction by X-ray imaging is highlighted.

The X-ray images of the skull were reconstructed into a 3D volume and this is followed by virtually sectioning the X-ray tomogram in order to correct the global shape of each 2D-IR image. The mask of the shape of each 2D-IR image was matched with a virtual section of the x-ray tomogram.

A threshold of 98% correlation was set to ensure the best match is selected for each section. In cases of no appropriate match, the correlation between preceding and subsequent 2D-IR image was computed and the virtual section corresponding to the best correlated image was used.

The mask of each 2D-IR image was subsequently mapped to the corresponding virtual section from the x-ray tomogram. Each 2D-IR image was then fitted into the new mask, thereby adjusting the internal structures proportionately to the difference between the old mask and the new mask.

The same 3D patch was then performed with the corrected 2D-IR images by X-ray imaging allowing to align properly each 2D-IR image and recovering the distorted global shape of the sample due to sample preparation. However, the problem of alignment of anatomical regions and structures is highlighted at this stage due to the innate aberrations from sample preparation and now magnified by the global corrections in the previous step.

Finally, to correct the anatomical structure aberrations, a local correction is performed on each slice while preserving the global shape correction by introducing a constraint with the mask of the global shape. Each anatomical structure was corrected from slice to slice; the structures were corrected for alignment and shape mismatch.

5.2. Results

Below is a step by step presentation of the results of our experiments on a healthy mouse brain for 3D reconstruction of anatomical structures based on their chemical profile.

5.2.1. Acquisition of the actual 3D shape of the brain

I first used mice heads for X-ray tomographic analysis of the brain volume. Heads were analyzed with and without brain inside the skull to obtain the actual brain volume by subtraction of segmented 3D images. The segmentation method we used allowed to obtain the meshing of brain with a 2-µm accuracy.

The high-resolution images were used as models for resizing the low-dose 3-projections X-ray images. The objective was to obtain a 3D image of the brain without altering its contents due to X-rays, and the choice of X-ray microscopy is also to avoid the use of contrast agents or labeling methods (as for MRI), which modify the chemical contents of the tissues.

It would have thus affected the chemical analyses by IR microscopy after histology. The volume rendering from 3 axial absorption projections allowed to obtain a realistic CT shape of the mouse brain that was used to virtualize all tissue sections and create a 2D mask of their planar limits.

The main issue following the acquisition of a brain volume from 3 axial absorption projections was to determine the beginning and ending point of brain sectioning as well as the actual axis of sectioning. This issue was solved by using an available anatomical atlas of the mouse brain, the Allen Developing Mouse Brain Atlas[29].

I resized the atlas with respect to the actual volume of the mouse brain. I used a graph-theoretic slice-to-slice reconstruction with a global histology-to-CT reconstruction to achieve high accuracy, both in the alignment of features between slices and in the 3D shape of the reconstructed brain.

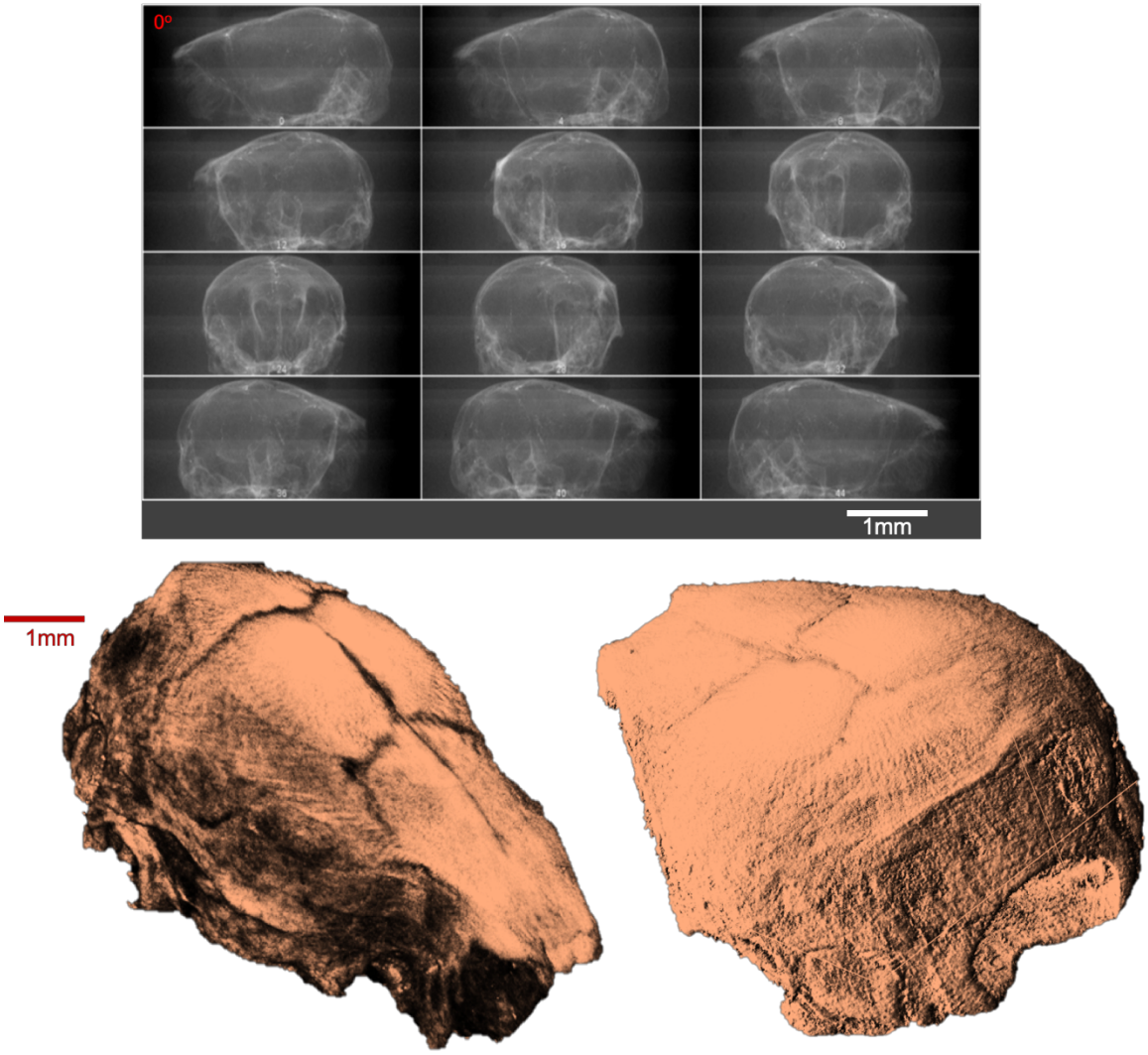

Figure 52 X-ray tomographic reconstruction of the mouse skull from 12 different projections

5.2.2. Acquisition of a 3D IR spectrum matrix of the brain

After acquisition of the three X-ray projections for volume rendering of the brain, the organ was removed from skull and deposited in the upright position (with cerebellum on the bottom) on sample holder for continuous cryomicrotomy at a 20-µm thickness.

An example of 2D IR image of the mouse brain with typical IR spectra from different anatomical regions is shown in Figure 53.

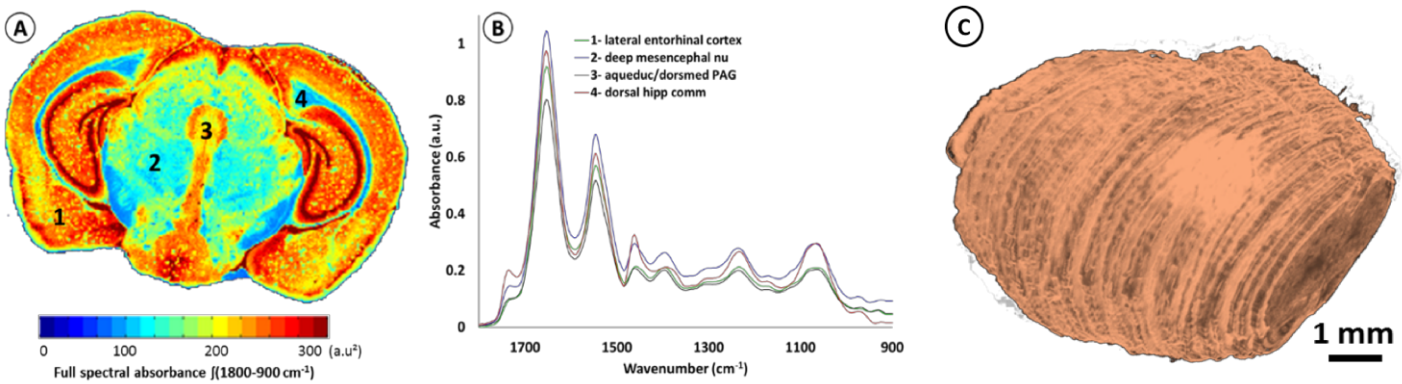

Figure 53 Mouse brain anatomy IR metadata image showing different labelled anatomical regions.

Figure 53 show a 3D-IR image obtained from a mouse brain:

A. The 2D-IR image of the section shown is approximatively located at Bregma -5.04 mm / internaural -0.24 mm. The mouse brain has been sectioned at 20-µm thickness (370 sections). The IR image is shown as a full spectral absorbance (in a.u.²).
B. The IR spectra in corresponding to the 1-4 positions marked in (A) are shown in the central panel. They show important absorbance intensity variations throughout the spectral interval (1800-900 cm^{-1}, also called the fingerprint region). These absorbance intensity variations allow recognizing the major anatomical regions of the mouse brain, which can be used for proper alignment using anatomical atlas of the brain (such as the Allen Developing Mouse Brain Atlas).
C. For the 3D-IR image reconstruction, the full spectral absorbance intensity scale was set free (set at 0 for artefactual pixels in 2D images, <1.5% of pixels for all images) for the 185 raw 2D-IR images obtained from mouse brain sectioning. The 3D patch shows that many tissue shape alterations where present on 2D-IR images.

IR spectra from different regions of the brain show quite different absorption profile, thus confirming that variations of chemical contents are significant. For individual 2D-IR images, the ∫(1800-900 cm^{-1}) intensity scale ranged 0-192 to 0-331 for the whole set of 214 images.

The intensity scale was set free for the 3D-IR image reconstruction. The first reconstruction of the 3D-IR image from 2D raw IR images (without any planar shape correction) was just center-aligned using the central axis between lobes as anatomical reference.

As shown in Figure 48, the general shape of the 3D-IR image of the brain contains numerous distortions. They came from organ shape alterations during surgery (due to the relapse of the brain volume once extracted from the skull, which exerts a pressure on brain tissues, and also due to the gravity-related collapse of this very soft tissue at deposition on the sample holder).

This is also due to the well-known tissue alterations during cryomicrotomy, where tears, bends, cracks, etc. appear at the tissue sectioning or deposition process. This is showing clearly the relevance of using a 3D *in situ* (or *in vivo*) imaging method for obtaining a realistic volume rendering of the mouse brain before histological analyses. This is also a critical to ensure further quantitative chemical analysis from the 3D-IR image.

5.2.3. Anatomical Region Extraction

An important objective of our study was to demonstrate that 3D chemical imaging by IR spectro-microscopy can be used to differentiate different anatomical regions in the mouse brain. However, it was out of the scope of this study due to the constraint of time to extract all the possible anatomical regions and structures in the mouse brain.

To this end, we chose to resolve large myelinated anatomical regions of the mouse brain. In order to resolve these regions, we performed the segmentation of anatomical regions after a classical spectroscopic analysis, i.e., by calculating the protein-to-lipid absorption ratio $\int(1700\text{-}1480\ cm^{-1})/\int(1760\text{-}1710\ cm^{-1})$. Due to the high lipid composition of myelin, these regions are well delineated and can thus be extracted by segmentation.
To extract the anatomical structures, a topological analysis is made in order to determine connected components. Figure 54 shows the extraction of the possible anatomical structures in the 2D IR-Image

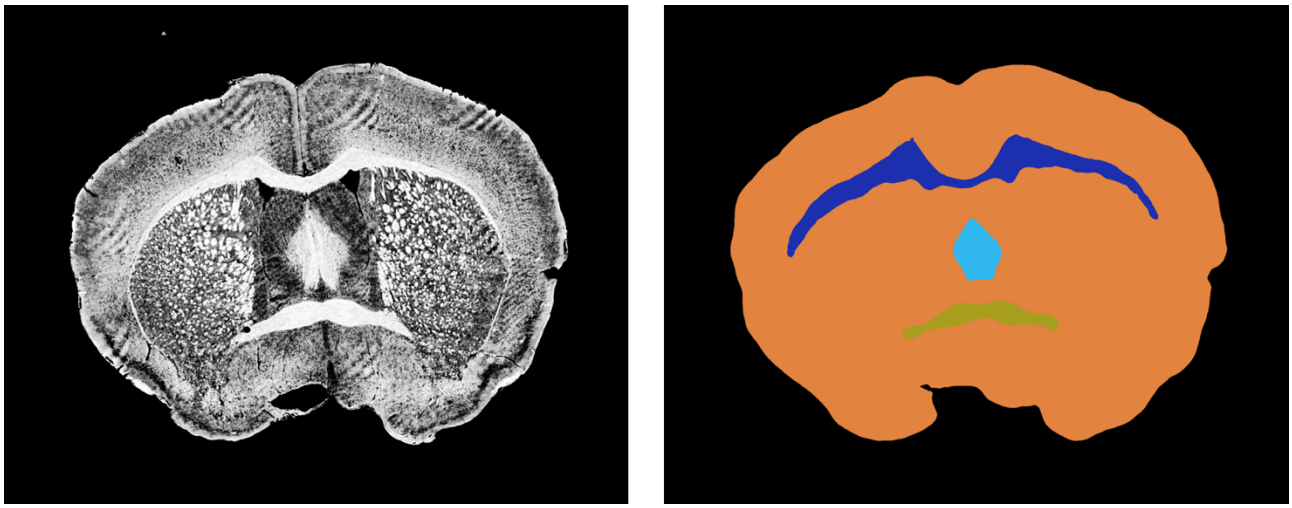

Figure 54 Extraction of anatomical structures from IR metadata image of protein(f(1700-1480 cm^{-1})) to lipid f(1760-1710 cm^{-1}) ratio by topographical analysis.

Once an anatomical structure could be highlighted, it was extracted and saved as an independent image for separate analysis.

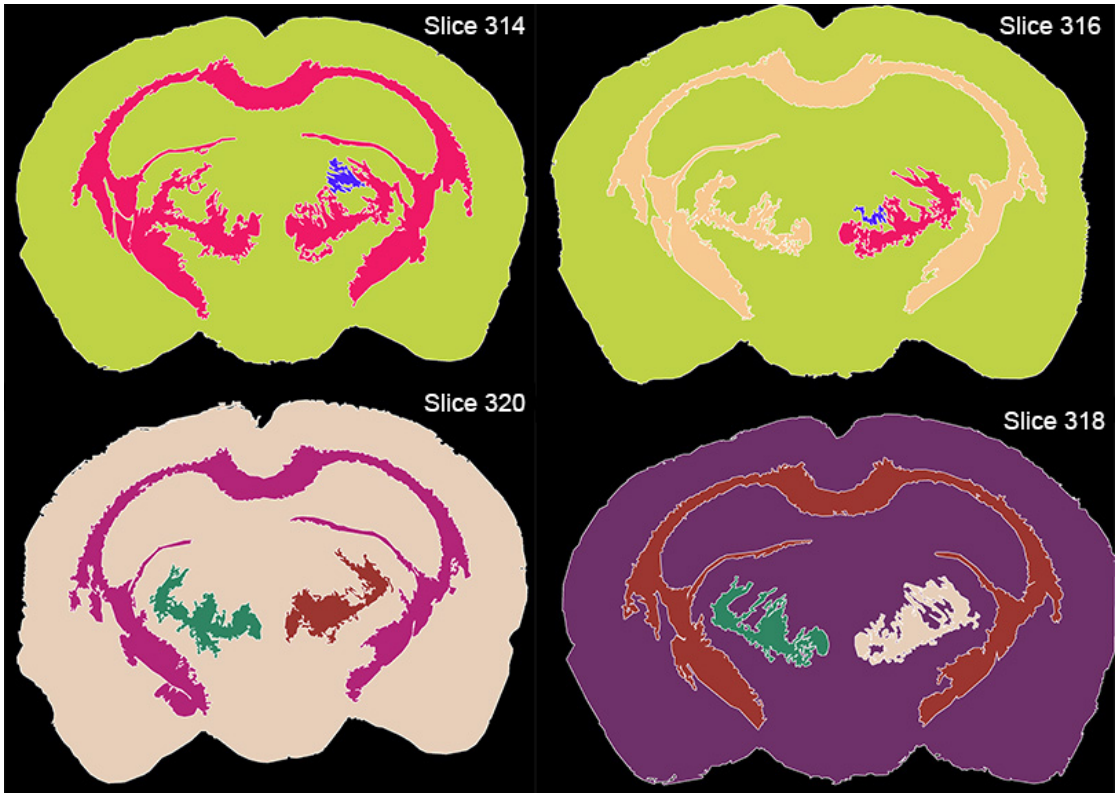

Figure 55 Consistent extraction of different anatomical structures come consecutive slices in the dataset with a color code assigned to each structure..

The anatomical structures extracted from each 2D-IR image were systematically compared with each other to establish correlation between similar structures in subsequent structures. When a

correspondence is established, the similar structures are assigned the same color for proper visualization.

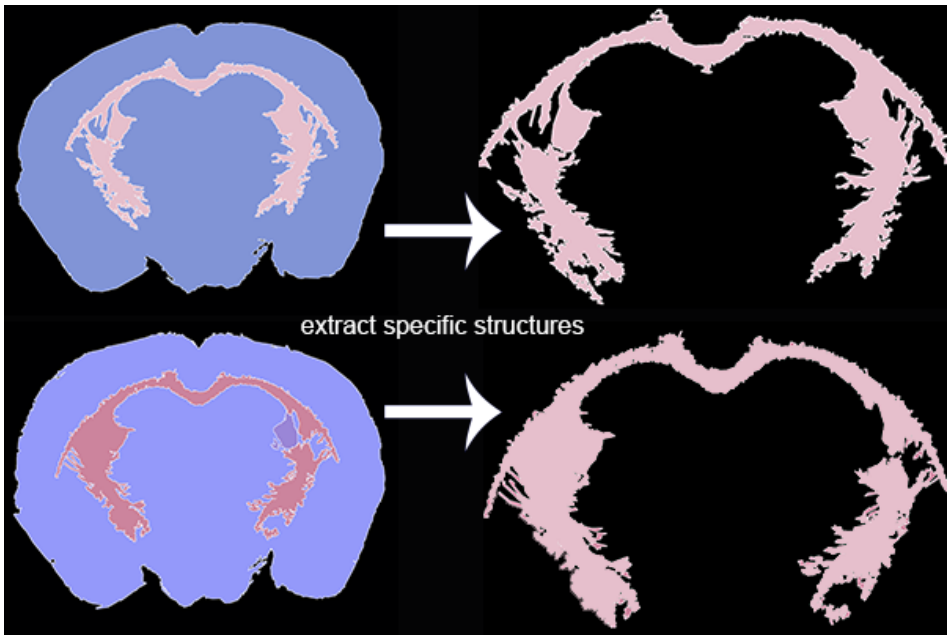

Figure 56 Similar structures extracted to establish correspondence and assign similar color codes for visualization.

5.2.5. 3D-IR image reconstruction:

The ∫(1800-900 cm^{-1}) spectral intensity integration was calculated for all IR spectra and the 3D image was reconstructed (full spectral intensity 3D image of the brain). The full spectral intensity scale typically ranges between 0 and 300, and this scale was applied to all 2D-IR images before 3D reconstruction.

The 3D patch of 2D-IR images was first performed with uncorrected 2D-IR images (Figure 57) to show the mediocre volume rendering induced by the multiple tissue sections shape alterations due to surgery, sample deposition on sample holder, and cryomicrotomy.

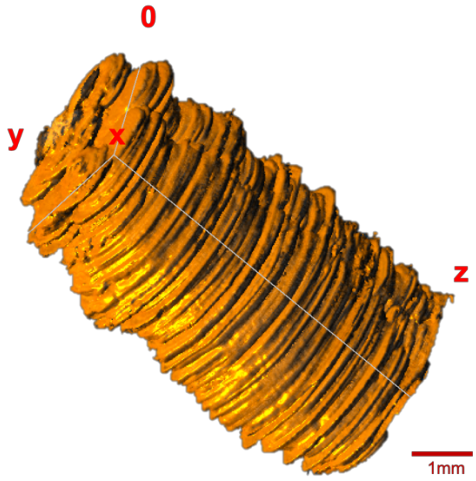

Figure 57 3D reconstruction of unaligned tissue slices.

To correct the shape aberrations due to surgery, sample deposition on sample holder, and cryomicrotomy, firstly, we performed a slice-slice registration in order to correct global alignment problems. The aligned 2D-IR images were then reconstructed to show that this procedure only solves the global alignment problem that results from cryomicrotomy. However, the problem of relaxation and shape loss due to sample extraction from its micro environment still persists. Thus the need for a global shape correction by X-ray imaging is highlighted.

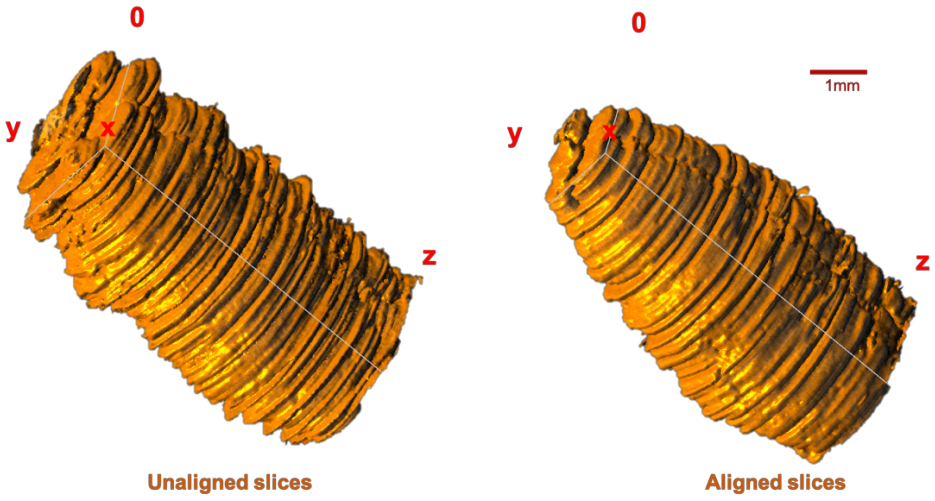

Figure 58 3D reconstruction after global tissue shape alignment

The X-ray images of the skull were reconstructed into a 3D volume and this is followed by virtually sectioning the X-ray tomogram in order to correct the global shape of each 2D-IR image. The mask of the shape of each 2D-IR image was matched with a virtual section of the x-ray tomogram.

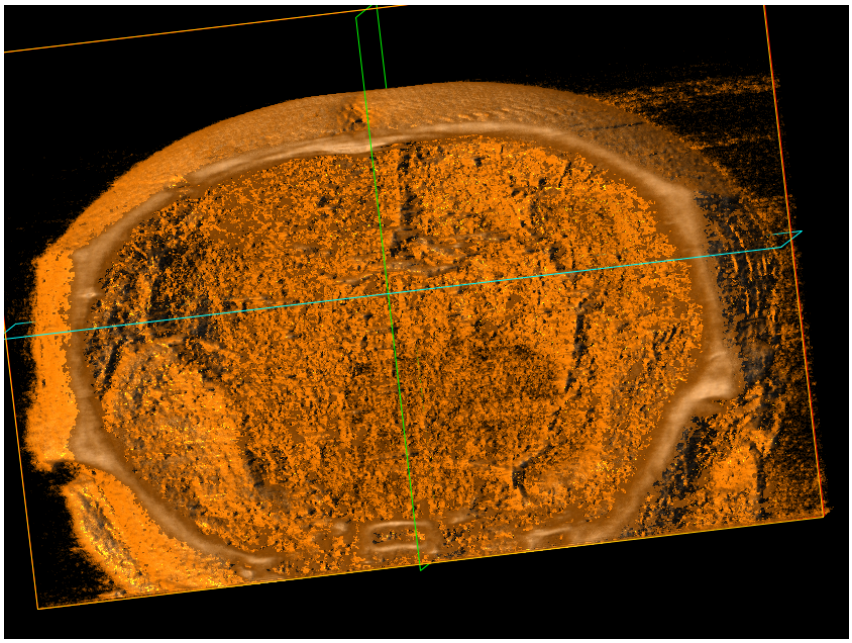

Figure 59 Virtual section from 3D x-ray reference model

A threshold of 98% correlation was set to ensure the best match is selected for each section. In cases of no appropriate match, the correlation between preceding and subsequent 2D-IR image was computed and the virtual section corresponding to the best correlated image was used.

The mask of each 2D-IR image was subsequently mapped to the corresponding virtual section from the x-ray tomogram. Each 2D-IR image was then fitted into the new mask, thereby adjusting the internal structures proportionately to the difference between the old mask and the new mask.

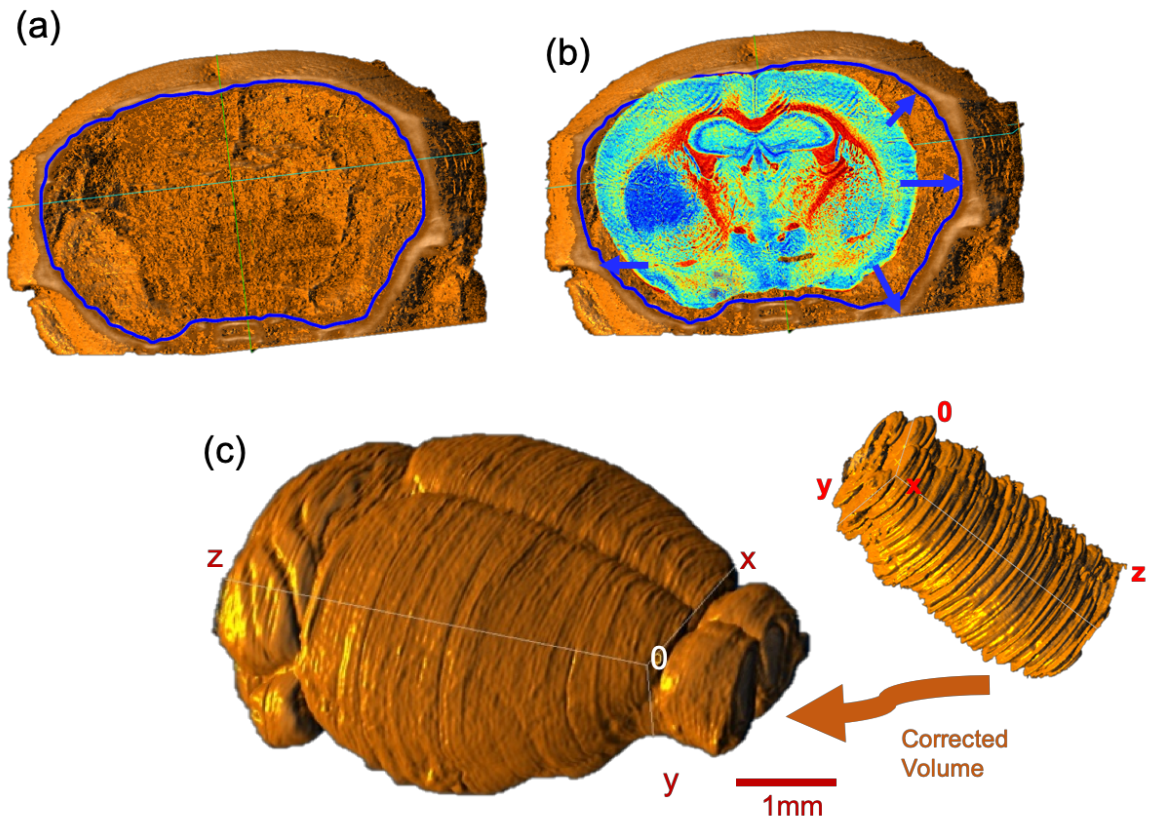

Figure 60 Global shape correction using x-ray model. (a) Mask of virtual section from x-ray model. (b) IR metadata image mapped and deformed to fit virtual section mask. (c) Reconstructed volume after correction using x-ray model.

The same 3D patch was then performed with the corrected 2D-IR images by X-ray imaging allowing to align properly each 2D-IR image and recovering the distorted global shape of the sample due to sample preparation. However, the problem of alignment of anatomical regions and structures is highlighted at this stage due to the innate aberrations from sample preparation and now magnified by the global corrections in the previous step.

Finally, to correct the anatomical structure aberrations, a local correction is performed on each slice while preserving the global shape correction by introducing a constraint with the mask of the global shape. Each anatomical structure was corrected from slice to slice; the structures were corrected for alignment and shape mismatch.

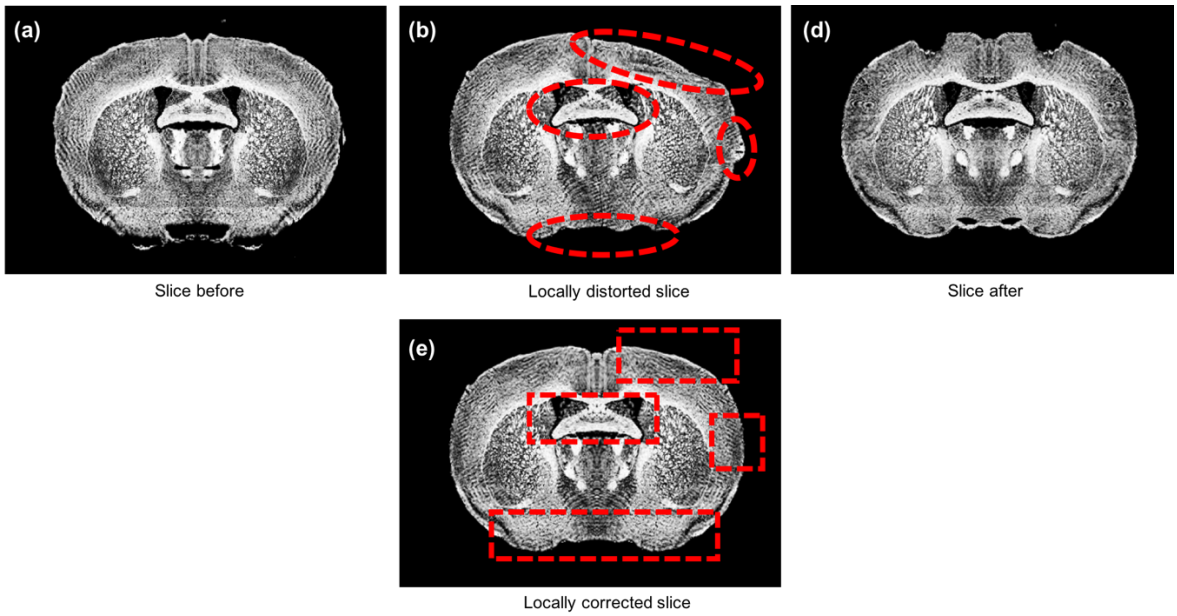

Figure 61 Local aberration correction showing the correction of some local shape distortion on the tissue slice in (b). (a) and (c) are reference slices used for the correction of (c).

To reconstruct specific anatomical structures, we perform segmentation on the global shape and local aberrations corrected IR metadata images. Segmentation is performed using a topological analysis segmentation. The tissue slices are segmented into different shapes based on the variations of absorption intensity.

Similar structures are then matched to assign the same color code for visualization before stacking into a 3D volume. Figure 62 shows an example of extracting and reconstructing the corpus callosum and the basal ganglia region of the mouse brain.

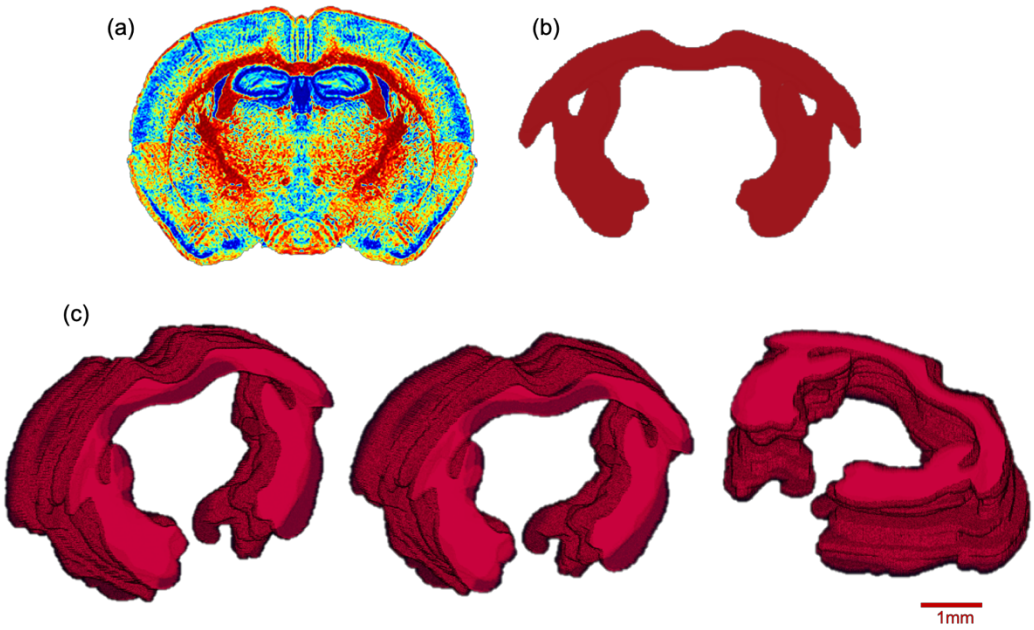

Figure 62 3D Reconstruction of the corpus callosum and basal ganglia region of mouse brain. (a) IR metadata image of the protein to lipid absorption ratio ∫(1700-1480 cm^{-1})/∫(1760-1710 cm^{-1}). (b) Segmentation of the corpus callosum and basal ganglia based on the topological analysis of tissue slices. (c) Different views of the 3D reconstructed corpus callosum and the basal ganglia region of the mouse brain.

5.3. Discussion

3D histology is a powerful approach for imaging biological specimens is the next frontier for modern histopathology. 3D histology offers a significant advantage over 2D because tissue blocks are not naturally transparent, and they contain complex 3D networks (blood and lymph systems, membranes, nerves and other fibers, etc.), a 3D arrangement of different cell phenotypes that is not homogeneous, and an extracellular space that is composed of many other compounds and filamentous structures. From a geometric point of view, it is possible in principle to instantly visualize tissue abnormalities using 3D histology.

3D anatomo-chemistry as the name implies aims to combine the study of the anatomy of bio samples in relation to their chemical compositions. Until now, the anatomy and quantitative chemical composition of biological samples have been studied independently. To the best of my knowledge, this is because there is no in-vivo imaging method able to resolve the anatomy and quantitative chemical composition of biological samples simultaneously.

3D IR spectro-microscopy offers a unique advantage due to its ability to resolve the anatomy and chemistry of biological samples. The use of a stain-free method such as IR microscopy is essential for 3D anatomo-chemistry as it leave the chemistry of the tissues unaltered. The 3D spectrum

matrix provides a molecular 'fingerprint' from spectra that can be used to delineate different anatomical regions.

The key advantage was the development of a genuine combination of *in vivo* 3D imaging with quantitative spectro-microscopy for producing a 3D quantitative chemical image of a tissue block, here a mouse brain. Our technique requires only a fresh-frozen tissue block to obtain a 3D image made extremely rich of chemical information thanks to the spectral data it contains. And the use of high-resolution X-ray tomograms of the mouse head to reconstruct a brain volume intended to histological analyses from only 3 projections ensured to limit the X-ray dose to the minimum.

Other *in vivo* techniques might be used for obtaining similarly the actual shape of the brain without the use of imaging contrast agents, but μCT is well known and accessible to most of modern research laboratories and pathology services. Furthermore, since we are not using either labeling and staining procedures for histology or contrast agents for *in vivo* imaging, the chemical contents of the tissue are not altered[31], which is the mandatory condition to expect further quantitative chemical analyses.

I first demonstrated that the 3D spectrum matrix formed by patched 2D-IR images can be used for many different data extractions from the same dataset. Using the full spectral intensity 3D image of the brain, we could segment and mesh many different anatomical regions.
It is noteworthy that the full spectral intensity images of the brain were already delineating many different brain regions comparable to what is usually observed from coloration of IHC images (hippocampus, cerebral cortex, hippocampal regions, cerebellum lobules, hypothalamus and thalamus, etc.).

The second objective of this methodology was to demonstrate that we can extract anatomical structures of interest from the 3D spectrum matrix formed by 2D-IR images. IR micro-spectroscopy is able to segment tissue block based on their chemical profile. I showed this by extracting myelinated structures from the mouse brain using well-known procedures for extraction of IR absorptions in order to segment the lipid rich myelinated regions of the brain.

As expected, we were able to resolve lipid rich fibre tracts such as the corpus callosum and big anatomical regions of the mouse brain such as the basal ganglia, hippocampus and thalamus. I have also demonstrated that these anatomical structures of interest can be reconstructed in 3D by using a combination of quantitative chemical analysis and in-vivo x-ray imaging.

I showed that we can resolve some of the bottlenecks associated with 3D histology thereby achieving 3D reconstruction similar to the ones obtainable by in-vivo techniques such as MRI. I have thus combined an efficient anatomical rendering of the mouse brain with a quantitative chemical analysis of its contents from the same dataset.

This new methodology opens a new era for histology since two major features can be developed now: the 3D study of tissues/organs and their quantitative chemical analysis for an infinite range of possibilities, as much as chemical information can be produced from IR spectral data to create relevant metadata.

While we were unable to resolve all the possible anatomical structures in the brain due to the constrain of time, this methodology is readily applicable for use in 3D pathology which does not require resolving all the complex anatomy of the brain.

I can assert that this methodology is the first realistic candidate for the development of 3D pathology as a routine for biomedical research, and possibly also for clinical applications. This methodology can be easily adapted to extract any anatomical structure including pathological structures. Indeed, all the steps of the image acquisition and data treatments can be automated for a standardized output of results in clinical applications.

Thanks to the chemical information that IR spectroscopy provides, it will be feasible to extract many different features of a tissue block, such as the blood vessel network[2], its biochemistry, its metabolism, for instance. The development of sophisticated spectral data treatments will allow defining the chemical (spectral) profile of these tissue features for 3D reconstruction at microscopic resolution.

Conclusion and Perspectives.

3D histology offers a powerful approach for imaging biological specimens and is the next frontier for modern histopathology. It offers a significant advantage over 2D because tissue blocks are not naturally transparent, and they contain complex 3D networks (blood and lymph systems, membranes, nerves and other fibers, etc.), a 3D arrangement of different cell phenotypes that is not homogeneous, and an extracellular space that is composed of many other compounds and filamentous structures. From a geometric point of view, it is possible in principle to instantly visualize tissue abnormalities using 3D histology.

A classical application of 3D histology is in the area of pathology where it allows a direct visualization of tissue features, particularly those involving structural changes or those in which the spatial relationship of disease features is important. But, this is restrictive since tissues are not only defined by structures; their chemical contents play a major role in the homeostasis of organs, notably within extracellular space.

3D pathology will thus make sense once the anatomical (or sub-structure networks) and chemical features of a tissue block are revealed jointly. However, analyzing the chemical parameters of the tissue (which can be translated as molecular, biochemical, etc. parameters) would require developing a quantitative method for 3D reconstruction and visualization on a common intensity scale.

Until now, the use of 3D pathology has not been routine in research and clinics due to technical difficulties in reconstructing 3D tissue blocks from 2D images of serial sections. Others have developed methods for a 3D reconstruction of tissue blocks, but these ones were first stained [109] or used block-face photographic volume registration [110] with MRI to help maintain the shape of very soft tissues, such as brain.

Consequently, the use of labeling and staining methods or gadolinium injections for MRI prevent further “unaltered” chemical analysis. These conventional methods are also ‘blind’ to the spatially ordered metabolic dynamics within tissues. Furthermore, multiple immunostaining cannot identify more than four different antigens on a same sample [26]. Thus, it is important to develop techniques which are able to analyse simultaneously the chemical and anatomical features tissue blocks.

Spectroscopic techniques offer quantitative measurement of tissue contents. Combining a spectrometer and a microscope is in a setup called spectro-microscopy. These setups offer a global view of the sample chemical contents, which can be further analyzed for extracting relevant molecular parameters for diagnosis [27]. 3D chemical imaging is achieved by several spectro-microscopic methods. These provide a quantitative analysis of tissue content and substructures with a depth of information that no other histological technique can determine from the same sample. However, they are currently underexploited despite their potential.

An emerging spectro-microscopic technique for histopathological examination is IR spectro-microscopy. As a result of the advent of powerful IR sources with quantum-cascade lasers (QCLs) in 2014, IR spectro-microscopy can now produce millions of IR spectra per hour with high S/N. This innovation has led to new developments in IR image analyses for biosamples, such as 3D-IR image reconstructions for the quantitative analysis of metabolic or biochemical parameters [27].

3D reconstruction was previously unnecessary in IR spectro-microscopy. Acquisition of a 3D histological dataset was not feasible due to bottlenecks such as inability to maintain consistent S/N and relatively slow acquisition time for large samples. As the new frontier of 3D chemical imaging by IR is just opening up, there is currently no standard processing sequence or specialized algorithms for 3D reconstruction of IR slices. Thus, there is need to develop a standard processing sequence for 3D reconstruction of IR slices.

The objective of this thesis was to develop IR microscopy for 3D pathology and consequently use these methods for 3D chemical imaging of tumors in the brain. However, in order to develop IR microscopy for 3D chemical imaging, we identified the need to develop an advanced processing sequence for 3D chemical imaging by IR microscopy. This is necessary in order to standardize experimental methods in IR data treatment and 3D image reconstruction of tissues for routine use in clinics.

I thus developed a new processing sequence for 3D chemical imaging by IR microscopy. This processing sequence covers the process of sample preparation, data acquisition of tissue samples, IR data treatment methods, metadata extraction methods and the 3D reconstruction of tissue slices. Our proposed 3D reconstruction technique was a combination of *in vivo* 3D imaging with quantitative spectro-microscopy.

The key advantage of this approach was the development of a genuine combination of *in vivo* 3D imaging with quantitative spectro-microscopy for producing a 3D quantitative chemical image of a tissue block, here a mouse brain. Our technique requires only a fresh-frozen tissue block to obtain a 3D image made extremely rich of chemical information thanks to the spectral data it contains. And the use of high-resolution X-ray tomograms of the mouse head to reconstruct a brain volume intended to histological analyses from only 3 projections ensured to limit the X-ray dose to the minimum.

Other *in vivo* techniques might be used for obtaining similarly the actual shape of the brain without the use of imaging contrast agents [16], but μCT is well known and accessible to most of modern research laboratories and pathology services. Furthermore, since we are not using either labeling and staining procedures for histology or contrast agents for *in vivo* imaging, the chemical contents of the tissue are not altered [87], which is the mandatory condition to expect further quantitative chemical analyses.

Consequently, we first demonstrated that the 3D spectrum matrix formed by patched 2D-IR images can be used for many different data extractions from the same dataset. I used the Allen brain atlas as a worldwide recognized reference for the mouse brain anatomy.

Using the full spectral intensity 3D image of the brain, we could segment and mesh many different anatomical regions. It is noteworthy that the full spectral intensity images of the brain were already delineating many different brain regions comparable to what is usually observed from coloration of IHC images (hippocampus, cerebral cortex, hippocampal regions, cerebellum lobules, hypothalamus and thalamus, etc.).

I separated the right (with tumor) and left (healthy) hemispheres to segment anatomical regions only based on spectral data and that was perfectly matching the reference atlases for the mouse brain. The 3D spectrum matrix of the tumor could be also extracted and its chemical contents analyzed separately.

It is therefore possible to separate tissue regions, analyze their chemical content variations, changes induced by borders or interface between anatomical regions, compare healthy and pathological specimens, and many more.

In addition, we demonstrate that we can extract and reconstruct quantitative chemical information from relevant tissue parameters. To date, quantitative histology has remained limited to the quantitation of objects [208] and sub-structures [209] in tissue sections, but not to its chemical contents [90]. I demonstrated that a 3D quantitative chemical image provided by IR spectro-microscopy is able to solve one of the most limiting aspect of conventional histological methods: the lack of quantitative analysis of molecular contents in tissues.

I focused on tissue metabolic parameters which regulation is deeply altered by growing tumors [194, 200], such as gliomas. I first calibrated the absorption values for glucose, glycogen, and lactate using their 2nd derivative spectra with respect to biochemical assays performed on brain homogenates obtained in parallel.

I used well-known procedures for extraction of IR absorptions [193, 2] that we could translate as concentrations [210]. The variations in metabolic molecule absorptions are consistent with the literature [188], where a 2-3-fold concentration change can be observed for these metabolic parameters between regions. The brain regions exhibit important glucose concentrations changes [202].

Therefore, we used the meshed anatomical regions of the brain as previously defined to determine their glucose, glycogen, and lactate concentration variations. Our results were found very similar to the few other studies available, i.e., which analyzed brain tissue areas separately (by microdissection [201, 202, 205]) and used quantitative methods (enzymatic assays).

I showed that the tumor volume exhibited more homogeneous metabolic concentrations, but with glucose and glycogen 60-70% lower and lactate 110% higher than the brain healthy tissues counterpart. This example of quantitative anatomo-metabolic analysis shows the potential of the method for 3D pathology in general while also assessing the well-studied Warburg effect in tumors.

I have thus combined an efficient anatomical rendering of the mouse brain with a quantitative chemical analysis of its contents from the same dataset. The 3D volume renderings for anatomical, chemical and metabolic contents of the mouse brain with a tumor reached an incomparable level of information for a 3D microscopy analysis.

It was also shown that co-registration between *in vivo* and histological analyses could be enriched by existing anatomical atlases. The quantitative volume rendering with transparency allows a direct 3D visualization of internal anatomy of the brain with concurrent quantitative analysis of its molecular concentrations.

Finally, we showed that our methodology can be extended beyond tumors to analyse the anatomy of the mouse brain. I attempted to develop what we called the 3D-anatomo chemistry of the brain. 3D anatomo-chemistry as the name implies aims to combine the study of the anatomy of bio samples in relation to their chemical compositions.

Until now, the anatomy and quantitative chemical composition of biological samples have been studied independently. To the best of my knowledge, this is because there is no in-vivo imaging method able to resolve the anatomy and quantitative chemical composition of biological samples simultaneously.

I demonstrated that we can extract anatomical structures of interest from the 3D spectrum matrix formed by 2D-IR images. IR microscopy is able to segment tissue block based on their chemical profile. I showed this by extracting myelinated structures from the mouse brain using well-known procedures for extraction of IR absorptions in order to segment the lipid rich myelinated regions of the brain.

As expected, we were able to resolve lipid rich fibre tracts such as the corpus callosum and big anatomical regions of the mouse brain such as the basal ganglia, hippocampus and thalamus. I also demonstrated that these anatomical structures of interest can be reconstructed in 3D by using a combination of quantitative chemical analysis and in-vivo x-ray imaging.

I showed that we can resolve some of the bottlenecks associated with 3D histology thereby achieving 3D reconstruction similar to the ones obtainable by in-vivo techniques such as MRI. I have thus combined an efficient anatomical rendering of the mouse brain with a quantitative chemical analysis of its contents from the same dataset.

While we were unable to resolve all the possible anatomical structures in the brain due to the constrain of time, this methodology is readily applicable for use in 3D pathology which does not require resolving all the complex anatomy of the brain.

As we demonstrated for anatomical and metabolic features of a mouse brain, the exploitation of the whole spectral information, called ‘spectromics’, from a tissue block will expand tremendously the possible applications of this methodology. This is also opening the way to multimodal data treatments, where machine learning algorithms will be able to cross-correlate events from different sources: anatomical, metabolic and biochemical, with omics – to improve my knowledge in health and disease.

This new methodology opens a new era for histology since two major features can be developed now: the 3D study of tissues/organs and their quantitative chemical analysis for an infinite range of possibilities, as much as chemical information can be produced from IR spectral data to create relevant metadata.

I can assert that this methodology is the first realistic candidate for the development of 3D pathology as a routine for biomedical research, and possibly also for clinical applications. Indeed, all the steps of the image acquisition and data treatments can be automated for a standardized output of results.

Thanks to the chemical information that IR spectroscopy provides, it will be feasible to extract many different features of a tissue block, such as the blood vessel network [26], its biochemistry, its metabolism, for instance. The development of sophisticated spectral data treatments will allow defining the chemical (spectral) profile of these tissue features for 3D reconstruction at microscopic resolution.

APPENDIX

Harris corner detection

Corners are regions in the image with large variation in intensity in all the directions. The Harris corner detector method was proposed to find whether a point shows significant change in all direction or not [151]. If yes, then point is marked as a corner point.

Harris corner detector is based on the auto correlation function of the intensities. It basically finds the difference in intensity for a displacement of $(\Delta x, \Delta y)$ in all directions. This is expressed as below:

$$E(x,y) = \sum_{x,y} \underbrace{w(x,y)}_{window\ function} . \left[\underbrace{I(x+\Delta x, y+\Delta y)}_{shifted\ intensity} - \underbrace{I(x,y)}_{intensity} \right]^2$$

The window function is either a rectangular window or Gaussian window which assigns weights to pixels underneath.

By the definition of corners, in approximate the intensity variation in a given window, the local maxima of the function $E(u,v)$ can be approximated. This can be done by applying Taylor expansion as follow:

Let I_x and I_y be the partial derivatives of I, such that;

$$I(x+\Delta x, y+\Delta y) \approx I(x,y) + I_x(x,y)\Delta x + I_y(x,y)\Delta y$$

Thus, $E(x,y)$ can be approximated as:

$$E(x,y) \approx \sum_{x,y} w(x,y).(I_x(x,y)\Delta x + I_y(x,y)\Delta y)^2$$

This can be rewritten in matrix form as:

$$E(x,y) = [\Delta x \quad \Delta y] M \begin{bmatrix} \Delta x \\ \Delta y \end{bmatrix}$$

Where

$$M = w(x,y)\begin{bmatrix} I_x I_x & I_x I_y \\ I_x I_y & I_y I_y \end{bmatrix}$$

A Harris response function is then computed to determine if the point (x, y) is a corner or not. The Harris response function is defined as:

$$R = \det(M) - k\big(trace(M)\big)^2 = \lambda_1\lambda_2 - k(\lambda_1 + \lambda_2)^2$$

where k is an empirically determined constant; $k \in [0.04,0.06]$,
λ_1 *and* λ_2 are the eigen values of M

When $|R|$ is small, which happens when λ_1 and λ_2 are small, the region is considered flat.
When $R < 0$, which happens when $\lambda_1 \gg \lambda_2$ or vice versa, the region is considered an edge.
When R large, which happens when λ_1 and λ_2 are large and $\lambda_1 \sim \lambda_2$, the region is considered a corner.
The Harris corner detector is invariant to translation, rotation and illumination change [152]. This detector is most repetitive and most informative. The disadvantage of this detector is it is not invariant to large scale change [153].

Scale invariant feature transform (SIFT)

Scale invariance is an important factor in ensuring the reliability of extracted features in a series of 2D histological slices. It is important that the features extracted can be detectable even under changes in image scale, noise and illumination. The deformation of tissue slices after histological sectioning contributes to the change of scale of salient features in successive tissue slices.

The SIFT method is robust and invariant to scaling, orientation, illumination changes, and partially invariant to affine distortion. This is achieved by decomposing images into multiple resolutions and performing the registration from low resolutions to high resolutions, hierarchal registration speed, avoid local minima, and therefore improve registration performance [154].

A SIFT key-point as shown in (figure) is a circular image region with an orientation. It is described by a geometric frame of four parameters: the key-point center coordinates x and y, its scale (the radius of the region), and its orientation (an angle expressed in radians) [155].

There are four main steps in SIFT feature extraction:

Scale-Space Extrema Detection

The first stage of key-point detection is to identify locations and scales that can be assigned under differing views of the same object. Detecting locations that are invariant to scale change of the image can be accomplished by searching for stable features across all possible scales, using a continuous function of scale known as scale space [211]. It has been shown that under a variety of reasonable assumptions the only possible scale-space kernel is the Gaussian function [212, 213].

Therefore, the scale space of an image is defined as a function, $L(x\ , y, \sigma)$, that is produced from the convolution of a variable-scale Gaussian, $G(x\ , y, \sigma)$, with an input image, $I(x\ , y)$:

$$L(x\ , y, \sigma) = \ G(x\ , y, \sigma) * \ I(x, y)$$

where $*$ is the convolution operation in x and y,

$$G(x\ , y, \sigma) = \frac{1}{2\pi\sigma^2} e^{-(x^2+y^2)/\sigma^2}$$

To efficiently detect stable key-point locations in scale space, Lowe [156] proposed using scale-space extrema in the difference-of-Gaussian function convolved with the image, $G(x\ , y, \sigma)$ which can be computed from the difference of two nearby scales separated by a constant multiplicative factor k: This scale space extrema is computed from the expression:

$$D(x\ , y, \sigma) = (G(x\ , y, k\sigma) - \ G(x\ , y, \sigma)) * \ I(x, y)$$

$$D(x\ , y, \sigma) = L(x\ , y, k\sigma) - \ L(x\ , y, \sigma)$$

It is a particularly efficient function to compute the smoothed images L in any case for scale space feature description. And D can therefore be computed by simple image subtraction. As shown in Fig. 2* for each octave (eight pixel area?) of scale space, the initial image is repeatedly convolved with Gaussians to produce the set of scale space images shown on the left. Adjacent Gaussian images are subtracted to produce the difference-of-Gaussian images on the right. After each octave, the Gaussian image is down-sampled by a factor of 2, and the process repeated.

Keypoint Localization

In order to detect the local maxima and minima of $G(x\ , y, \sigma)$, each sample point is compared to its eight neighbors (pixels) in the current image and nine neighbors in the scale above and below (Fig. 5). It is selected only if it is larger than all of these neighbors or smaller than all of them. The

images shown in the Fig. 5 are detected by comparing a pixel (marked with X) to its 26 neighbors in 3 × 3 regions at the current and adjacent scales (marked with circles). Once a key-point candidate has been found by comparing a pixel to its neighbors, the next step is to perform a detailed fit to the nearby data for location, scale, and ratio of principal curvatures. This information allows points to be rejected that have low contrast (and are therefore sensitive to noise) or are poorly localized along an edge. Fig. 6 shows some of the detected key-points from tested image [212].

Orientation Assignment

By assigning a consistent orientation to each key-point based on local image properties, the key-point descriptor can be represented relative to this orientation and therefore achieve invariance to image rotation. This approach contrasts with the orientation invariant descriptors of [1], in which each image property is based on a rotationally invariant measure. The disadvantage of that approach is that it limits the descriptors that can be used and discards image information by not requiring all measures to be based on a consistent rotation.

The scale of the key-point is used to select the Gaussian smoothed image, L, with the closest scale, so that all computations are performed in a scale-invariant manner. For each image sample,$L(x, y)$, at this scale, the gradient magnitude$m(x, y)$, and orientation, $\theta(x, y)$, are computed using pixel differences [156].

Feature Description

To generate a vector that describes a SIFT key-point, orientation histograms are created over 4x4 sample regions. The figure shows 8 directions for each orientation histogram with the length of each arrow corresponding to the magnitude of that histogram entry [214]. A gradient sample on the left can shift up to 4 sample positions while still contributing to the same histogram on the right. So, 4×4 array location grid and 8 orientation bins in each sample. That is 128-element dimension of key point descriptor [155].

Speeded up robust features (SURF)

SURF as the name implies, is a speeded-up version of SIFT. In SIFT, Lowe [156] approximated Laplacian of Gaussian (LoG) with Difference of Gaussian for finding scale-space. SURF goes a little further and approximates LoG with Box Filter [157].

SURF is based on multi-scale space theory and the feature detector is based on Hessian matrix and also rely on the determinant of Hessian matrix for both scale-space detection and key-point localization.

Since Hessian matrix has good performance and accuracy. In image I, $X = (x, y)$ is the given point, the Hessian matrix $H(X, \sigma)$ in X at scale σ, it can be define as:

$$H(X, \sigma) = \begin{bmatrix} L_{xx}(X, \sigma) & L_{xy}(X, \sigma) \\ L_{yx}(X, \sigma) & L_{yy}(X, \sigma) \end{bmatrix}$$

Where $L_{xx}(X, \sigma)$ is the convolution result of the second order derivative of Gaussian filter with the image I in point X, and similarly for $L_{xy}(X, \sigma)$ and $L_{yy}(X, \sigma)$.

SURF creates a 'stack' without 2:1 down sampling for higher levels in the pyramid resulting in images of the same resolution. Due to the use of integral images, SURF filters the stack using a box filter approximation of second–order Gaussian partial derivatives as shown in figure (2). Since integral images allow the computation of rectangular box filters in near constant time [158].

Due to the use of box filters and integral images, we do not have to iteratively apply the same filter to the output of a previously filtered layer, but instead can apply box filters of any size at exactly the same speed directly on the original image and even in parallel. Therefore, the scale space is analyzed by up-scaling the filter size rather than iteratively reducing the image size [157].

For orientation assignment, SURF uses the Haar wavelet responses in x and y direction within a circular neighbourhood of radius $6s$ around the interest point, with s the scale at which the interest point was detected. The sampling step is scale dependent and chosen to be s. In keeping with the rest, also the size of the wavelets are scale dependent and set to a side length of $4s$.
Only six operations are needed to compute the response in x or y direction at any scale. Once the wavelet responses are calculated and weighted with a Gaussian ($\sigma = 2s$) centred at the interest

point, the responses are represented as points in a space with the horizontal response strength along the abscissa and the vertical response strength along the ordinate. The dominant orientation is estimated by calculating the sum of all responses within a sliding orientation window of size $\frac{\pi}{3}$, see Fig. 10.

The horizontal and vertical responses within the window are summed. The two summed responses then yield a local orientation vector. The longest such vector over all windows defines the orientation of the interest point. The size of the sliding window is a parameter which had to be chosen carefully. Small sizes fire on single dominating gradients, large sizes tend to yield maxima in vector length that are not outspoken. Both result in a misorientation of the interest point [157].

In order to describe SURF features, the first step consists of constructing a square region centered around the interest point and oriented along the orientation selected in previous section. The size of this window is 20s. Examples of such square regions are illustrated in Fig. 11 [157]. The region is split up regularly into smaller 4x4 square sub-regions. This preserves important spatial information. For each sub-region, the horizontal (d_x) and vertical (d_y)Haar wavelet responses at 5x5 regularly spaced sample points is computed.

Then, the wavelet responses d_x and d_y are summed up over each sub-region and form a first set of entries in the feature vector. In order to bring in information about the polarity of the intensity changes, the sum of the absolute values of the responses is also extracted, $|d_x|$ and $|d_y|$. Hence, each sub-region has a 4D descriptor vector v for its underlying intensity structure;

$$v = (\Sigma\, d_x, \Sigma\, d_y, \Sigma\, |d_x|, \Sigma\, |d_y|)$$

Concatenating this for all 4x4 sub-regions, this results in a descriptor vector of length 64. The wavelet responses are invariant to a bias in illumination. Invariance to contrast (a scale factor) is achieved by turning the descriptor into a unit vector.

Feature matching

The problem of feature matching can be formulated as follows, suppose that p is a point detected by a feature detector in an image associated with a descriptor

$$\phi(p) = \{\phi_k(P) | k = 1,2, \dots, K\}$$

where for all K, the feature vector provided by the k-th descriptor is

$$\phi_k(p) = (f_{1_p}^{k}, f_{2_p}^{k}, \dots, f_{n_{kp}}^{k})$$

The aim is to find the best correspondence q in another image from the set of N interest points $Q = \{q_1, q_2, \dots, q_N\}$ by comparing the feature vector $\phi_k(p)$ with those of the points in the set Q. To this

end, a distance measure between the two interest points descriptors $\phi_k(p)$ and $\phi_k(q)$ can be defined as

$$d_k(p,q) = |\phi_k(p) - \phi_k(q)|$$

A match between the pair of interest points (p, q) is accepted only if p is the best match for q in relation to all the other points in the first image and q is the best match for p in relation to all the other points in the second image. In this context, it is very important to devise an efficient algorithm to perform this matching process as quickly as possible. The nearest-neighbor matching in the feature space of the image descriptors in Euclidean norm can be used for matching vector based features [159].

Optical flow method

The notion of optical flow literally refers to the displacements of intensity patterns. This definition originates from a physiological description of the visual perception of the world through image formation on the retina. In that sense, while optical flow is necessarily caused by relative motion between the observer and the objects of the observed scene, it only represents motion of intensities in the image plane, and not necessarily accounts for the actual 3D motion in the physical scene [161].

Computation of optical flow means computation of two vectors U and V. Vector U represents horizontal velocity of motion and V represents vertical velocity of motion. Usually U and V are computed using the concepts of energy functional. And the main aim is to minimize this energy functional. Energy functional consists of two terms: data term and smoothness term [162].

To determine optical flow, there is need to track some properties of images. Two key problems in optical flow estimation are: 1) Determine what image property to track 2) Determine how to track it [162]. Some features of the images are assumed to stay constant among multiple frames during optical flow estimation. Generally used constancy assumptions are discussed below:

Brightness Constancy Assumption

The most common assumption used in optical flow estimation is the brightness constancy assumption. It states that the gray value of corresponding pixels in the two consecutive frames should be the same.

Assume $I(x, y, t)$ is the center pixel in a n×n neighbourhood and moves by δx, δy in time δt to $I(x + \delta x, y + \delta y, t + \delta t)$. Since $I(x, y, t)$ and $I(x\ +\ \delta x, y\ +\ \delta y, t\ +\ \delta t)$ are the images of the same point (and therefore the same) we have:

$$I(x, y, t)\ =\ I(x\ +\ \delta x, y\ +\ \delta y, t\ +\ \delta t)$$

This can also be extended to 3D applications. Given a small 3D n × n × n block at (x, y, z) at time t moving by $(\delta x, \delta y, \delta z)$ to $(x\ +\ \delta x, y\ +\ \delta y, z\ +\ \delta z)$ over time δt"

$$I(x, y, z, t)\ =\ I(x\ +\ \delta x, y\ +\ \delta y, z\ +\ \delta z, t\ +\ \delta t)$$

Gradient Constancy Assumption

The brightness constancy assumption has one decisive drawback: It is quite susceptible to slight changes in brightness, which often appear in natural scenes. Therefore, it is useful to allow some small variations in the grey value and help to determine the displacement vector by a criterion that is invariant under grey value changes. Such a criterion is the gradient of the image grey value, which can also be assumed not to vary due to the displacement.

I can perform a 1st order Taylor series expansion about $I(x, y, t)$ in the brightness constancy equation to obtain:

$$I(x + \delta x, y +\ \delta y, t\ +\ \delta t) =\ I(x, y, t) + \frac{\partial I}{\partial x}\ \delta x + \frac{\partial I}{\partial y}\ \delta y\ + \frac{\partial I}{\partial t}\ \delta t\ +\ H.O.T.$$

where H.O.T. are the Higher Order Terms, which we assume are small and can safely be ignored. Using the above two equations we obtain:

$\frac{\partial I}{\partial x}\ \delta x + \frac{\partial I}{\partial y}\ \delta y\ + \frac{\partial I}{\partial t}\ \delta t = 0$ or

$\frac{\partial I}{\partial x}\ \frac{\delta x}{\delta t} + \frac{\partial I}{\partial y}\ \frac{\delta y}{\delta t} + \frac{\partial I}{\partial t}\ \underbrace{\frac{\delta t}{\delta t}}_{=1} = 0$ and finally,

$$\frac{\partial I}{\partial x}\ u_x + \frac{\partial I}{\partial y}\ v_y\ + \frac{\partial I}{\partial t} = 0$$

Here $u_x = \frac{\delta x}{\delta t}$ and $v_y = \frac{\delta y}{\delta t}$ are the x and y components of image velocity or optical flow and $\frac{\partial I}{\partial x}$, $\frac{\partial I}{\partial y}$ and $\frac{\partial I}{\partial t}$ are image intensity derivatives at (x, y, t).

These partial derivatives are normally written as:

$I_x = \frac{\partial I}{\partial x}$,$I_y = \frac{\partial I}{\partial y}$ and $I_t = \frac{\partial I}{\partial t}$

Thus, the gradient constancy equation could be rewritten as:

$$I_x u_x + I_y v_y\ + I_t\ = 0$$

The optical flow constraint has one inherent problem: it yields only one constraint to solve for two variables. It is well known that such an under-determined equation system yields an infinite number of solutions. For every fixed u_x a valid v_y can be found fulfilling the constraint. This is as a result of an optical flow problem called the aperture problem.

The aperture problem defines that there is usually insufficient local image intensity structure to measure full image velocity, but sufficient structure to measure the component normal to the local intensity structure.

Smoothness Assumption

The smoothness term stands for the assumption that the neighboring regions belong to the same object and thus these regions have similar depth. The main role of the smoothness term is the redistribution of the computed information and smoothing of depth outliers. In case we get no reliable information from the data term, the smoothness term will realize its smoothing effect by filling in the problem region with data, calculated from neighboring regions.

Résumé

Ce travail a été mené au sein du groupe ‘biophysique’ de plasticité vasculaire de l’unité de recherche de l’angiogenèse et du micro-environnement des tumeurs, l’INSERM U1029 situé à l’Université de Bordeaux. L'objectif principal de cette recherche est de développer une méthodologie d'imagerie 3D pour la caractérisation chimique des tumeurs cérébrales. Il s'agit d'un domaine de recherche sur le cancer qui n'est pas encore développé et qui pourrait devenir très utile pour améliorer l'outil de diagnostic existant pour les tumeurs cérébrales.

L'histologie tridimensionnelle (3D) est un nouvel outil avancé de cancérologie. L'ensemble du profil chimique et des caractéristiques physiologiques d'un tissu est essentiel pour comprendre la logique du développement d'une pathologie. Cependant, il n'existe aucune technique analytique, in vivo ou histologique, capable de découvrir de telles caractéristiques anormales et de fournir une distribution 3D à une résolution microscopique.

Nous présentons ici une méthode unique de microscopie infrarouge (IR) à haut débit combinant une correction d'image automatisée et une analyse ultérieure des données spectrales pour la reconstruction d'image 3D-IR. Nous avons effectué l'analyse spectrale d'un organe complet pour un petit modèle animal, un cerveau de souris avec une tumeur de gliome implantée. L'image 3D-IR est reconstruite à partir de 370 coupes de tissus consécutives et corrigée à l'aide du tomogramme à rayons X de l'organe pour une analyse quantitative précise du contenu chimique. Une matrice 3D de spectres IR 89 x 10^6 est générée, ce qui nous permet de séparer la masse tumorale des tissus cérébraux sains en fonction de divers paramètres anatomiques, chimiques et métaboliques.

Nous démontrons pour la première fois que des paramètres métaboliques quantitatifs (glucose, glycogène et lactate) peuvent être extraits et reconstruits en 3D à partir des spectres IR pour la caractérisation du métabolisme cérébral / tumoral (évaluation de l'effet de Warburg dans les tumeurs). Notre méthode peut être davantage exploitée en recherchant l'ensemble du profil spectral, en distinguant différents points de repère anatomiques dans le cerveau. Nous le démontrons par la reconstruction du corps calleux et de la région des noyaux gris centraux du cerveau.

Dans cette thèse, des méthodes avancées de traitement des données spectrales ont été développées pour la caractérisation des tumeurs cérébrales. Une séquence de traitement avancée est également développée pour la reconstruction quantitative 3D de coupes IR. Une application de nos méthodes

développées est montrée dans une reconstruction 3D quantitative d'une tumeur dans un cerveau de souris basée sur la caractérisation chimique de la tumeur et du métabolisme des tissus normaux. Cette thèse présente également la reconstruction 3D de l'anatomie du cerveau de souris à l'aide de notre séquence de traitement avancée pour la reconstruction quantitative 3D de coupes IR.

Nous avons d'abord démontré que la matrice spectrale 3D constituée d'images 2D-IR patinées peut être utilisée pour de nombreuses extractions de données différentes à partir du même jeu de données. Nous avons utilisé l'atlas du cerveau Allen comme référence mondialement reconnue pour l'anatomie du cerveau de souris.

En utilisant l'intégralité de l'image 3D d'intensité spectrale du cerveau, nous pourrions segmenter et mailler de nombreuses régions anatomiques différentes. Il est à noter que les images d'intensité spectrale complète du cerveau délimitaient déjà de nombreuses régions du cerveau comparables à ce que l'on observe habituellement à partir de la coloration d'images IHC (hippocampe, cortex cérébral, régions de l'hippocampe, lobules de cervelet, hypothalamus et thalamus, etc.).

Nous avons séparé les hémisphères droit (avec la tumeur) et gauche (en bonne santé) pour segmenter les régions anatomiques uniquement sur la base de données spectrales, ce qui correspondait parfaitement aux atlas de référence du cerveau de souris. La matrice spectrale 3D de la tumeur pourrait également être extraite et son contenu chimique analysé séparément.

Il est donc possible de séparer les régions tissulaires, d'analyser leurs variations de contenu chimique, les modifications induites par les frontières ou l'interface entre les régions anatomiques, de comparer des échantillons sains et pathologiques, et bien d'autres.

De plus, nous démontrons que nous pouvons extraire et reconstruire des informations chimiques quantitatives à partir de paramètres tissulaires pertinents. À ce jour, l'histologie quantitative est restée limitée à la quantification d'objets [208] et de sous-structures [209] dans des coupes de tissus, mais pas à son contenu chimique [87]. Nous avons démontré qu'une image chimique quantitative 3D fournie par spectroscopie IR permettait de résoudre l'un des aspects les plus limitants des méthodes histologiques conventionnelles: le manque d'analyse quantitative du contenu moléculaire dans les tissus.

Nous nous sommes concentrés sur les paramètres métaboliques des tissus, dont la régulation est profondément altérée par la croissance des tumeurs [194, 200], tels que les gliomes. Nous avons d'abord calibré les valeurs d'absorption du glucose, du glycogène et du lactate en utilisant leurs spectres de 2ème dérivé par rapport aux essais biochimiques réalisés sur des homogénats de cerveau obtenus en parallèle.

Nous avons utilisé des procédures bien connues d'extraction des absorptions IR [193, 2] que nous pourrions traduire par concentrations [210]. Les variations d'absorption des molécules métaboliques sont conformes à la littérature [188], où un changement de concentration de 2 à 3 fois peut être observé pour ces paramètres métaboliques entre les régions. Les régions du cerveau présentent d'importants changements dans les concentrations de glucose [202].

Par conséquent, nous avons utilisé les régions anatomiques maillées du cerveau telles que définies précédemment pour déterminer leurs variations de concentration en glucose, glycogène et lactate. Nos résultats ont été trouvés très similaires aux quelques autres études disponibles, c.-à-d. Qui analysaient séparément les zones du tissu cérébral (par microdissection [201, 202, 205]) et utilisaient des méthodes quantitatives (dosages enzymatiques).

Nous avons montré que le volume de la tumeur présentait des concentrations métaboliques plus homogènes, mais avec du glucose et du glycogène inférieurs de 60 à 70% et un lactate de 110% supérieur à celui des tissus sains pour le cerveau. Cet exemple d'analyse anatomo-métabolique quantitative montre le potentiel de la méthode pour la pathologie 3D en général tout en évaluant l'effet Warburg bien étudié sur les tumeurs.

Nous avons donc associé un rendu anatomique efficace du cerveau de souris à une analyse chimique quantitative de son contenu à partir du même ensemble de données. Les rendus volumiques 3D de contenus anatomiques, chimiques et métaboliques du cerveau de souris présentant une tumeur ont atteint un niveau d'informations incomparable pour une analyse par microscopie 3D.

Il a également été démontré que le co-enregistrement entre analyses in vivo et analyses histologiques pouvait être enrichi par des atlas anatomiques existants. Le rendu quantitatif en volume avec transparence permet une visualisation 3D directe de l'anatomie interne du cerveau avec une analyse quantitative simultanée de ses concentrations moléculaires.

Enfin, nous avons montré que notre méthodologie pouvait s'étendre au-delà des tumeurs pour analyser l'anatomie du cerveau de souris. Nous avons tenté de développer ce que nous avons appelé la chimie anatomo-3D du cerveau. L'anatomo-chimie 3D comme son nom l'indique vise à combiner l'étude de l'anatomie des échantillons biologiques en relation avec leurs compositions chimiques. Jusqu'à présent, l'anatomie et la composition chimique quantitative d'échantillons biologiques ont été étudiées indépendamment. À notre connaissance, cela est dû au fait qu'il n'existait pas de méthode d'imagerie in vivo capable de résoudre simultanément l'anatomie et la composition chimique quantitative des échantillons biologiques.
Nous avons démontré que nous pouvons extraire des structures anatomiques d'intérêt à partir de la matrice de spectre 3D formée d'images 2D-IR. La microscopie IR permet de segmenter le bloc de tissu en fonction de leur profil chimique. Nous avons montré cela en extrayant des structures myélinisées du cerveau de souris en utilisant des procédures bien connues d'extraction d'absorptions IR afin de segmenter les régions myéliniques riches en lipides du cerveau.

Comme on pouvait s'y attendre, nous avons pu résoudre des faisceaux de fibres riches en lipides tels que le corps calleux et de grandes régions anatomiques du cerveau de souris telles que les noyaux gris centraux, l'hippocampe et le thalamus. Nous avons également démontré que ces structures anatomiques d'intérêt peuvent être reconstruites en 3D en combinant analyse chimique quantitative et imagerie par rayons X in vivo.

Nous avons montré que nous pouvions résoudre certains des goulots d'étranglement associés à l'histologie 3D, réalisant ainsi une reconstruction 3D similaire à celle pouvant être obtenue par des techniques in vivo telles que l'IRM. Nous avons donc associé un rendu anatomique efficace du cerveau de souris à une analyse chimique quantitative de son contenu à partir du même ensemble de données.

Bien que nous n'ayons pas été en mesure de résoudre toutes les structures anatomiques possibles dans le cerveau en raison de la contrainte de temps, cette méthodologie est facilement applicable pour une utilisation en pathologie 3D qui ne nécessite pas de résoudre toute l'anatomie complexe du cerveau.

Comme nous l’avons démontré pour les caractéristiques anatomiques et métaboliques d’un cerveau de souris, l’exploitation de l’ensemble de l’information spectrale, appelée «spectromique», à partir d’un bloc de tissu élargira énormément les applications possibles de cette méthodologie. Cela ouvre également la voie aux traitements de données multimodaux, où les algorithmes d’apprentissage automatique seront capables de mettre en corrélation des événements provenant de différentes sources: anatomique, métabolique et biochimique, avec l’omique - afin d’améliorer nos connaissances en matière de santé et de maladie.

Cette nouvelle méthodologie ouvre une nouvelle ère pour l'histologie dans la mesure où deux caractéristiques principales peuvent maintenant être développées: l'étude 3D des tissus / organes et leur analyse chimique quantitative pour une gamme infinie de possibilités, autant d'informations chimiques pouvant être produites à partir de données spectrales IR créer des métadonnées pertinentes.

Nous pouvons affirmer que cette méthodologie est le premier candidat réaliste au développement de la pathologie 3D en tant que routine pour la recherche biomédicale, et éventuellement aussi pour des applications cliniques. En effet, toutes les étapes de l'acquisition d'images et des traitements de données peuvent être automatisées pour une sortie normalisée des résultats.

Grâce aux informations chimiques fournies par la spectroscopie IR, il sera possible d'extraire de nombreuses caractéristiques différentes d'un bloc tissulaire, telles que le réseau de vaisseaux sanguins2, sa biochimie, son métabolisme, par exemple. Le développement de traitements de données spectrales sophistiqués permettra de définir le profil chimique (spectral) de ces caractéristiques tissulaires pour une reconstruction 3D à une résolution microscopique.

Bibliography

[1] L. C. Garfunkel, J. Kaczorowski and C. Christy, Pediatric Clinical Advisor, Mosby, Inc, 2007.

[2] R. Noreen, M. Moenner, Y. Hwu and C. Petibois, "FTIR spectro-imaging of collagens for characterization and grading of gliomas," *Biotechnology Advances,* no. 30, p. 1432–1446, 30 March 2012.

[3] M. J. Strong, J. Garces, J. C. Vera, M. Mathkour, N. Emerson and M. L. Ware, "Brain Tumors: Epidemiology and Current Trends in Treatment," *Journal of J Brain Tumors & Neurooncology,* vol. 1, no. 1, pp. 1-21, 20 September 2015.

[4] I. Wilhelm, J. Molnár, C. Fazakas, J. Haskó and I. A. Krizbai, "Role of the Blood-Brain Barrier in the Formation of Brain Metastases," vol. 14, no. 1, p. 1383–1411, 11 January 2013.

[5] PDQ Adult Treatment Editorial Board, " PDQ Cancer Information Summaries [Internet]. Adult Central Nervous System Tumors Treatment (PDQ®)," National Cancer Insititue , 2018.

[6] R. Stupp, W. Mason, M. Van den Bent, M. Weller, B. Fisher, M. Taphoorn, K. Belanger, A. Brandes, C. Marosi, U. Bogdahn, J. Curschmann, R. Janzer, S. Ludwin, T. Gorlia, A. Allgeier, D. Lacombe, J. Cairncross, E. Eisenhauer, R. Mirimanoff, E. O. f. R. a. T. o. C. B. T. a. R. Groups and N. C. I. o. C. C. T. Group, "Radiotherapy plus concomitant and adjuvant temozolomide for glioblastoma," *The new England Journal of Medcine,* vol. 352, no. 10, pp. 987-996, 2005.

[7] R. Stupp, M. Hegi, W. Mason, M. Van den Bent, M. Taphoorn, R. Janzer, S. Ludwin, A. Allgeier, B. Fisher, K. Belanger, P. Hau, A. Brandes, J. Gijtenbeek, C. Marosi, C. Vecht, K. Mokhtari, P. Wesseling, S. Villa, E. Eisenhauer, T. Gorlia, M. Weller, D. Lacombe, J. Cairncross, R. Mirimanoff, E. O. f. R. a. T. o. C. B. T. a. R. O. Groups and N. C. I. o. C. C. T. Group, "Effects of radiotherapy with concomitant and adjuvant temozolomide versus radiotherapy alone on survival in glioblastoma in a randomised phase III study: 5-year analysis of the EORTC-NCIC trial.," *The Lancelet. Oncology,* vol. 10, no. 5, pp. 459-466., May 2009.

[8] N. Laperriere, L. Zuraw and G. Cairncross, "Radiotherapy for newly diagnosed malignant glioma in adults: a systematic review," *Radiother Oncol,* vol. 64, no. 3, pp. 259-273, 2002.

[9] N. Bleehen and S. Stenning, "A Medical Research Council trial of two radiotherapy doses in the treatment of grades 3 and 4 astrocytoma. The Medical Research Council Brain Tumour Working Party," *British Journal of Cancer,* vol. 64, no. 4, pp. 769-774, October 1999.

[10] M. Nakamura, F. Roser, J. Michel, C. Jacobs and M. Samii, "The natural history of incidental meningiomas," *Neurosurgery,* vol. 53, no. 1, pp. 62-70, July 2003.

[11] S. Yano, J. Kuratsu and K. B. T. R. Group, "Indications for surgery in patients with asymptomatic meningiomas based on an extensive experience," *Journal of neurosurgery,* vol. 105, no. 4, pp. 538-543, October 2006.

[12] J. Ferlay, I. Soerjomataram, R. Dikshit, S. Eser, C. Mathers, M. Rebelo, D. Parkin, D. Forman and F. Bray, "Cancer incidence and mortality worldwide: sources, methods and major patterns in GLOBOCAN 2012.," *International Journal of Cancer,* vol. 136, no. 5, pp. E359-E386, 2015.

[13] S. Bauer, R. Wiest, L.-P. Nolte and M. Reyes, "A Survey of MRI-based Medical Image Analysis for Brain Tumor Studies," *Physics in medicine and biology,* vol. 58, no. 13, pp. 97-129, July 2013.

[14] M. Castillo, "History and evolution of Brain tumor imaging: Insights through Radiology," *Radiology,* vol. 273, no. 2, pp. S111-125, November 2014.

[15] S. Cha, "Update on Brain Tumor Imaging: From Anatomy to Physiology," *American Journal of Neuroradiology,* vol. 27, no. 3, pp. 475-497, March 2006.

[16] T. Engelhorn, I. Eyupoglu, M. Schwarz, M. Karolczak, H. Bruenner, T. Struffert, W. Kalender and A. Doerfler, "In vivo micro-CT imaging of rat brain glioma: a comparison with 3T MRI and histology," *Neuroscience letters,* vol. 458, no. 1, pp. 28-31, 10 July 2009.

[17] G. Gambarota, W. Leenders, C. Maass, P. Wesseling, B. van der Kogel, O. van Tellingen and A. Heerschap, "Characterisation of tumour vasculature in mouse brain by USPIO contrast-enhanced MRI," *British Journal of Cancer,* vol. 98, no. 11, p. 1784–1789, 3 June 2008.

[18] L. Ludemann, W. Grieger, R. Wurm, P. Wust and C. Zimmer, "Quantitative measurement of leakage volume and permeability in gliomas, meningiomas and brain metastases with dynamic contrast-enhanced MRI," *Journal of Magnetic Resonance Imaging,* vol. 23, no. 1, p. 833–841.

[19] G. S. Young, "Advanced MRI of Adult Brain Tumors," *Neurologic clinics,* vol. 25, no. 2007, p. 947–973, 2007.

[20] M. C. Marc, F. B. J. Ramon and C. Soonmee, "Modern Brain Tumor Imaging," *Braint tumor research and treatment,* vol. 3, no. 1, pp. 8-23, 23 April 2015.

[21] E. V.-M. Javier, C. M. Marc and C. Soonmee, "Current Clinical Brain Tumor Imaging," *Neurosurgery,* vol. 81, no. 3, p. 397–415, 1 September 2017.

[22] D. N. Louis, A. Perry, G. Reifenberger, A. Von Deimling, D. Figarella-Branger, W. K. Cavenee, H. Ohgaki, O. D. Wiestler, P. Kleihues and D. W. Ellison, "The 2016 World Health Organization Classification of Tumors of the Central Nervous System: a summary," *Acta Neuropathologica,* vol. 131, no. 6, pp. 803-820, June 2016.

[23] A. Gonzalez-Segura, J. Manuel Morales, J. Manuel Gonzalez-Darder, R. Cardona-Marsal, C. Lopez-Gines, M. Cerda-Nicolas and D. Monleon, "Magnetic Resonance Microscopy at 14 Tesla and Correlative Histopathology of Human Brain Tumor Tissue," *PLOS One,* vol. 6, no. 11, pp. 1-10, 2011.

[24] C. Petibois, B. Drogat, A. Bikfalvi, G. Deleris and M. Moenner, "Histological mapping of biochemical changes in solid tumors by FT-IR spectral imaging," *Federation of European Biochemical Societies Letters,* vol. 581, no. 1, p. 5469–5474, 2007.

[25] H. A. Alturkistani, F. M. Tashkandi and Z. M. Mohammedsaleh, "Histological Stains: A Literature Review and Case Study," *Global Journal of Health Science,* vol. 8, no. 3, pp. 72-79, March 2016.

[26] V. Bobroff, H.-H. Chen, M. Delugin, S. Javerzat and C. Petibois, "Quantitative IR microscopy and spectromics open the way to 3D digital pathology," *Journal of Biophotonics,* vol. 10, no. 1, p. 598–606, 2017.

[27] A. Ogunleke, V. Bobroff, H.-H. Chen, J. Rowlette, M. Delugin, B. Recur, Y. Hwu and C. Petibois, "Fourier-transform vs. quantum-cascade-laser infrared microscopes for histo-pathology: From lab to hospital?," *Trends in Analytical Chemistry,* vol. 89, no. 1, pp. 190-196, 2017.

[28] C. Petibois, "3D Quantitative Chemical Imaging of Tissues by Spectromics," *Trends in Biotechnology,* vol. 35, no. 12, pp. 1194-1207, 2017.

[29] Hospital, Robert Wood Johnson University, "Treatment for Brain Tumors Using the Gamma Knife," [Online]. Available: https://www.rwjbh.org/rwj-university-hospital-new-brunswick/treatment-care/gamma-knife/conditions-treated/brain-tumors/.

[30] M. Nakada, S. Nakada, T. Demuth, N. Tran, D. Hoelzinger and M. Berens, "Molecular targets of glioma invasion.," *Cell and molecular life sciences,* vol. 64, no. 4, pp. 458-478, 2007.

[31] S. Larjavaara, R. Mäntylä, T. Salminen, H. Haapasalo, J. Raitanen, J. Jääskeläinen and A. Auvinen, "Incidence of gliomas by anatomic location," *Neuro Oncology,* vol. 9, no. 3, p. 319–325, July 2007.

[32] D. Persaud-Sharma, J. Burns, J. Trangle and S. Moulik, "Disparities in Brain Cancer in the United States: A literature review of gliomas".

[33] A. R. Elvidge, "The morphology, Biological Behaviour and Prognosis of Brain Tumors," *Cancer Journal for Clinicians,* vol. 5, no. 6, pp. 192-204, November 1955.

[34] V. P. Collins, "Brain tumors: Classification and Genes," *Journal of Neurology, Neurosurgery and Psychiatry,* vol. 75, no. 1, pp. ii2-i11, 14 May 2004.

[35] O. G. Dodge, "Histological Typing of tumors of the Central Nervous System," *Brithish Journal of Cancer,* vol. 44, no. 3, p. 480, 1981.

[36] D. P. Agamanolis, "Tumors of the central nervous system," in *Neuropathology: An illustrated interactive course for medical students and residents*, 2017.

[37] J. S. Michael, G. Juanita, C. V. Juan, M. Mansour, E. Noah and M. L. Ware, "Brain tumors: Epidemology and Current Trends," *Brain tumors and Neurooncology,* vol. 1, no. 1, pp. 1-21, 30 September 2015.

[38] M. Nikiforova, A. Wald, M. Melan, S. Roy, S. Zhong, R. Hamilton, F. Lieberman, J. Drappatz, N. Amankulor, I. Pollack, Y. Nikiforov and C. Horbinski, "Targeted next-generation sequencing panel (GlioSeq) provides comprehensive genetic profiling of central nervous system tumors.," *Neuro Oncology,* vol. 18, no. 3, pp. 379-387, March 2016.

[39] K. Ali, Y. Lu, U. Das, R. K. Sharma, S. Wiebe, Kotoo, M. V. Sadanand, D. R. Fourney, A. Vitali, M. Kelly, T. May, J. Gomez and E. Pellerin, "Biomolecular diagnosis of human glioblastoma multiforme using Synchrotron mid-infrared spectromicroscopy," *International Journal of molecular medicine,* vol. 26, no. 1, pp. 11-16, 2010.

[40] D. R. Ifa and L. S. Eberlin, "Ambient Ionization Mass Spectrometry for Cancer Diagnosis and Surgical Margin Evaluation," *Clinical Chemistry,* vol. 62, no. 1, pp. 111-123, January 2016.

[41] A. K. Jarmusch, V. Pirro, Z. Baird, E. M. Hattab, A. A. Cohen-Gadol and G. R. Cooks, "Lipid and metabilite profiles of human brain tumors by desorption electrospray ionization-

MS," *Proceedings of the National Academy of Science of the Unuted States of America,* vol. 113, no. 6, pp. 1486-1491, 9 February 2016.

[42] A. S. Sarah, J. W. Robert, D. J. Mahlon, A. T. Steven and M. C. Richard, "Protein Profiling in Brain Tumors Using Mass Spectrometry: Feasibility of a New Technique for the Analysis of Protein Expressioon," *Clinical Cancer Research ,* vol. 10, no. 1, pp. 981-987, 1 Febryary 2004.

[43] P. M. Vaysse, R. M. A. Heeren, T. Porta and B. Balluf, "Mass spectrometry imaging for clinical research – latest developments, applications, and current limitations," *Royal Society of Chemistry,* vol. 142, no. 1, pp. 2690-2712, 5 April 2017.

[44] D. Calligaris, I. Norton, D. R. Feldman, J. L. Ide, I. F. Dunn, L. S. Eberlin, R. G. Cooks, F. A. Jolesz, A. J. Golby, S. Santagata and N. Y. Agar, "Mass Spectrometry Imaging as a Tool for Surgical Decision-Making," *J Mass Spectrom,* vol. 48, no. 11, p. 1178–1187, Nov 2013.

[45] J. Zhang, Y. Fan, M. He, X. Ma, Y. Song, M. Liu and J. Xu, "Accuracy of Raman spectroscopy in differentiating brain tumor from normal brain tissue," *Oncotarget,* vol. 8, no. 22, p. 36824–36831, 7 March 2017.

[46] S. Kalkanis, R. Kast, M. Rosenblum, T. Mikkelsen, S. Yurgelevic, K. Nelson, A. Raghunathan, L. Poisson and G. Auner, "Raman spectroscopy to distinguish grey matter, necrosis, and glioblastoma multiforme in frozen tissue sections.," *Journal of neuro-oncology,* vol. 116, no. 3, pp. 1326-9, February 2014.

[47] R. Aguiar, L. J. Silveira, E. Falcão, M. Pacheco, R. Zângaro and C. Pasqualucci, "Discriminating neoplastic and normal brain tissues in vitro through Raman spectroscopy: a principal components analysis classification model.," *Photomedcine and laser surgery,* vol. 31, no. 12, pp. 595-604, December 2013.

[48] S. Yao, H.-H. Chen, E. Harte, G. D. Ventura and C. Petibois, "The role of asbestos morphology on their cellular toxicity: an in vitro 3D Raman/Rayleigh imaging study," *Analytical and Bioanalytical Chemistry,* vol. 405, no. 27, p. 8701–8707, 2013.

[49] A. Imiela, B. Polis, L. Polis and H. Abramczyk, "Novel strategies of Raman imaging for brain tumor research," *Oncotarget,* vol. 8, no. 49, p. 85290–85310, October 2017.

[50] C. Beleites, K. Geiger, M. Kirsch, S. Sobottka, G. Schackert and R. Salzer, "Raman spectroscopic grading of astrocytoma tissues: using soft reference information.," *Analytical and bioanalytical chemistry,* vol. 400, no. 9, pp. 2801-16, July 2011.

[51] T. J. Vickers, R. E. Wambles Jr. and C. K. Mann, "Curve Fitting and Linearity: Data Processing in Raman Spectroscopy," *Applied Spectroscopy,* vol. 55, no. 4, pp. 389-393, 1 April 2001.

[52] N. Amharref, A. Beljebbar, S. Dukic, L. Venteo, L. Schneider, M. Pluot and M. Manfait, "Discriminating healthy from tumor and necrosis tissue in rat brain tissue samples by Raman spectral imaging," *Biochimica et Biophysica Acta (BBA) - Biomembranes,* vol. 1768, no. 10, pp. 2605-2615, 2007.

[53] C. Petibois and G. Deleris, "Chemical mapping of tumor progression by FT-IR imaging: towards molecular histopathology," *Trends in Biotechnology,* vol. 24, no. 10, 2006.

[54] R. Bhargava, "Towards a practical Fourier transform infrared chemical imaging protocol for cancer histopathology," *Anal Bioanal Chem,* vol. 389, no. 1, p. 1155–1169, 2007.

[55] C. Petibois, B. Drogat, A. Bikfalvi, G. Deleris and M. Moenner, "Histological mapping of biochemical changes in solid tumors by FT-IR spectral imaging," *FEBS Letters,* vol. 581, no. 28, pp. 5469-74, 2007.

[56] M. Diem, L. Chiriboga, P. Lasch and A. Pacifico, "Infrared spectra and infrared spectral maps of individual normal and cancerous cells," *Biopolymers (Biospectroscopy),* vol. 67, no. 4–5, p. 349–353, 2002.

[57] M. Diem, S. Boydston-White and L. Chiriboga, "Infrared spectroscopy of cells and tissues: shining light onto a novel subject," *Appl. Spectrosc,* vol. 53, no. 4, p. 148–161, 1999.

[58] N. Amharrefa, A. Beljebbara, S. Dukica, L. Venteo, L. Schneider, M. Pluot, R. Vistellea and M. Manfait, "Brain tissue characterisation by infrared imaging in a rat glioma model," *BBA-Biomembranes,* vol. 1758, no. 7, pp. 892-899, July 2006.

[59] B. e. a. Wood, "A three-dimensional multivariate image processing technique for the analysis of FTIR spectroscopic images of multiple tissue sections.," *BMC Med. Imaging,* vol. 6, p. 1–9, 2006.

[60] Y. Liu and A. Chiang, "High-resolution confocal imag- ing and three-dimensional rendering," *Methods,* vol. 30, p. 86–93 , 2003.

[61] S. e. a. Yao, "The role of asbestos morphology on their cellular toxicity: an in vitro 3D Raman/Rayleigh imaging study.," *Anal. Bioanal. Chem.,* vol. 27, p. 8701–8707, 2013.

[62] L. e. a. Fornai, "Three-dimensional molecular reconstruction of rat heart with mass spectrometry imaging.," *Anal. Bioanal. Chem.,* vol. 404, p. 2927–2938, 2012.

[63] L. e. a. Eberlin, "Three-dimensional vizualization of mouse brain by lipid analysis using ambient ionization mass spectrometry.," *Angew. Chem. Int. Ed. Engl.,* vol. 49, p. 873–876, 2010.

[64] L. Wang and B. Mizaikoff, "Application of multivariate data-analysis techniques to biomedical diagnostics based on mid-infrared spectroscopy.," *Anal Bioanal Chem,* vol. 391, no. 1, p. 1641–54, 2008.

[65] G. Bellisola and C. Sorio, "Infrared spectroscopy and microscopy in cancer research and diagnosis," *American Journal of Cancer Research,* vol. 2, no. 1, pp. 1-21, 2012.

[66] Thermo Nicolet, Introduction to Fourier Transform Infrared Spectrometry, Madison: Thermo Nicloet, 2001.

[67] J. M. Chalmers and P. R. Griffiths, Handbook of vibrational spectroscopy, New York: J Wiley, 2002.

[68] P. Garidel, M. Boese and J. Diaz, "Non-Invasive Fourier Transform Infrared Microspectroscopy and Imaging Techniques: Basic Principles and Applications," *Modern Research and Educational Topics in Microscopy.,* vol. 1, no. 1, pp. 132-143, 2007.

[69] I. Levin and R. Bhargava, "Fourier transform infrared vibrational spectroscopic imaging: integrating microscopy and molecular recognition.," *Annual review of physical chemistry,* vol. 56, no. 1, pp. 429-74, 2005.

[70] L. H. Kidder, I. W. Levin, E. N. Lewis, V. D. Kleiman and E. J. Heilweil, "Mercury cadmium telluride focal-plane array detection for mid-infrared Fourier-transform spectroscopic imaging," *Optics Letters,* vol. 22, no. 10, pp. 742-744.

[71] K. C. Liddiard, "Thin-film resistance bolometer IR detectors," *The International Society for Optical Engineering,* vol. 413, no. 110, p. 1, 2000.

[72] E. N. Lewis, E. Lee, L. H. Kidder, E. H. Jefferson, C. D. Ellison, P. J. Faustino, R. C. Lyon and A. S. Hussain, "Extending the Detection Limit for Near Infrared Spectroscopic Measurements of Heterogeneous Solids Using Focal Plane Array Detectors," *Microscopy and Microanalysis,* vol. 9, no. S02, p. 1076–1077, 2003.

[73] C. Matthäus, B. Bird, M. Miljković, T. Chernenko, M. Romeo and M. Diem, "Chapter 10: Infrared and Raman microscopy in cell biology.," in *Methods in Cell Biology*, vol. 89, Academic Press, 2008, pp. 275-308.

[74] G. L. Mostaco and L. Bachmann, "Application of FTIR Spectroscopy for Identification of Blood and Leukemia Biomarkers: A Review over the Past 15 Years.," *British journal of haematology,* vol. 46, p. 388–404, 2011.

[75] C. Petter, N. Heigl, M. Rainer, R. Bakry, J. Pallua, G. Bonn and C. Huck, "Development and application of Fourier-transform infrared chemical imaging of tumour in human tissue.," *Current medicinal chemistry,* vol. 16, no. 3, pp. 318-326, 2009.

[76] M. Walsh, M. German, M. Singh, H. Pollock, A. Hammiche, M. Kyrgiou, H. Stringfellow, E. Paraskevaidis, P. Martin-Hirsch and F. Martin, "IR microspectroscopy: potential applications in cervical cancer screening," *Cancer Letters,* vol. 246, no. 1-2, pp. 1-11, 2007.

[77] I. Rehman, S. Rehman, Z. Movasaghi and J. Darr, " Fourier Transform Infrared Spectroscopic Analysis of Breast Cancer Tissues; Identifying Differences between Normal Breast, Invasive Ductal Carcinoma, and Ductal Carcinoma In Situ of the Breast.," *Applied Spectroscopy Reviews,* vol. 45, p. 355–368, 2010.

[78] J. Kwak, S. Hewitt, S. Sinha and R. Bhargava, "Multimodal microscopy for automated histologic analysis of prostate cancer.," *BMC Cancer,* vol. 11, p. 62, Feb 2011.

[79] P. Lewis, K. Lewis, R. Ghosal, B. S, L. AJ, J. Wills, R. Godfrey, P. Kloer and L. Mur, "Evaluation of FTIR spectroscopy as a diagnostic tool for lung cancer using sputum.," *BMC Cancer,* vol. 10, p. 640, 23 November 2010.

[80] R. Sahu and S. Mordechai, "Spectral signatures of colonic malignancies in the mid-infrared region: from basic research to clinical applicability," *Future Oncol.,* vol. 6, no. 10, pp. 1653-67, Oct 2010.

[81] K. Wehbe, R. Pineau, S. Eimer, A. Vital, H. Loiseau and G. Déléris, "Differentiation between normal and tumor vasculature of animal and human glioma by FTIR imaging.," *The Analyst,* vol. 135, no. 12, pp. 3052-9, Dec 2010.

[82] N. Eikje, K. Aizawa, T. Sota, Y. Ozaki and S. Arase, "Identification and characterization of skin biomolecules for drug targeting and monitoring by vibrational spectroscopy.," *Open Med Chem J.,* vol. 2, pp. 38-48, 8 May 2008.

[83] L. Quaroni and A. Casson, "Characterization of Barrett esophagus and esophageal adenocarcinoma by Fourier-transform infrared microscopy.," *The Analyst.,* vol. 134, no. 6, pp. 1240-6., June 2009.

[84] N. F. Le, M. Bralet, D. Debois, C. Sandt, C. Guettier, P. Dumas, A. Brunelle and O. Laprévote, "Chemical imaging on liver steatosis using synchrotron infrared and ToF-SIMS microspectroscopies.," *PLoS One,* vol. 4, no. 10, p. e7408, October 2009.

[85] B. Bird, M. Miljkovic, M. Romeo, J. Smith, N. Stone, M. George and M. Diem, "Infrared micro-spectral imaging: distinction of tissue types in axillary lymph node histology.," *BMC Clin Pathol,* vol. 8, p. 8, 29 August 2008.

[86] J. Kelly, T. Nakamura, S. Kinoshita, N. Fullwood and F. Martin, "Evidence for a stem-cell lineage in corneal squamous cell carcinoma using synchrotron-based Fourier-transform infrared microspectroscopy and multivariate analysis.," *The Anaylst,* vol. 135, no. 12, pp. 3120-5., Dec 2010.

[87] C. Petibois and B. Desbat, "Clinical application of FTIR imaging: new reasons for hope," *Trends in Biotechnology,* vol. 28, p. 495–500, 2010.

[88] N. Salvado, S. Buti, M. Tobin, E. Pantos, A. John, N. Prag and T. Pradell, " Advantages of the use of SR-FT-IR microspectroscopy: applications to cultural heritage.," *Analytical Chemistry,* vol. 77, pp. 3444-3451, 2005.

[89] P. Dumas, N. Jamin, J. Teillaud, L. Miller and B. Beccard, "Imaging capabilities of synchrotron infrared microspectroscopy.," *Faraday Discuss,* vol. 126, pp. 289-302, 2004.

[90] C. Petibois, M. Piccinini, M. Guidi and A. Marcelli, "Facing the challenge of biosamples FTIR imaging using the synchrotron radiation source," *Journal of synchrotron radiation,* vol. 17, p. 1–11, 2010.

[91] J. Rowlette, M. Weida, B. Bird, D. Arnone, M. Barre and T. Day, "High-confidence, high-throughput screening with high- def IR microspectroscopy," *BioOptics World,* March/April 2014.

[92] Y. Yao, A. Hoffman and C. Gmachl, "Mid-infrared quantum cascade lasers," *Nat. Photonics,* vol. 6, pp. 432-439., 2012.

[93] M. Kole, R. Reddy, M. Schulmerich, M. Gelber and R. Bhargava, "Discrete frequency infrared microspectroscopy and imaging with a tunable quantum cascade laser," *Analytical Chemistry,* vol. 84, pp. 10366-10372., 2012.

[94] T. David, D. Childs, R. A. Hogg, D. G. Revin, I. U. Rehman, J. W. Cockburn and S. J. Matcher, "Sensitivity Advantage of QCL Tunable-Laser Mid-Infrared Spectroscopy Over FTIR Spectroscopy," *Applied Spectroscopy Reviews,* vol. 50, no. 10, pp. 822-839, 2015.

[95] A. Barth, "Infrared spectroscopy of proteins.," *Biochim Biophys Acta,* vol. 1767, no. 9, pp. 1073-101., September 2007.

[96] B. Stuart, Infrared Spectroscopy: Fundamentals and Applications, John Wiley & Sons, Ltd, 2004.

[97] Z. Zhang, S. Chen and Y. Liang, "Baseline correction using adaptive iteratively reweighted penalized least squares," *The Analyst,* vol. 135, p. 1138–46, 2010.

[98] K. H. Liland, T. Almy and B. H. Mevik, "Optimal choice of baseline correction for multivariate calibration of spectra," *Applied Spectroscopy,* vol. 64, no. 9, p. 1007–1016, 2010.

[99] C. Beleites, "Fitting Baselines to Spectra," 2015.

[100] A. J. Owen, "Uses of Derivative Spectroscopy," Agilent Technologies, 1995.

[101] M. Gutierrez, "DERIVATIVE SPECTROSCOPY APPLIED TO THE DETERMINATION OF ALPHA- AND BETA-ACIDS IN HOPS," *J. Inst. Brew.,* vol. 98, pp. 277-281, July-August, 1992.

[102] L. Rieppo, S. Saarakkala, T. Närhi, H. Helminen, J. Jurvelin and J. Rieppo, "Application of second derivative spectroscopy for increasing molecular specificity of Fourier transform infrared spectroscopic imaging of articular cartilage.," *Osteoarthritis Cartilage.,* vol. 20, no. 5, pp. 451-459, May 2012.

[103] C. Krafft, G. Steiner, C. Beleites and R. J. Salzer, "Disease recognition by infrared and Raman spectroscopy.," *Biophotonics.,* vol. 2, no. 1-2, pp. 13-28, Feb 2009.

[104] I. Jolliffe, Principal component analysis, New York: Springer, 2002.

[105] L. Li, "Dimension reduction for high-dimensional data," *Methods Mol Biol.,* vol. 620, pp. 417-34, 2010.

[106] D. Ami, A. Natalello, P. Mereghetti, T. Neri, M. Zanoni, M. Monti, S. M. Doglia and C. A. Redi, "FT-IR spectroscopy supported by PCA–LDA analysis for the study of embryonic stem cell differentiation," *Spectroscopy,* vol. 24, p. 89–97, 2010.

[107] V. Bobroff, H.-H. Chen, M. Delugin, S. Javerzat and C. Petibois, "Quantitative IR microscopy and spectromics open the way to 3D digital pathology," *Journal of Biophotonics,* vol. 10, p. 598–606, 2017.

[108] H.-H. Chen, V. Bobroff, M. Delugin, R. Pineau, R. Noreen, Y. Seydou, S. Banerjee, J. Chatterjee, S. Javerzat and C. Petibois, "The Future of Infrared Spectroscopy in Biosciences:

In Vitro, Time-Resolved, and 3D," *ACTA PHYSICA POLONICA,* vol. 129, no. 2, pp. 255-259, 2016.

[109] N. Roberts, D. Magee, S. Yi, K. Brabazon, M. Shires, D. Crellin, N. M. Orsi, R. Quirke, P. Quirke and T. Darren, "Toward Routine Use of 3D Histopathology as a Research Tool," *The American Journal of Pathology,* vol. 180, no. 5, pp. 1835-1842, July 2012.

[110] M. E. Vandenberghe, A. S. Herard, N. Souedet, E. Sadouni, M. D. Santin, D. Briet, D. Carre, J. Schulz, P. Hantraye, P. E. Chabrier, T. Rooney, T. Debeir, V. Blanchard, L. Pradier, M. Dhenai and T. Delzescaux, "High-throughput 3D whole-brain quantitative histopathology in rodents.," *Sci. Rep.,* vol. 6, no. 20958, 2016.

[111] T. Hjornevik, T. B. Leergaard, D. Darine, O. Moldestad, A. M. Dale, F. Willoch and J. G. Bjaalie, "Three-dimensional atlas system for mouse and rat brain imaging data," *Front. Neuroinform,* vol. 1, no. 4, 02 November 2007.

[112] X. Yiwen, G. P. J., N. Zengxuan, G. Eli, A. John-Michael, Y. Hao and D. W. Aaron, "A Method for 3D Histopathology Reconstruction Supporting Mouse Microvasculature Analysis," *PLOS ONE,* vol. 10, no. 5, 29 May 2015.

[113] J. Pichata, J. E. Iglesiasa, T. Yousry, S. Ourselin and M. Modat, "A Survey of Methods for 3D Histology Reconstruction," *Medical Image Analysis,* vol. 46, pp. 73-105, May 2018.

[114] Y. Yagi and J. R. Gilbertson, "Digital imaging in pathology: the case for standardization," *Journal of Telemedicine and Telecare,* vol. 11, p. 109–116, 2005.

[115] Z. Yang, K. Richards, N. D. Kurniawan, S. Petrou and D. C. Reutens, "Mri-guided volume reconstruction of mouse brain from histological sections," *Journal of neuroscience methods,* vol. 211, no. 2, pp. 210-217, 2012.

[116] L. Nyúl and J. Udupa, "On standardizing the MR image intensity scale.," *Magnetic resonance in medcine,* vol. 42, no. 6, pp. 1072-1081., Dec 1999.

[117] X. Li, T. E. Yankeelov, G. D. Rosen, J. C. Gore and B. M. Dawant, "Enhancement of histological volumes through averaging and their use for the analysis of magnetic resonance images.," *Magnetic resonance imaging,* vol. 27, no. 3, p. 401–416, 2009.

[118] J. Pichat, M. Modat, T. Yousry and S. Ourselin, "A multi-path approach to histology volume reconstruction," in *Biomedical Imaging (ISBI), 2015 IEEE 12th International Symposium on. IEEE*, 2015.

[119] M. S. Breen, R. S. Lazebnik and D. L. Wilson, "Three-dimensional registration of magnetic resonance image data to histological sections with 39 model-based evaluation.," *Annals of biomedical engineering,* vol. 33, no. 8, p. 1100–1112, 2005.

[120] A. S. Choe, Y. Gao, X. Li, K. B. Compton, I. Stepniewska and A. W. Anderson, "Accuracy of image registration between mri and light microscopy in the ex vivo brain.," *Magnetic resonance imaging ,* vol. 29, no. 5, p. 683–692, 2011.

[121] S. D. Kumar S, "Texture Feature Extraction to Colorize Gray Images," *International Journal of Computer Applications,* vol. 63, no. 17, 2013.

[122] S. Yuheng and Y. Hao, Image Segmentation Algorithms Overview, 2017.

[123] C. Heitz, F. A. Nehlig and I. J. A. J. P. Namer, "Journal of neuroscience methods," *A robust statistics-based global energy function for the alignment of serially acquired autoradiographic sections.,* vol. 124, no. 1, p. 93–102, 2003.

[124] C. Palm, M. Axer, D. Graßel, J. Dammers, J. Lindemeyer, K. Zilles, U. Pietrzyk and K. Amunts, "Towards ultra-high resolution fibre tract mapping of the human brain-registration of polarised light images and reorientation of fibre vectors.," *Frontiers in human neuroscience,* vol. 4, no. 9, 2010.

[125] P. A. Yushkevich, B. B. Avants, L. Ng, M. Hawrylycz, P. D. Burstein, H. Zhang and J. C. Gee, "3d mouse brain reconstruction from histology using a coarse-to-fine approach," *Biomedical Image Registration,* p. 230–237, 2006.

[126] D. Chudasama, T. Patel and S. Joshi, "Image Segmentation using Morphological Operations," *International Journal of Computer Applications,* vol. 117, no. 18, pp. 16-19, May 2015.

[127] E. Anjna and R. Kaur, "Review of Image Segmentation Technique," *International Journal of Advanced Research in Computer Science,* vol. 8, no. 4, May 2017.

[128] D. Kaur and Y. Kaur, "Various Image Segmentation Techniques: A Review," *International Journal of Computer Science and Mobile Computing,* vol. 3, no. 5, 2014.

[129] D. D. Patil and S. G. Deore, "Medical Image Segmentation: A Review," *International Journal of Computer Science and Mobile Computing,* vol. 2, no. 1, pp. 22-27, 2013.

[130] F. Derraz, M. Khelif and M. Beladgham, "Application of Active Contour Models in Medical Image Segmentation," *ITCC,* vol. 2, 2004.

[131] T. Kanade, Z. Yin, R. Bise, S. Huh, S. Eom, M. F. Sandbothe and M. Chen, "Cell Image Analysis: Algorithms, System and Applications," in *Computer Vision tracking of stemness*, 2008.

[132] J. Ashburner and K. Friston, "Rigid body registration.," in *Human Brain Function*, San Diego, Academic Press, 2003.

[133] W. R. Crum, T. Hartkens and D. L. G. Hill, "Non-rigid image registration: theory and practice," *The British Journal of Radiology,* vol. 77, p. S140–S153, 2004.

[134] A. A. Goshtasby, Image Registration: Principles, Tools and Methods, London: Springer Science & Business Media, 2012.

[135] J. B. Antoine Maintz and M. A. Viergever, "An Overview of Medical Image Registration Methods," *Medical Image Analysis,* 1996.

[136] E. Ferrantea and N. Paragios, "Slice-to-volume medical image registration: a survey," *Medical Image Analysis,* vol. 39, pp. 101-123, 2017.

[137] C. Kuglin and D. Hines, " The Phase Correlation Image Alignment Method," *Proc. of the IEEE Int. Conf. on Cybernetics and Society,* p. 163–165, 1975.

[138] E. M. C. De Castro, " Registration of Translated and Rotated Images Using Finite Fourier Transforms.," *IEEE Transactions on Pattern Analysis and Machine Intelligence,* 9 1987.

[139] B. Reddy and B. Chatterji, "An FFT-Based Technique for Translation, Rotation, and Scale-Invariant Image Registration.," *IEEE Transactions on Image Processing,* vol. 5, p. 1266–1271, 1996.

[140] H. Yan and J. Liu, "Robust Phase Correlation Based Feature Matchinig for Image Co-registration and Dem Generation.," *The International Archives of the Photogrammetry, Remote Sensing and Spatial Information Sciences,* vol. XXXVII, 2008.

[141] B. Reddy and B. Chatterji, "An FFT-based technique for translation, rotation, and scale-invariant image registration," *IEEE Transactions on Image Processing,* vol. 5, no. 8, pp. 1266 - 1271, August 1996.

[142] Orderud, "Phase Correlation," [Online]. Available: https://commons.wikimedia.org/w/index.php?curid=18403288.

[143] N. S. Jignesh, P. Suprava and K. Kajal, "Image Registration Using Log Polar Transform and Phase Correlation to Recover Higher Scale," *JOURNAL OF PATTERN RECOGNITION RESEARCH,* vol. 7, pp. 90-105, 2012.

[144] J. N. Sarvaiya, S. Patnaik and S. Bombaywala, "Image registration using Log polar transform and phase correlation," in *TENCOON 2009: IEEE Region 10 Conference,*, 2009.

[145] Q.-s. Chen, M. Defrise and F. Deconinck, "Symmetric phase-only matched filtering of Fourier Mellin transform for image registration and recognition," *IEEE Trans. on Pattern Analysis and Machine Intelligence,* vol. 16, pp. 1156-1168, 1994.

[146] X. Guo, Z. Xu, Y. Lu and Y. Pang, "An Application of Fourier-Mellin Transform in Image Registration," in *Proceedings of The Fifth International Conference on Computer and Information Technology*, 2005.

[147] B. Sun and D. Zhou, "Rotated Image Matching Method Based on CISD," vol. LNCS 4491, no. PART 1, pp. 1346-1352, 2007.

[148] G. Wolberg and S. Zokai, "Robust image registration using log-polar transform," in *International Conference on Image Processing*, 2000.

[149] B. Zitova and J. Flusser, "Image Registration Methods: a survey," *Elsevier Image and Vision Computing,* July 2003.

[150] V. H. Gandhi and S. R. Panchal, "Feature Based Image Registration Techniques: An Introductory Survey," *International Journal of Engineering Development and Research,* vol. 2, no. 1, pp. 368-375, 2014.

[151] C. Harris and M. Stephens, "A combined corner and edge detector," in *In Proc. of Fourth Alvey Vision Conference*, 1988.

[152] T. Tuytelaars and K. Mikolajczyk, "Local Invariant Feature Detectors: A Survey," *Foundations and Trends Rin Computer Graphics and Vision,* May 2008.

[153] C. Schmid, R. Mohr and C. Bauckhage, "Evaluation of Interest Point Detectors," *International Journal of Computer Vision,* June 2000.

[154] E. I. Zacharaki, D. Shen, S.-K. Lee and C. Davatzikos, "ORBIT: A Multiresolution Framework for Deformable Registration of Brain Tumor Images," *IEEE Transactions on Medical Imaging,* vol. 27, no. 8, pp. 1003 - 1017, August 2008.

[155] G. E. Hemamalini and J. Prakash, "Medical Image Analysis of Image Segmentation and Registration Techniques," *International Journal of Engineering and Technology (IJET),* vol. 8, no. 5, pp. 2234-2241, Oct-Nov 2016.

[156] D. Lowe, "Object recognition from local scale-invariant features," *Proceedings of International Conference on Computer Vision,* pp. 1150-1157, 1999.

[157] H. Bay, T. Tuytelaars and L. V. Gool, "SURF: speeded up robust features," *ECCV,* 2006.

[158] M. A.-R. Hasso and R. M. Elyas, "Fast Image Registration Based on Features Extraction and Accurate Matching Points for Image Stitching," *International Journal of Computer Science Issues,* vol. 11, no. 5, pp. 138-142, 2014.

[159] M. Hassaballah, A. A. Abdelmgeid and H. A. Alshazly, "Image Features Detection, Description and Matching," in *Studies in Computational Intelligence*, Switzerland, © Springer International Publishing, 2016.

[160] J. Garamendi, C. Ballester, L. Garrido, V. Lazcano and V. Caselles, "Joint TV-L1 Optical Flow and Occlusion Estimation," *IPOL,* 2014.

[161] D. Fortun, P. Bouthemy and C. Kervrann, "Optical flow modeling and computation: a survey," *Computer Vision and Image Understanding,* 2015.

[162] H. Raveshiya and V. Borisagar, "Motion Estimation Using Optical Flow Concepts," *Internation Journal of Computer Technology & Applications,* vol. 3, no. 2, pp. 696-700, 2012.

[163] M. T. McCann, J. A. Ozolek, C. A. Castro, B. Parvin and J. Kovacevic, "Automated histology analysis: Opportunities for signal processing.," *IEEE Signal Processing Magazine,* vol. 32 , no. 1, 2015.

[164] N. Chicherova, K. Fundana, B. Muller and P. C. Cattin, "Histology to μct data matching using landmarks and a density biased ransac.," in *International Conference on Medical Image Computing and Computer-Assisted Intervention.*, 2014.

[165] S. Osechinskiy and F. Kruggel, "Slice-to-volume nonrigid registration of histological sections to mr images of the human brain.," *Abstract Full-Text PDF Full-Text HTML Full-Text XML Linked References Citations to this Article How to Cite this Article Anatomy Research International,* vol. 2010, 2010.

[166] G. Malandain, E. Bardinet, K. Nelissen and W. Vanduffel, "Fusion of autoradiographs with a nmr volume using 2-d and 3-d linear transformations," *NeuroImage,* vol. 23, no. 1, p. 111–127, 2004.

[167] M. Stille, E. J. Smith, W. R. Crum and M. Modo, "3d reconstruction of 2d fluorescence histology images and registration with in vivo mr images: Application in a rodent stroke model.," *Journal of neuroscience methods,* vol. 219, no. 1, p. 27–40, 2013.

[168] M. Goubran, C. Crukley, S. de Ribaupierre, T. M. Peters and A. R. Khan, "Image registration of ex-vivo mri to sparsely sectioned histology of hippocampal and neocortical temporal lobe specimens," *Neuroimage,* vol. 83, p. 770–781, 2013.

[169] S. Gaffling, V. Daum and J. Hornegger, "Landmark-constrained 3-d histological imaging: A morphology-preserving approach," *VMV,* p. 309–316, 2011.

[170] T. Ju, J. Warren, J. Carson, M. Bello, I. Kakadiaris, W. Chiu, C. Thaller and G. Eichele, "3d volume reconstruction of a mouse brain from histological sections using warp filtering.," *Journal of Neuroscience Methods,* vol. 156, no. 1, p. 84–100, 2006.

[171] S. Wirtz, B. Fischer, J. Modersitzki and O. Schmitt, "Superfast elastic registration of histologic images of a whole rat brain for 3d reconstruction," *Medical Imaging,* p. 328–334, 2004.

[172] L. Alic, J. C. Haeck, K. Bol, S. Klein, S. T. van Tiel, P. A. Wielepolski, M. de Jong, W. J. Niessen, M. Bernsen and J. F. Veenland, "Facilitating tumor functional assessment by spatially relating 3d tumor histology and in vivo mri: image registration approach.," *PLoS One ,* vol. 6, no. 8, pp. 228-235, 2011.

[173] D. H. Adler, J. Pluta, S. Kadivar, C. Craige, J. C. Gee, B. B. Avants and P. A. Yushkevich, "Histology-derived volumetric annotation of the human hippocampal subfields in postmortem mri," *Neuroimage ,* vol. 84, p. 505–523, 2014.

[174] M. Alegro, E. Amaro-Jr, B. Loring, H. Heinsen, E. Alho, L. Zollei, D. Ushizima and L. T. Grinberg, "Multimodal whole brain registration: Mri and high resolution histology.," in *Proceedings of the IEEE Conference on Computer Vision and Pattern Recognition Workshops.*, 2016.

[175] K. Nagara, H. R. Roth, S. Nakamura, H. Oda, T. Moriya, M. Oda and K. Mori, "Micro-ct guided 3d reconstruction of histological images.," *International Workshop on Patch-based Techniques in Medical Imaging,* p. 93–101, 2017.

[176] T. Rohlfing, "Image similarity and tissue overlaps as surrogates for image registration accuracy: widely used but unreliable.," *IEEE transactions on medical imaging,* vol. 31, no. 2, p. 153–163., 2012.

[177] R. M. Haralick, "Statistical and structural approaches to texture.," *Proceedings of IEEE,* vol. 67, no. 5, p. 786–804., 1979.

[178] A. Cifor, L. Bai and A. Pitiot, "Smoothness-guided 3-d reconstruction of 2-d histological images," *Neuroimage,* vol. 56, no. 1, p. 197–211. , 2011.

[179] Y. C. Liu and A. S. Chiang, "High-resolution confocal imaging and three-dimensional rendering.," *Methods,* vol. 30, p. 86–93, 2003.

[180] H. Ye, T. Greer and L. Li, "From pixel to voxel: a deeper view of biological tissue by 3D mass spectral imaging," *Bioanalysis ,* vol. 3, no. 3, p. 313–332., 2011.

[181] Z. Hammody, R. K. Sahu, S. Mordechai, E. Cagnano and S. Argov, "Characterization of Malignant Melanoma Using Vibrational Spectroscopy," *The scientific world journal,* vol. 5, pp. 172-182, 2005.

[182] Z.-M. Zhang, S. Chen and Y.-Z. Liang, "Baseline correction using adaptive iteratively reweighted penalized least squares," *Analyst,* vol. 135, pp. 1138-1146, 2010.

[183] C. Beleites, "Fitting Baselines to Spectra," 2015.

[184] C. Petibois, K. Wehbe, K. Belbachir, R. Noreen and G. Deleris, "Current Trends in the Development of FTIR Imaging for the Quantitative Analysis of Biological Samples," *ACTA PHYSICA POLONICA,* vol. 115, no. 2, pp. 507-512, 2009.

[185] K. Belbachir, R. Noreen, G. Gouspillou and C. Petibois, "Collagen types analysis and differentiation by FTIR spectroscopy," *Anal Bioanal Chem,* July 2009.

[186] A. Ogunleke, B. Recur, H. Balacey, s.-H. Chen, M. Delugin, Y. Hwu, S. Javerzata and C. Petibois, "3D chemical imaging of the brain using quantitative IR spectro-microscopy," *Royal Society of Chemistry,* vol. 9, no. 1, p. 89–198, 7 January 2018.

[187] R. J. DeBerardinis and C. B. Thompson, "Cellular metabolism and disease: what do metabolic outliers teach us?," *Cell,* vol. 148, no. 6, p. 1132–1144, 16 March 2016.

[188] M. J. Hackett, N. J. Sylvain, H. Hou, S. Caine, M. Alaverdashvili, M. J. Pushie and M. E. Kelly, "Concurrent Glycogen and Lactate Imaging with FTIR Spectroscopy To Spatially Localize Metabolic Parameters of the Glial Response Following Brain Ischemia," *Analytical Chemistry,* vol. 88, pp. 10949-10956, 2016.

[189] N. Roberts, D. Magee, Y. Song, K. Brabazon, M. Shires, D. Crellin, N. M. Orsi, R. Quirke, P. Quirke and D. Treanor, "Toward routine use of 3D histopathology as a research tool.," *The American Journal of Pathology,* vol. 180, no. 5, pp. 1835-42, May 2012.

[190] E. T. Quinto, "An Introduction to X-ray tomography and Radon Transforms," *Proceedings of Symposia in Applied Mathematics,* 2005.

[191] W. Yu and L. Zeng, "ℓ0 Gradient Minimization Based Image Reconstruction for Limited-Angle Computed Tomography.," *PLOS ONE ,* vol. 10, no. 7, p. 11, 2015.

[192] M. Beister, D. Kolditz and W. A. Kalender, "Iterative reconstruction methods in X-ray CT," *Physica Medica,* no. 28, pp. 94-108, 2012.

[193] J. Mourant, Y. Yamada, S. Carpenter, L. Dominique and J. Freyer, "FTIR spectroscopy demonstrates biochemical differences in mammalian cell cultures at different growth stages.," *Biophys J,* vol. 85, no. 3, pp. 1938-47, Sept 2003.

[194] Z. Keckesova, J. L. Donaher, J. De Cock and e. al, "LACTB is a tumour suppressor that modulates lipid metabolism and cell state.," *Nature,* vol. 543, no. 7647, pp. 681-686, 2017.

[195] T. Engelhorn, I. Y. Eyupoglu, M. A. Schwarz and e. al., "In vivo micro-CT imaging of rat brain glioma: a comparison with 3T MRI and histology," *Neurosci Lett,* vol. 458, no. 1, pp. 28-31, 2009.

[196] H. Toyama, M. Ichise, J. S. Liow and e. al., "[18F]FDG mouse brain PET imaging: Absolute quantification of regional cerebral glucose utilization as compared with 2-[14C]DG autoradiography," *Int Congress Series,* vol. 1265, pp. 255-261, 2004.

[197] J. A. Gleave, J. P. Lerch, R. M. Henkelman and e. al.§§, "A Method for 3D Immunostaining and Optical Imaging of the Mouse Brain Demonstrated in Neural Progenitor Cells," *PLoS One,* vol. 8, 2013.

[198] O. Chahrour, D. Cobice and J. Malone, "Stable isotope labelling methods in mass spectrometry-based quantitative proteomics," *J Pharm Biomed Anal,* vol. 113, pp. 2-20, 2015.

[199] E. S. Lein, M. J. Hawrylycz, N. Ao and e. al., "Genome-wide atlas of gene expression in the adult mouse brain.," *Nature,* vol. 445, no. 7124, pp. 168-76, 2007.

[200] E. Vlashi, C. Lagadec, L. Vergnes and e. al., "Metabolic state of glioma stem cells and nontumorigenic cells.," *Proc Natl Acad Sci U S A ,* vol. 108, no. 38, pp. 16062-7, 2011.

[201] P. Gip, G. Hagiwara, N. Ruby and H. Heller, "Sleep deprivation decreases glycogen in the cerebellum but not in the cortex of young rats," *Am J Physiol Regul Integr Comp Physiol.,* vol. 283, no. 1, pp. 54-9, 2002.

[202] M. Shimada, T. Kihara, M. Watanabe and e. al., "Regional distribution of glucose in mouse brain," *Neurochem Res,* vol. 2, no. 6, p. 595–603, 1977.

[203] R. A. Swanson and D. W. Choi, "Glial glycogen stores affect neuronal survival during glucose deprivation in vitro.," *J Cereb Blood Flow Metab ,* vol. 13, no. 1, pp. 162-9, 1993.

[204] S. M. Sagar, F. R. Sharp and R. A. Swanson, "The regional distribution of glycogen in rat brain fixed by microwave irradiation.," *Brain Res ,* vol. 417, no. 1, pp. 172-4, 1987.

[205] M. Takimoto and T. Hamada, "Acute exercise increases brain region-specific expression of MCT1, MCT2, MCT4, GLUT1, and COX IV proteins," *Journal of applied physiology ,* vol. 116, no. 9, 2014.

[206] M. V. Liberti and J. W. Locasale, "The Warburg Effect: How Does it Benefit Cancer Cells?," *Trends Biochem Sci,* vol. 41, no. 3, pp. 211-218, 2016.

[207] A. Vartanian, S. K. Singh, S. Agnihotri and e. al., "GBM's multifaceted landscape: highlighting regional and microenvironmental heterogeneity.," *Neuro Oncol ,* vol. 16, no. 9, pp. 1167-75, 2014.

[208] H. H. Chen, C. C. Chien, C. Petibois and e. al, "Quantitative analysis of nanoparticle internalization in mammalian cells by high resolution X-ray microscopy," *J Nanobiotechnol ,* vol. 9, no. 14, 2011.

[209] E. Zudaire, L. Gambardella, C. Kurcz and e. al., "A computational tool for quantitative analysis of vascular networks.," *PLoS One,* vol. 6, no. 11, 2011.

[210] C. Petibois, V. Rigalleau, A. M. Melin and e. al., "Determination of glucose in dried serum samples by Fourier-transform infrared spectroscopy.," *Clin Chem,* vol. 45, no. 9, pp. 1530-5, 1999.

[211] A. Witkin, "Scale-space filtering," in *Proceedings of International Joint Conference on Artificial Intelligence*, Germany, 1983.

[212] Y. H. M. Hassan, J. O. Ehiorobo, R. E. Irughe and O. M. Ehigiator, "Registration of Multi Time Images Using SIFT (Scale Invariant Feature Transformation)," *Journal of Earth Science and Engineering,* vol. 2, pp. 310-316, 2012.

[213] T. Lindeberg, "Scale-space theory: A basic tool for analysing structures at different scales," *ournal of Applied Statistics,* vol. 21, no. 2, pp. 224-270, 1994.

[214] A. Mian, M. Bennamoun and R. Owens, "On the repeatability and quality of keypoints for local featurebased 3D object retrieval from cluttered scenes," *International Journal of Computer Vision,* vol. 89, no. 2-3, pp. 348-361. .

[215] A. Imiela, B. Polis, L. Polis and H. Abramczyk, "Novel strategies of Raman imaging for brain tumor research," *Oncotarget,* vol. 8, no. 49, p. 85290–85310, Oct 2017.

[216] D. C. Fernandez, R. Bhargava, S. M. Hewitt and I. W. Levin, "Infrared spectroscopic imaging for histopathologic recognition," *NATURE BIOTECHNOLOGY,* vol. 23, no. 4, pp. 469-474, 2005.

[217] J. E. Villanueva-Meyer, M. C. Mabray and S. Cha, "Current Clinical Brain Tumor Imaging," *Neurosurgery,* vol. 81, no. 3, p. 397–415, 01 September 2017.

[218] J. Desroches, M. Jermyn, M. Pinto, F. Picot, M.-A. Tremblay, S. Obaid, E. Marple, K. Urmey, Dominique, T. Gilles Soulez, M.-C. Guiot, B. C. Wilson, K. Petrecca and F. Leblond, "A new method using Raman spectroscopy for in vivo targeted brain cancer tissue biopsy," *Scientific Reports,* vol. 8, no. 1792, pp. 1-10, 29 January 2018.

[219] P. Chand, S. Amit, R. Gupta and A. Agarwal, "Errors, limitations, and pitfalls in the diagnosis of central and peripheral nervous system lesions in intraoperative cytology and frozen sections," *Journal of Cytology,* vol. 33, no. 2, pp. 93-97, 2016.